INVESTIGATIONS OF THE LOW-FREQUENCY DISTRIBUTED ACOUSTIC SENSING RESPONSE TO A PROPAGATING HYDRAULIC FRACTURE

A Dissertation

by

SMITH EDWARD LEGGETT

Submitted to the Graduate and Professional School of
Texas A&M University
in partial fulfillment of the requirements for the degree of

DOCTOR OF PHILOSOPHY

Chair of Committee,	Ding Zhu
Co-Chair of Committee,	Alfred Daniel Hill
Committee Members,	Siddharth Misra
	Luis San Andrés
Head of Department,	Jeffrey Spath

May 2022

Major Subject: Petroleum Engineering

ABSTRACT

Low-frequency distributed acoustic sensing has emerged as a significant diagnostic tool for characterizing unconventional completions. The distributed sensor is deployed on a monitor well and provides measurements of deformation due to propagating hydraulic fractures originating from offset wells. Lab-scale experiments and numerical investigations were conducted to aid in interpreting field-measured low-frequency distributed acoustic sensing responses.

Novel hydraulic fracture experiments were conducted using transparent epoxy blocks as fracture specimens. The epoxy blocks contained embedded fiber optic sensors used to record the strains induced by radial fracture growth. The results confirmed current interpretations of characteristic low-frequency distributed acoustic sensing patterns observed in the field. These patterns indicate the time and location that a fracture intersects the monitor well. The experiments also revealed the significance of sensor spatial resolution and debonding on the ability to accurately predict the timing of a fracture intersection. In addition, the zero strain and zero strain rate location methods were developed to estimate the location of the fracture front as it approached the monitor well using low-frequency distributed acoustic measurements.

As for the numerical investigations, a new equation was derived that relates changes in the low-frequency distributed acoustic response to temperature and strain. This relationship enabled simulation of thermal effects on the low-frequency distributed acoustic response during a multi-cluster, limited-entry type unconventional completion.

A workflow was presented to model fracture geometries, and estimate resulting far-field strain and temperature changes along a fiber optic cable. The results indicate that temperature changes can appreciably alter the low-frequency distributed acoustic response at a similar order of magnitude to strain changes after a fracture intersection occurs. However, temperature changes do not affect interpretations of the timing and location of the first fracture to intersect the monitor well.

DEDICATION

This work is dedicated to God, who uses all things for His purposes.

This work is also dedicated to Ingrid: wife, mother, friend, encourager.

The light shines in the darkness, and the darkness has not overcome it.

(English Standard Version, John 1:5)

ACKNOWLEDGEMENTS

Dr. Ding Zhu and Dr. Dan Hill have taught, mentored, and funded countless students of petroleum engineering. I am grateful to count myself as one that has benefited from their patient advising, unwavering support, and genuine advocacy. As my advisers, they shaped me and greatly improved this work. The constructive feedback from committee members Dr. Siddharth Misra and Dr. Luis San Andrés enhanced the research.

I'm also grateful to mentors new and old. John Maida and Michel LeBlanc with Halliburton in Houston, TX provided the optical interrogator used for the fiber Bragg grating strain sensing as well as fruitful discussions regarding the research. Thank you, Stuart Cox, for the encouraging phone calls and visits. Thanks to Micah Davis for the woodworking tips and letting me use your table saw.

Colleagues in the research group provided companionship, support, and encouragement throughout the study: Gongsheng, Shohei, Alex, Teresa, Julia, Jin, Karen, Yasuyuki, Jaiyue, Tohoko, Gabe, Obi, Rudy, and Robert.

I am thankful for the friends I've made while pursuing the degree, especially members of the PhD qualifying exam study group: Marcus, Emilio, Serhii, and Mohammad.

There is a good reason that John Maldonado's name is in the acknowledgement section of every petroleum student involved in lab experiments in the petroleum engineering department. He is the best.

Thanks to Stephen Amundson for sending me a Bible verse every single day for the past four years. Each one was an encouragement. You are a good friend.

Mom and Dad, thanks for all the support and encouragement. My family and I have cherished these years of living nearby. It takes a village! Your examples of prioritizing family, of faith, and selfless living make me who I am today.

Opa, thank you for helping with so many aspects of our time here, including supporting Ingrid when she really needed it. You're the best father-in-law I could ask for.

Peter, Andrew, Aubrey, Jonathan, thanks for putting up with Daddy's crazy idea to go back to school. You were always on the driveway to wave goodbye when I left, and to welcome me home. Remember: God first, family second, everything else third.

Ingrid, thanks for being my number one fan! This adventure would have been impossible without your support, which has been unwavering. One of my greatest joys in life is partnering with you in raising our kids and ministering to others. Your tireless devotion to the kids and creation of a happy home life provided the foundation from which I could launch to research and study.

And finally, Lord, thank you for your goodness and provision these past four years. I don't know what comes next, but you have proven faithful time and time again.

CONTRIBUTORS AND FUNDING SOURCES

Contributors

This work was supported by a dissertation committee consisting of advisor Dr. Ding Zhu, co-advisor Dr. Dan Hill, and committee member Dr. Siddharth Misra of the Harold Vance Department of Petroleum Engineering and Dr. Luis San Andrés of the J. Mike Walker ‘66 Department of Mechanical Engineering.

John Maldonado aided in using the mill press to drill holes in the epoxy blocks as depicted in Chapter 3. Teresa Reid assisted in acquiring some of the data for the lab experiments depicted in Chapter 4. The LF-DAS data analyzed in Chapter 5 was shared by Marathon Oil Corporation.

All other work conducted for the dissertation was completed by the student independently.

Funding Sources

Graduate study was supported by a fellowship and graduate research assistantship from the Harold Vance Department of Petroleum Engineering.

This work was also made possible in part by Marathon Oil Corporation under project number M1703159, as well as the Department of Energy under the Austin Chalk/Eagle Ford Field Laboratory project number DE-FOA-0001722. Its contents are solely the responsibility of the authors and do not necessarily represent the official views of the awarding offices.

TABLE OF CONTENTS

Page

LIST OF FIGURES

Page

LIST OF TABLES

Page

1. INTRODUCTION

Direct study of petroleum reservoirs is limited to core samples of miniscule size relative to the reservoir extent. Characterization of hydrocarbon bearing formations and hydraulic fracture completions therefore relies on indirect sampling of related physical phenomenon. Petroleum engineers and geoscientists utilize diagnostic technologies such as well logs, seismic data, and modeling production performance to characterize petroleum resources, including those developed with hydraulic fracture completions. Fiber optic sensing is one such diagnostic technology that researchers have employed for nearly three decades to investigate the subsurface (Hurtig 1993). However, a new type of fiber optic sensing, low-frequency distributed acoustic sensing, has begun to shed new light on characterizing hydraulically fractured reservoirs.

This chapter begins by addressing the importance of research into diagnostic technologies for hydraulic fracture completions, especially in the context of unconventional reservoir developments. A review of published literature related to low-frequency distributed acoustic sensing in oil and gas wells follows the motivation section. Finally, a problem statement is developed followed by a summary of the organization of the dissertation.

1.1. Motivation

The United States government forecasts crude oil and natural gas to continue to play a dominant role in meeting the country's energy demands for the next three decades (EIA 2021). Figure 1.1 exhibits historical and projected energy consumption by fuel source in the United States. While demand for renewable energy is forecasted to rise sharply,

demand for crude oil and natural gas are also projected to rise in the coming years. According to this forecast, in the year 2050, petroleum and natural gas consumption will continue to exceed renewable energy usage by more than a factor of four.

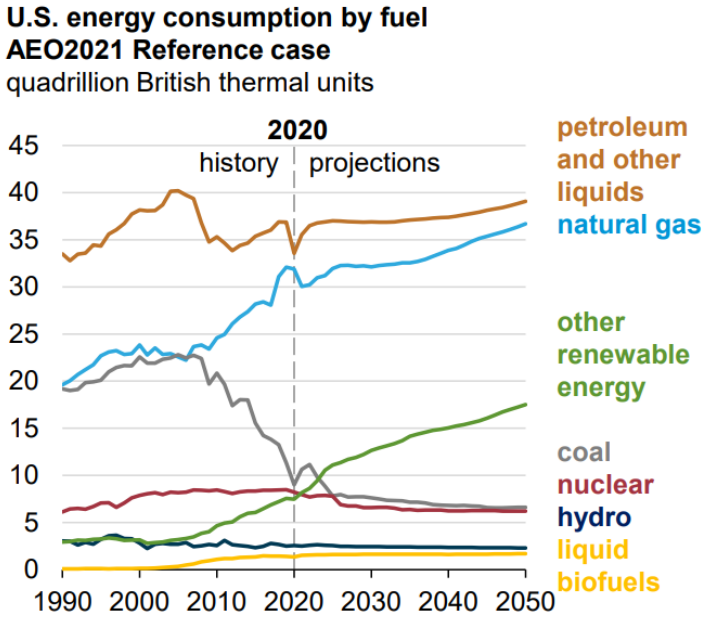

Figure 1.1 Historical and forecasted energy consumption by fuel type (EIA 2021).

Perhaps the only certain thing about forecasts is that they are certain to be wrong. The International Energy Agency presents scenarios that incorporate accelerations in the supply and demand of renewable energy. In the scenarios displayed in Figure 1.2, fossil

fuels, including coal, are on various levels of decline by the year 2050, depending on how rapidly renewable energy sources can ramp up supply (IEA 2021).

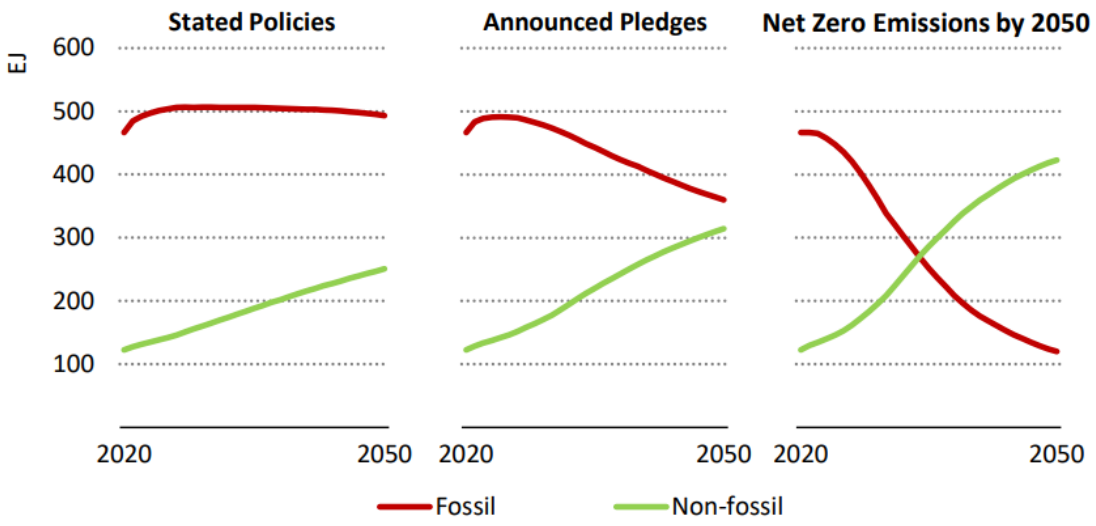

Figure 1.2 Fossil and non-fossil fuel demand scenarios: IEA (2018) World Energy Outlook. All rights reserved.

Decreasing humanity's energy usage is not a beneficial option for humanity, as argued in *The Moral Case for Fossil Fuels* (Epstein 2014). Therefore, the message conveyed in Figure 1.2 is that the global population should rely on oil, gas, and coal to make up the difference in the world's energy needs that cannot be delivered from renewable sources. The world is asking the petroleum industry to be able to rapidly ramp up or scale down

hydrocarbon production within a wide range of uncertainty. This is a tall order, especially as onshore conventional oil and gas reservoirs are largely depleted. Moreover, offshore reservoir developments require years between the initial investment and first production. The answer to this energy challenge lies in unconventional petroleum reservoir development, made accessible by multi-stage hydraulic fracturing. Low-permeability unconventional reservoirs, at times termed “tight oil” or “tight gas,” do not produce at economic rates with traditional stimulation methods. The advent of multi-stage hydraulic fracturing in horizontal wells unlocked the economic development of onshore reservoirs previously unexploitable. The data presented in Figure 1.3 from 2010 to 2020 highlight how production from low-permeability reservoirs rose to dominate the United States oil supply in the decade beginning in 2010. Three different cases of future crude oil supply are presented for beyond 2020: a base case, a low supply case, and a high supply case. Particularly striking is the juxtaposition of the tight oil production in the low and high supply cases; supply estimates differ by a factor of two. On the other hand, the oil supply projected from Alaska, the Gulf of Mexico, and other conventional assets is relatively stable in the high and low case. By nature, unconventional, hydraulically fractured, onshore reservoir development can be ramped up or down relatively rapidly in response to commodity prices. The agility of unconventional reservoir developments provides an appealing solution to humanity’s uncertain future demand for oil and gas energy.

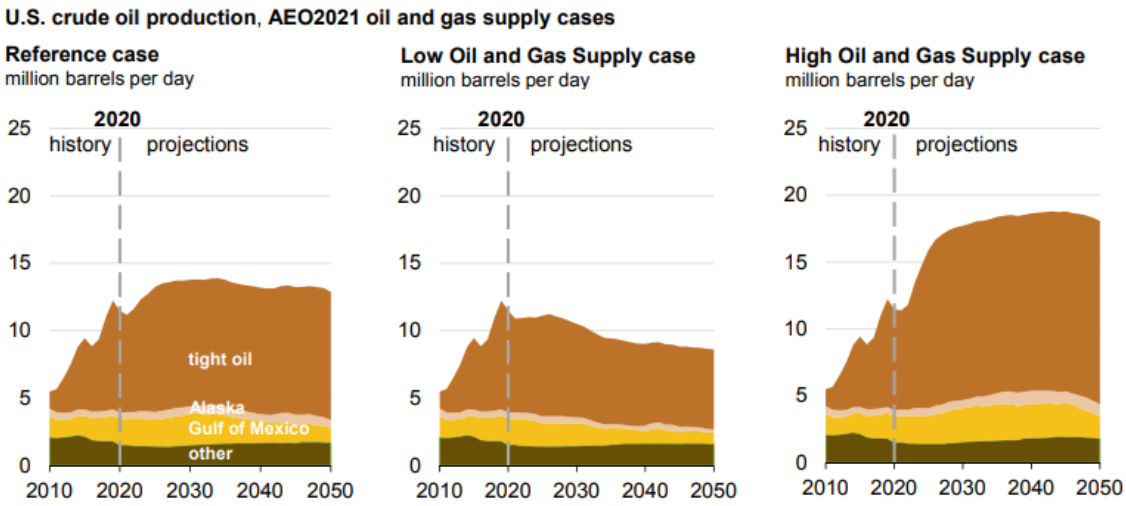

Figure 1.3 Historical and three forecasted cases of crude oil production in the United States by reservoir type (EIA 2021).

Because the world will continue to rely on oil and gas energy for the foreseeable future, and because the forecasted demand has such a wide range of uncertainty, research into improving the development of unconventional reservoirs is critical. Moreover, as the primary enabling technology for low-permeability reservoir production, multi-stage hydraulic fracturing requires continued investigation. More efficient and more effective hydraulic fracture completions improve project economics and increase hydrocarbon reserves to meet future energy demands.

Fundamental questions remain on the nature of fracture networks generated by hydraulic fracture completions. There is little consensus on the basic shape and number of hydraulic fractures generated from a single cluster in a multi-cluster fracture stage. How long and tall are they? Are height and length even useful descriptors for fracture

geometries? Where are the fractures, and where is the proppant within the fractures? Answering these questions requires hydraulic fracture diagnostic technologies that measure various characteristics or responses from the fracture, the fracture fluid, or the proppant. One such technology, low-frequency distributed acoustic sensing (low-frequency DAS, or LF-DAS), has begun to provide novel insights to help answer these questions.

1.2. Literature Review

Low-frequency DAS is an optical sensing technique used to measure changes in strain along the fiber optic cable. A typical LF-DAS deployment is illustrated in Figure 1.4. A monitor well instrumented with fiber optic cable measures the LF-DAS response due to hydraulic fracture propagation from an offset treatment well. Because the LF-DAS sensor is located on a different well than the actively stimulated well, the term “cross-well” monitoring is often applied to LF-DAS sensing. In a typical deployment, the fiber optic cable is clamped to the production casing and cemented in the wellbore.

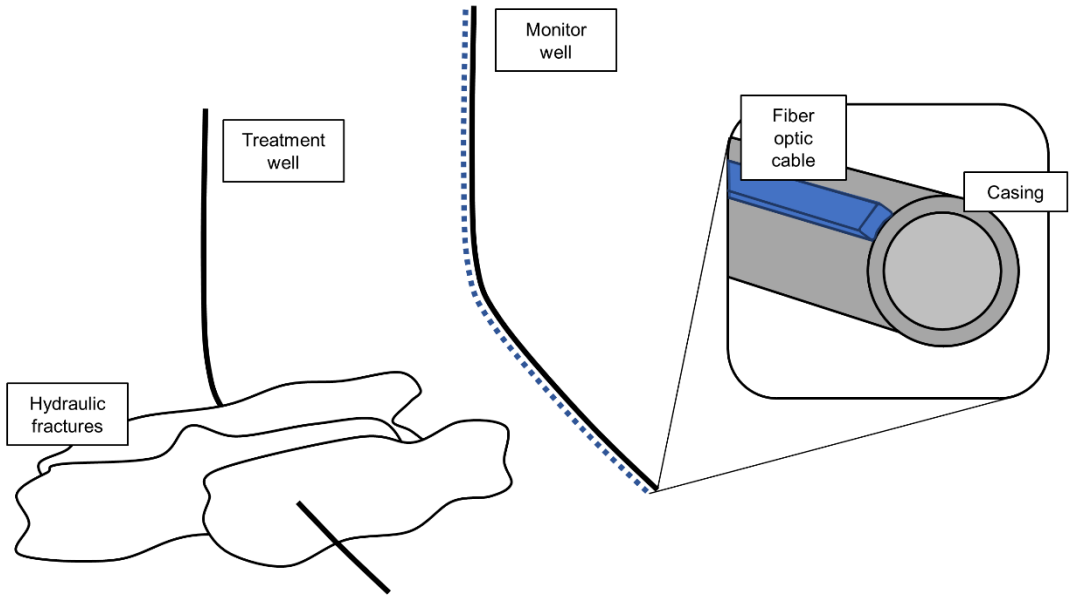

Figure 1.4 Schematic of a low-frequency distributed acoustic (LF-DAS) sensing configuration.

For a complete background of low-frequency distributed sensing, it is appropriate to review the history of its predecessor, distributed acoustic sensing (DAS).

1.2.1. Distributed Acoustic Sensing

In the 1990's, two sets of researchers discovered that the backscattered light induced by coherent light in single-mode fibers could be used for distributed sensing (Hartog 2017). Dakin and Lamb were granted a patent in 1990 for a distributed fiber optic sensor system based on measurements of the optical phase shift (Dakin 1990). Shortly thereafter, in 1993, two electrical engineering professors at Texas A&M University developed a distributed acoustic sensing system to detect intruders crossing borders based on similar

principles (Taylor 1993). As opposed to a typical sensor which measures at discrete locations, distributed optical sensors measure responses continually over the length of the fiber. For a distributed fiber optic sensor, the entire cable itself is the sensor. While measurements are reported at discrete intervals, these intervals are arbitrary and selected from the continuum of fiber optic sensor's signal.

The schematic shown in Figure 1.5 illustrates the sensing process (Silixa Ltd 2021). An optical interrogator pulses coherent light at a wavelength of approximately 1550-nanometers through an optical fiber. Due to inhomogeneities in the fiber optic cable's core, a portion of the light pulse backscatters as it transmits along the fiber. In the absence of external perturbations, such as changes in strain or temperature of the fiber, the phase of the backscattered signal is stable. If a portion of the fiber is stretched, even as minutely stretched by tension or compression from an acoustic wave, the backscattered signal is altered (Hartog 2017).

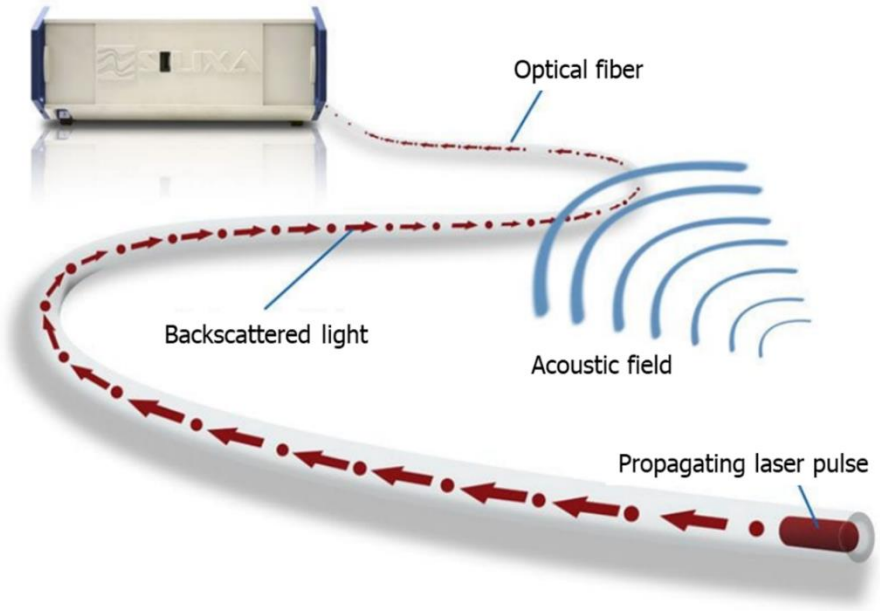

Figure 1.5 Schematic of the distributed acoustic sensing interrogation process. Adapted from Silixa 2021.

Pinpointing the location of a disturbance on the fiber requires knowledge of the two-way travel time of the signal, Δt and the group velocity of light in the fiber, v_g. The group velocity can be estimated by dividing the speed of light in a vacuum by the index of refraction of the fiber optic cable's core, typically 1.468 for a glass fiber. Then, the distance of the disturbance from the interrogator, d_{fiber}, can be computed using Equation 1.1 (Hartog 2017).

$$d_{fiber} = v_g \frac{\Delta t}{2} \tag{1.1}$$

For a fiber optic cable buried in a trench along an international border, Equation 1.1 can be used to determine the location of an intruder given the timing of a disruption in the backscattered signal.

Various types of backscatter occur in fiber optic cables; Figure 1.6 presents the spectral components of a backscattered signal (Krohn et al. 2015). Due to its elastic nature, Rayleigh scattering causes a backward propagation of a portion of the laser pulse at the same frequency as the emitted light pulse. Distributed acoustic sensing utilizes the Rayleigh component of the backscattered signal to detect changes in the optical phase induced by strain or temperature changes. Raman and Brillouin inelastic scattering exhibit useful properties for temperature and strain sensing respectively (Hartog 2017).

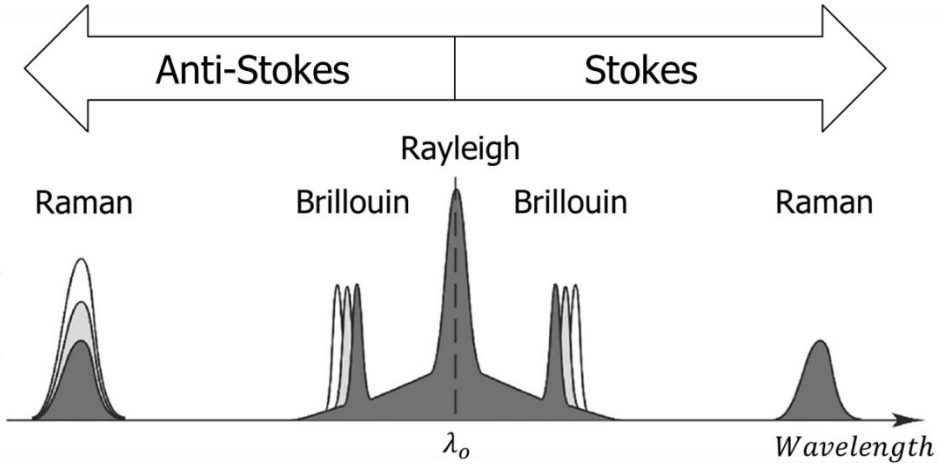

Figure 1.6 Spectral components of backscattered light in fiber optic cables (after Krohn 2015). Reproduced by permission of SPIE.

In practice, the continuous DAS signal is divided into sensing segments called "channels" that usually represent a length of 1 or 2 meters. The length of the channels represents the sampling resolution of the DAS system. The spatial resolution of the DAS measurement is determined by the gauge length of the laser pulses. For example, in dual-pulse DAS systems, the gauge length is determined by the spacing between the two lasers pulses and is typically on the order of 5 to 10 meters. A schematic of a dual-pulse interrogation method is included in Figure 1.7 (Alekseev et al. 2015). In this system, the frequencies of the two pulses are modulated in order to extract the optical phase shift, the fundamental DAS measurand. The dual-pulse interrogation method preserves the polarity of the signal, which enables distinguishing between extending and compressing events in low-frequency DAS sensing. The sampling resolution is typically shorter than the spatial resolution, so that a change in strain or temperature on the fiber at a single point (point O in Figure 1.7) will result in an observed optical phase shift over multiple channels. The gauge length is equal to the distance between the center of pulse A and pulse B in Figure 1.7.

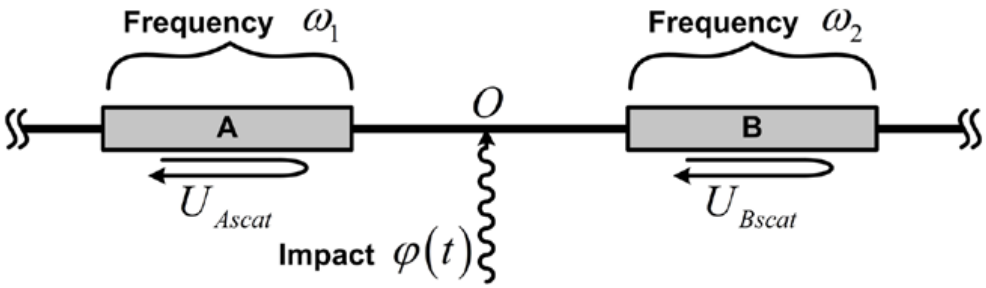

Figure 1.7 Schematic of a frequency modulated dual-pulse interrogation method used for distributed acoustic sensing. Alekseev, et al. 2015. A phase-sensitive optical time-domain reflectometer with dual-pulse diverse frequency probe signal. Laser Physics 25 (6). http://dx.doi.org/10.1088/1054-660X/25/6/065101. Reproduced by permission of IOP Publishing Ltd.

The following relationship can be used to determine the phase detected by the optical interrogator based on the traversed length of a laser pulse *l*, the index of refraction of the fiber *n*, and the wavelength of the laser-emitted light λ (Hicke et al. 2019, Karrenbach et al. 2019).

$$\varphi = \frac{2\pi n l}{\lambda} \tag{1.2}$$

For differential phase measurements, the representative distance light travels is twice the gauge length L_g on an unstrained fiber.

$$\varphi = \frac{4\pi n L_g}{\lambda} \tag{1.3}$$

Karrenbach showed that differentiating the phase leads to the following expression for the change in the Rayleigh backscattered optical phase as a function of axial strain along the fiber, ε.

$$\Delta\varphi = \frac{4\pi n L_g}{\lambda}\varepsilon \tag{1.4}$$

Equation 1.4 reveals that the cumulative change in the DAS optical phase shift, $\Delta\varphi$, is proportional to the axial strain on the fiber. Manufacturers of DAS interrogation systems often provide the instantaneous change in the optical phase shift, $d\varphi/dt$:

$$\frac{d\varphi}{dt} = \frac{4\pi n L_g}{\lambda}\frac{d\varepsilon}{dt} \tag{1.5}$$

Thus, the instantaneous change in the optical phase shift is proportional to the time derivative of strain, or the strain rate. While DAS fundamentally senses strain rate, it can sample at acoustic frequencies (10 kHz and above) and has a high enough sensitivity to detect vibrations associated with noise. Thus, the term "distributed acoustic sensing" was coined, although some scientists prefer the terminology "distributed vibration sensing" (Hartog 2017).

1.2.2. DAS Applications in Upstream Oil and Gas

In recent years, the upstream oil and gas industry has found multiple uses for distributed acoustic sensing. Applications include noise detection (Pakhotina et al. 2020) and microseismic monitoring (Karrenbach et al. 2019) which utilize sampling frequencies on the order of 1 to 10 kHz to detect noise from flow and seismic waves. Purportedly, the first application of distributed acoustic sensing for noise detection occurred in a tight gas well completion in February of 2009 (Molenaar et al. 2012). Researchers at Shell used DAS to monitor the noise associated with setting a bridge plug, firing perforation guns, and flowing fluid through perforations during injection.

To visualize the measurements, the DAS response is typically plotted on a waterfall plot: a heat map of the frequency band energy of the DAS response plotted versus depth and time. Such a plot is included below in Figure 1.8 which shows the DAS response to a single stage of a multi-cluster, hydraulic fracture completion (Pakhotina et al. 2020). In this case, the fiber optic cable is located on the treatment well. Oriented perforating is performed to reduce the risk of shooting through the fiber optic cable prior to injection.

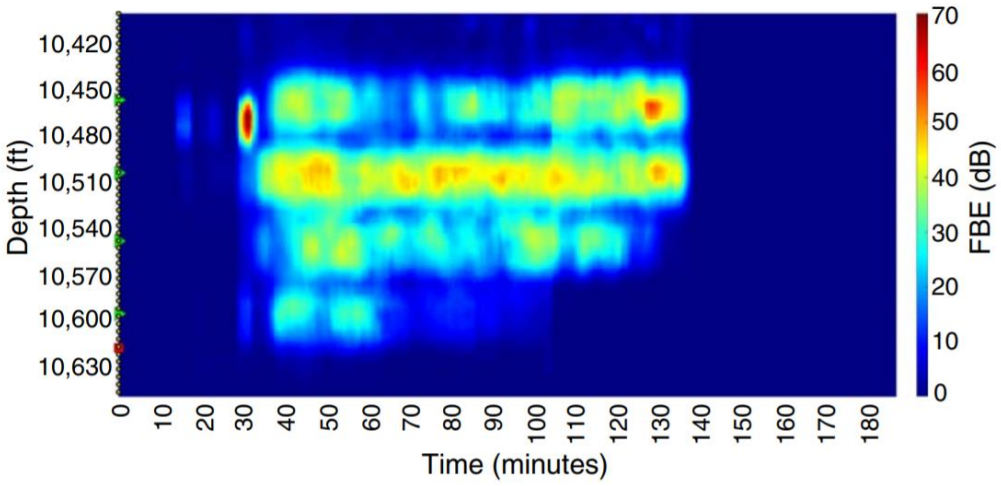

Figure 1.8 A waterfall plot of the DAS frequency band energy versus depth and time used to monitor a multi-cluster hydraulic fracture stage (Pakhotina et al. 2020). Reproduced with permission from SPE.

Pakhotina quantitively interpreted the DAS frequency band energy to allocate flow rates to each perforation cluster over time. The green dots on the depth axis indicate the

location of each of the four clusters in this stage; the red dot indicates the location of the frac plug that isolates the perforation clusters from the prior stage interval. Cluster 1, the cluster of perforations closest to the frac plug, was interpreted to receive the lowest amount of injection volume, while cluster 3 was allocated the highest injection volume. The same fiber optic cable used for noise detection can also be used for LF-DAS cross-well strain rate sensing. The main differences between DAS and LF-DAS as currently used in the oilfield are summarized in Table 1.1.

Table 1.1 Comparison between DAS and LF-DAS monitoring.

Noise monitoring (DAS)	Strain rate monitoring (LF-DAS)
Monitors noise on the treatment well	Monitors far-field strain on a monitor well
High-frequency portion of DAS response interpreted	Low-frequency portion of DAS response interpreted
Frequency band energy computed at ~1 second intervals	Change in optical phase computed at 10 second intervals

DAS sensors have only been utilized in oil and gas wells since 2009. However, the history of low-frequency distributed acoustic sensing in wellbores is even more brief. The following two sections review field cases with published LF-DAS data acquired during offset fracturing operations and numerical simulations of the LF-DAS response to a hydraulic fracture.

1.2.3. Low-Frequency DAS Published Field Cases

Jin and Roy published the first results of the low-frequency DAS response to a hydraulic fracture completion at an offset well (Jin and Roy 2017). They utilized a dual-pulse DAS interrogation method that could detect whether changes in the optical phase shift were positive or negative. As the LF-DAS phase shift is proportional to strain, identifying the sign of the phase shift enables detection of either extension or compression of the fiber optic cable. Plotting the LF-DAS phase shift versus depth and time on a waterfall plot as shown in Figure 1.9, Jin and Roy suggested the response indicated a fracture had intersected the fiber-instrumented monitor well.

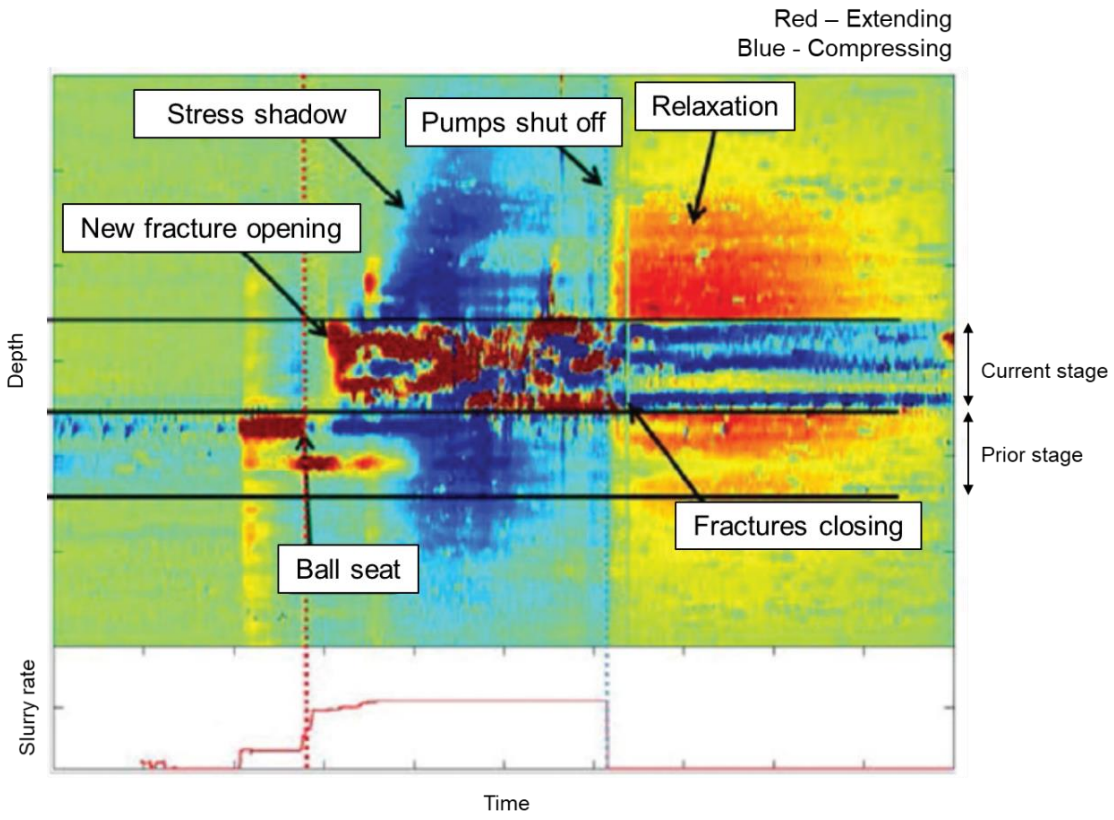

Figure 1.9 Waterfall plot of the low-frequency distributed acoustic sensing response to a far-field propagating hydraulic fracture (top) and corresponding pumping plot (bottom) (after Jin and Roy 2017). Reproduced with permission from SEG.

Notable features of the waterfall plot include: a nearly immediate strain response to the commencement of fracture fluid injection, a wide region of extending fiber that converges to a thin region of extending fiber by intense compressing fiber, and a change in polarity in the signal that corresponds to the end of the fracture stage. Jin and Roy published their interpretation of the LF-DAS waterfall plot within the context of a larger field experiment in the Eagle Ford with the objective of characterizing the hydraulically

fractured reservoir. To characterize fracture geometry and orientation, the researchers mapped the purported fracture hit events from the active completion stage as shown in Figure 1.10. The drawings indicated that the fractures were propagating essentially parallel to each other in the direction of maximum horizontal stress. Fracture hit events up to 1,500 feet away were observed. The first two stages on well P5 were not monitored; the absence of lines drawn from those stages to the observation well does not indicate that the fractures did not propagate beyond 1,500 feet (Raterman et al. 2018).

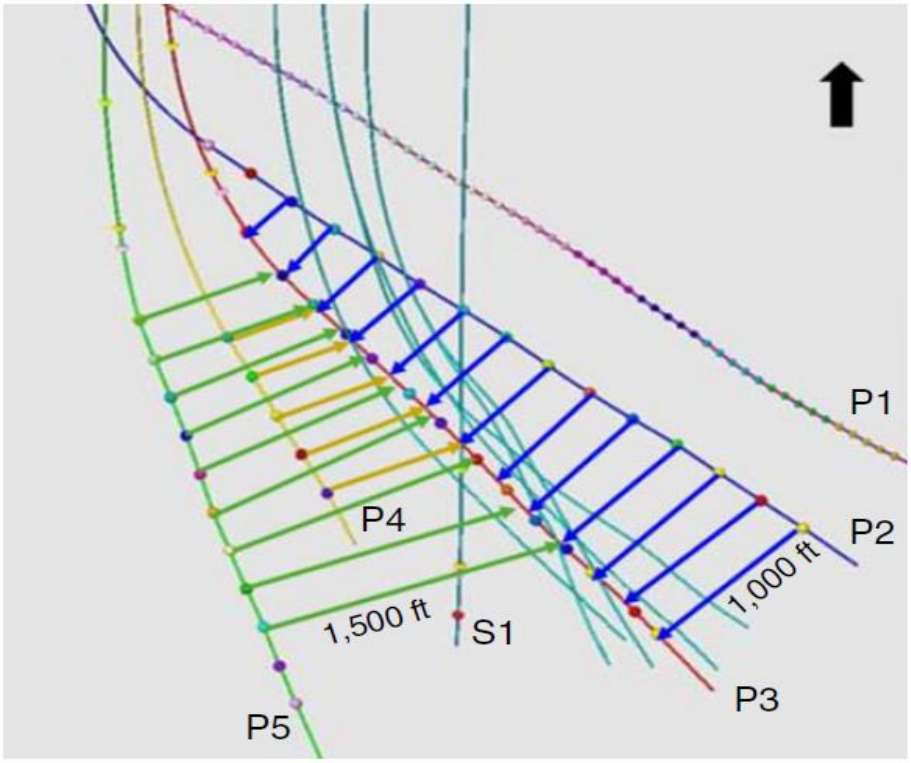

Figure 1.10 Map view of LF-DAS interpreted fracture intersections at the monitor well P3, displayed in red (Raterman et al. 2018). Reproduced with permission from SPE.

Ugueto and other researchers corroborated the findings of Jin and Roy by publishing LF-DAS results from the Montney formation (Ugueto et al. 2019). Their plots, as shown in Figure 1.11, included time, depth, and phase shift axis labels that gave an indication of the spatial and temporal resolution and magnitude of the LF-DAS data. The strain rate at well H responds quickly to the start and end of pumping at well G, located 650 feet away. In their publication, Ugueto et al. suggested the presence of three fracture

intersection events in a single stage as labeled on the waterfall plot as perforation clusters 4.1 – 4.3.

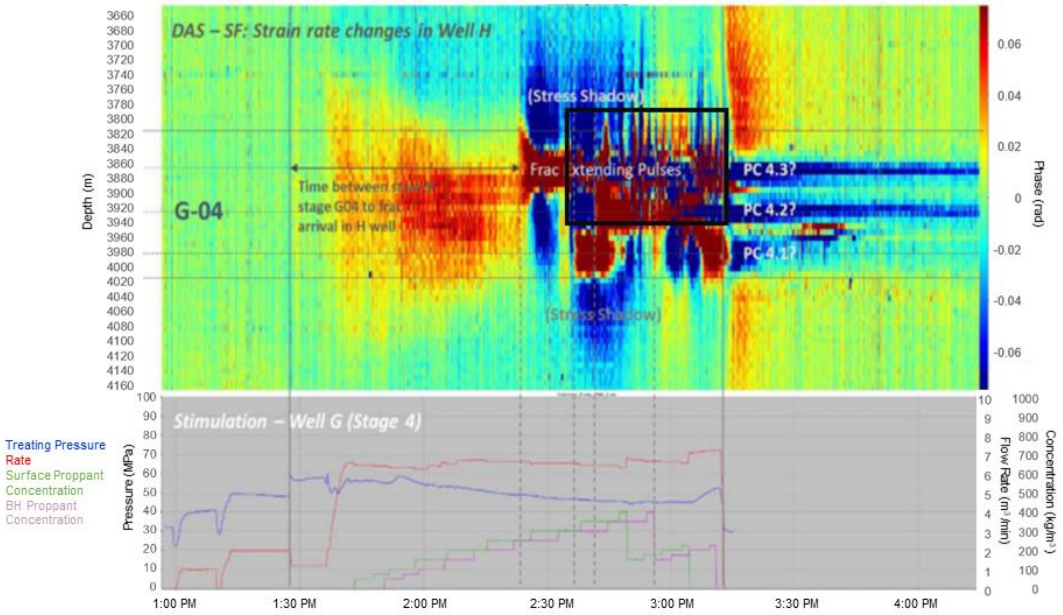

Figure 1.11 LF-DAS waterfall plot with corresponding offset well pumping plot (after Ugueto et al. 2019). Reproduced with permission from SPE.

Furthermore, researchers at Optasense and Devon Energy acquired distributed acoustic sensing data during hydraulic fracture operations in a Meramec field development (Karrenbach et al. 2019). They published the ability of the low-frequency portion of the DAS signal to detect temperature changes in addition strain changes. They compared LF-DAS derived temperature measurements during offset hydraulic fracturing

operations to temperature measurements from a co-located distributed temperature sensor (DTS), shown in Figure 1.12a and Figure 1.12b respectively. LF-DAS measures only changes in temperature over the gauge length, while DTS detects the absolute temperature. However, comparing the temperature changes from the initial baseline temperature shows good agreement between LF-DAS based and DTS measured temperature changes. The LF-DAS based measurement has less noise; the LF-DAS waterfall plot is crisper than the DTS waterfall plot, highlighting the elevated sensitivity of LF-DAS to temperature changes compared to DTS.

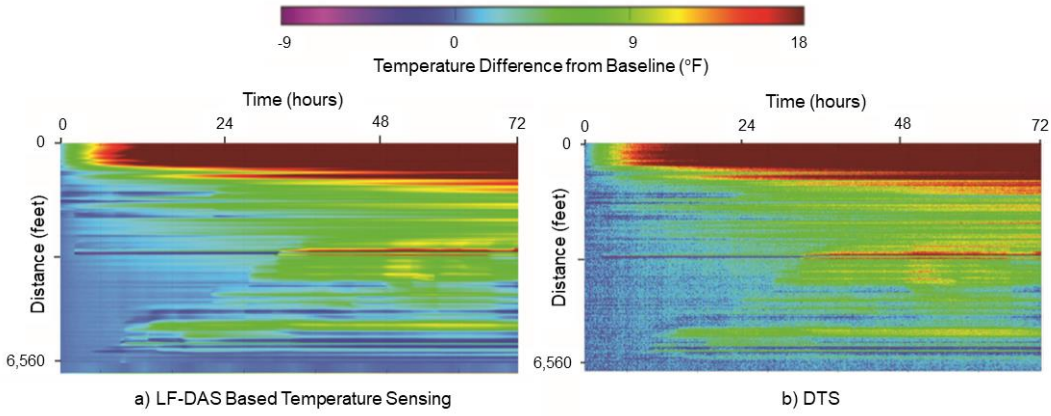

Figure 1.12 A comparison between a co-located a) LF-DAS derived temperature measurement and b) distributed temperature sensing (DTS) measurement (after Karrenbach et al. 2019). Reproduced with permission from SEG.

Researchers from Devon Energy presented sealed wellbore pressure monitoring as a low-cost alternative to LF-DAS for diagnosing the timing of the first fracture intersection event, or frac hit (Haustveit et al. 2020). Sealed wellbore pressure monitoring is conducted by recording the surface casing pressure of an unstimulated horizontal well that is filled with water during offset fracture operations. Haustveit et al. correlated surface pressure perturbations with the onset of the characteristic narrow band of extending fiber in LF-DAS signatures as shown in Figure 1.13. The onset of pressure changes occurs almost simultaneously with the convergence of the LF-DAS region of extending fiber (marked with the black arrow). However, some offset exists between this point and the most obvious increase in the pressure signal at the time where *dP/dt* increases dramatically.

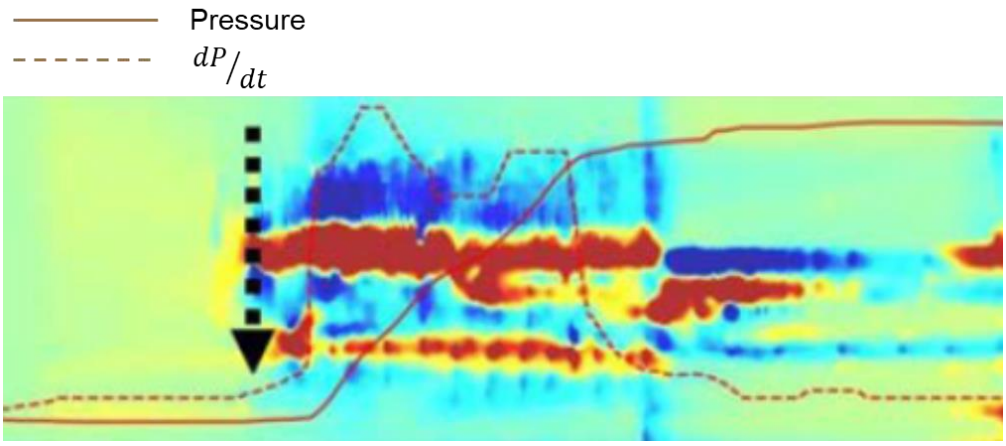

Figure 1.13 The surface pressure and its time derivative of an offset monitor well compared synchronously to LF-DAS strain rate signals from the same monitor well (after Haustveit et al. 2020). Reproduced with permission from SPE.

While Raterman et al. used the locations of the frac hit events to map out fracture azimuths, Haustveit et al. used the timing of frac hit events to study cluster uniformity. They suggested that for the same well spacing and injection rate, a longer time to a frac hit indicates uniformity in cluster fluid distribution, while a rapidly occurring frac hit indicates a single dominant fracture received most of the injection fluid. Thus, they used the injected volume at the time of the first frac hit, or the "volume to first response," as a proxy for cluster uniformity. In their field case, they showed that the volume to first response correlated positively with production and used the results to evaluate completion designs (Haustveit et al. 2020).

1.2.4. Low-Frequency DAS Numerical Modeling

A flurry of activity related to modeling the LF-DAS response during offset hydraulic fracturing operations quickly followed the publication of the aforementioned field cases. Researchers at Chevron modeled far-field strain changes due to propagating hydraulic fractures using the displacement discontinuity method (Zhang et al. 2020). Chevron participated in the Department of Energy funded Hydraulic Fracture Test Site in the Permian Bain, and the investigators sought to interpret the LF-DAS responses acquired in that project. In Figure 1.14 the modeled axial strain rate along the fiber optic cable with an intersecting hydraulic fracture is compared to the field-measured LF-DAS signal.

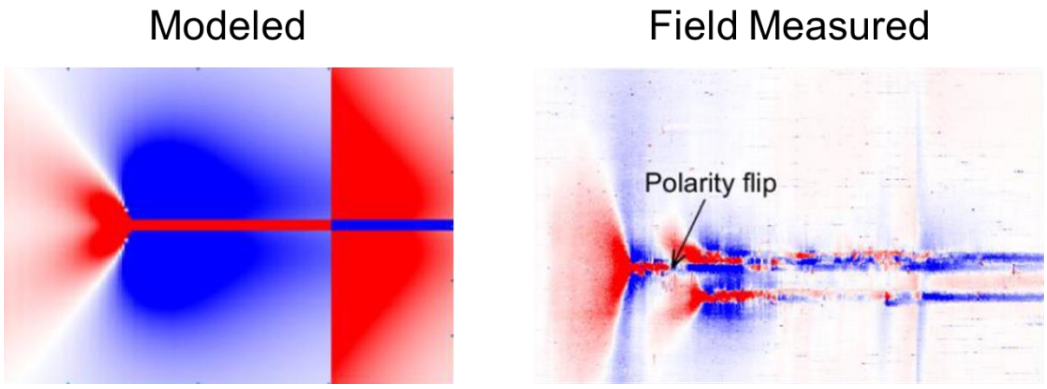

Figure 1.14 A comparison of modeled strain rates and a field-measured LF-DAS signal at the hydraulic fracture test site in the Permian Basin. Red indicates extending fiber, blue indicates compressing fiber (after Zhang et al. 2020). Reproduced with permission from AAPG.

The waterfall plots have qualitative similarities. Each begins with a wide region of extending fiber (red) that converges to a narrow region of extending fiber surrounded by compressing fiber (blue). The timing of this convergence corresponded to the time of a fracture intersection, or frac hit. These modeling results supported Jin and Roy's assertion that the convergence of the extending portion of the LF-DAS signal indicates a frac hit. Other numerical studies utilizing similar methods reached similar conclusions, further supporting Jin and Roy's interpretation of strain rate patterns (Liu et al. 2020, Shahri et al. 2021).

It is important to consider how the fiber optic sensors are deployed operationally in oilfield applications. Figure 1.15 shows a schematic of a permanent fiber optic cable deployment next to an image of the drilling rig floor during an actual fiber installation. Encased in a gel-filled, stainless-steel capillary tubing, the fiber optic cable is deployed by being externally clamped to the pipe being run in the wellbore. Often, the stainless-steel tubing is encased in a protective plastic jacket when run on the casing. Each of these layers (gel, stainless-steel tubing, and plastic jacket) function to protect the fiber optic cable from damage during installation. After the casing and attached fiber are lowered into the wellbore, the annulus between the casing and wellbore is cemented. It is significant to note that, to date, numerical studies of the LF-DAS response have not considered strain transfer effects from the rock-cement-casing system, nor strain transfer from the casing to the fiber encased in a plastic-coated, gel-filled, stainless-steel protective tubing.

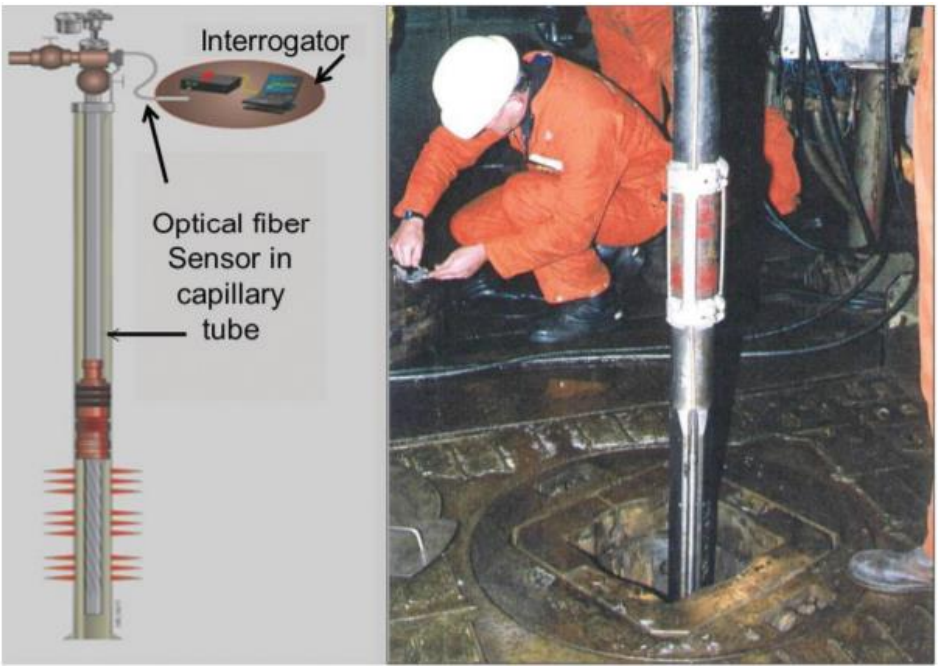

Figure 1.15 In DAS oilfield applications, the fiber optic cable is typically clamped externally to the casing or tubing and run in the hole (Krohn et al. 2015). Reproduced with permission from SPIE.

1.3. Problem Statement

In summary, LF-DAS has the potential to provide information on the timing and location of frac hit events. The time and location of frac hits inform characterization of fracture azimuths, fracture geometry at one point in time, and the uniformity of injection fluid distributions in an offset multi-cluster stimulation. However, questions remain about the LF-DAS response to propagating hydraulic fractures. Notably, no laboratory experiments have been presented that confirm the standard interpretation of the timing of fracture intersection events from LF-DAS data. Numerical modeling studies provide a

strong case that the industry does have the correct interpretation, but the numerical models fail to reproduce much of the complexity seen in the field data. Is it possible that the industry is misinterpreting the timing of frac hit events due to simplified models? The research in this work seeks to answer this question by conducting laboratory experiments measuring offset strain changes due to a propagating fracture. These experiments can provide insights into the complexity of observed LF-DAS signals. Additionally, current interpretations of LF-DAS data provide an estimate of the fracture front at only one moment. Sealed wellbore pressure monitoring can purportedly do the same, estimating the timing of a frac hit event at a fraction of the cost of acquiring LF-DAS data. It can be argued that sealed wellbore pressure monitoring provides a cost-effective alternative to LF-DAS to acquire a similar dataset. The value of a LF-DAS acquisition can be increased by extracting more information from the data, such as how the fracture geometry evolves over time. The research presented in this dissertation includes linear elastic modeling of the strain on fiber optic cables due to a far-field hydraulic fracture. The models provide insights into characterizing hydraulic fracture geometry evolution from the measured strain data.

Finally, nearly all published LF-DAS interpretations assume that the signal corresponds to the strain rate, although it is well-documented that the LF-DAS phase is altered in response to changes in temperature. As cool fracture fluid injected at high rates intersects a monitor well instrumented with LF-DAS sensors, it is probable that the temperature along the fiber is altered. How significant are these temperature changes

relative to strain changes on the LF-DAS response? And what is the sensitivity of LF-DAS sensors to temperature and strain changes?

1.4. Objective and Organization of Dissertation

This work seeks to answer these questions by investigations into the nature of the LF-DAS signal via laboratory experiments and numerical modeling. A summary of pertinent background theory is provided in Chapter 2. Chapter 3 details the methodology for a laboratory-scale hydraulic fracture experiment. In this experiment, a radial hydraulic fracture propagates toward fiber optic strain sensors embedded in an 8-inch block of transparent epoxy. The placement of the strain sensors relative to the hydraulic fracture are designed to correspond to LF-DAS field installations. Chapter 4 presents the experimental results, comparing measured fracture radius, pressure, and far-field strains to theory. This chapter also includes strain and strain rate waterfall plots constructed from the experimental data that illuminate features of the LF-DAS response. Chapter 5 develops a methodology to estimate fracture geometry evolution with time from LF-DAS strain rate data. The method was validated against the experimental data and applied to a field-case for dynamic fracture geometry characterization. In Chapter 6, learnings from the experiments are applied to numerical modeling of the LF-DAS response from a limited-entry type hydraulic fracture completion in order to investigate temperature effects on low-frequency distributed acoustic sensors. The conclusions from the research and suggestions for future work are discussed in Chapter 7.

2. BACKGROUND THEORY

In this chapter, relevant background theory is presented that provides the groundwork for the experimental and numerical studies. Section 2.1 supplies an overview of linear elastic theory and the models used to simulate the strain response due to a hydraulic fracture. In Section 2.2, pertinent information regarding the fiber Bragg grating strain sensors used in the experiments is reviewed. Section 2.3 introduces the thermal model used in the numerical study of thermal effects on LF-DAS sensors. The study on thermal effects, discussed in Chapter 6, considers the contributions of both strain and temperature changes on the low-frequency distributed acoustic sensing response.

2.1. Linear Elastic Modeling

The experiments in this work propagate a fracture towards an array of embedded strain sensors, simulating the LF-DAS response. To interpret both the experiments and LF-DAS field responses requires models of the strain induced by hydraulic fracturing on the fibers. In this section, three types of linear elastic models are presented to simulate the strain induced by a hydraulic fracture:

1. An analytic solution for a fracture with radial geometry (Sneddon 1946),
2. A finite element model,
3. And a displacement discontinuity method (DDM) model.

Table 2.1 provides an overview of each of the models: the domain they simulate and how they are used in this research.

Table 2.1 Overview of employed linear elastic models.

Model	Domain	Uses
Sneddon	Single, radial crack in an infinite, homogenous domain	Validate other models, simulate the experiments, and inform field interpretations
Finite Element	Single, radial crack in a finite, homogenous block	Model the boundary effects of the finite fracture specimen
DDM	Multiple cracks in an infinite, homogenous domain	Model multiple propagating fractures in a multi-cluster completion

The bases of the models are the fundamental linear elastic equations of an equilibrium, stress-displacement relations, and elastic stress-strain relations. These are derived here for the sake of thoroughness. In cartesian coordinates, the equations of equilibrium can be derived by considering a summation of forces on a three-dimensional block. Figure 2.1 illustrates the free body diagram for a sum of forces on an elemental block that is a part of a larger volume undergoing deformation. The normal stresses in the *x*, *y*, and *z* directions are indicated by σ. The shear stresses are given as τ_{xy}, τ_{xz}, and τ_{yz}. Equilibrium equations in each direction are given by:

$$\sum F_x = 0 \tag{2.1}$$

$$\sum F_y = 0 \tag{2.2}$$

$$\sum F_z = 0 \tag{2.3}$$

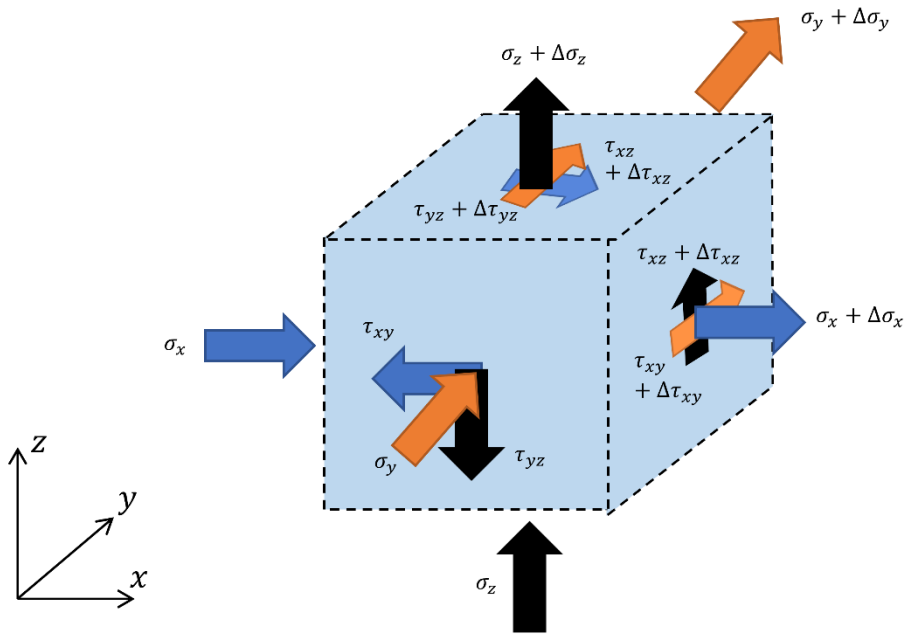

Figure 2.1 Schematic of the free body diagram used to develop the equilibrium equations of elasticity. Blue, orange, and black arrows correspond to forces in the x, y, and z directions. Shown are all normal stresses as well as the shear stresses on the visible faces of the cube.

Stress is defined as the force per unit area.

$$\sigma = \frac{F}{A} \tag{2.4}$$

Considering that the element in Figure 2.1 has dimensions of Δx, Δy, and Δz, the summation of forces in the x direction can be written as:

$$(\sigma_x + \Delta\sigma_x - \sigma_x)\Delta y\Delta z + (\tau_{xy} + \Delta\tau_{xy} - \tau_{xy})\Delta x\Delta z + \tag{2.5}$$

$$(\tau_{xz} + \Delta\tau_{xz} - \tau_{xz})\Delta x\Delta y = 0$$

Canceling out like terms, and dividing by Δx, Δy, and Δz, and taking the limit as the size of the volumetric element approaches zero yields:

$$\frac{\partial\sigma_x}{\partial x} + \frac{\partial\tau_{xy}}{\partial y} + \frac{\partial\tau_{xz}}{\partial z} = 0 \qquad 2.6$$

Performing similar operations in the *y* and *z* directions produces:

$$\frac{\partial\sigma_y}{\partial y} + \frac{\partial\tau_{xy}}{\partial x} + \frac{\partial\tau_{yz}}{\partial z} = 0 \qquad 2.7$$

$$\frac{\partial\sigma_z}{\partial z} + \frac{\partial\tau_{xz}}{\partial x} + \frac{\partial\tau_{yz}}{\partial y} = 0 \qquad 2.8$$

Equations 2.6 through 2.8 represent the equilibrium equations of linear elasticity, neglecting body forces (for example, magnetic or gravitational forces).

Displacement is defined by the distance a particle within the element pictured in Figure 2.1 moves as deformation occurs. Displacements in the *x*, *y*, and *z* directions are given by *u*, *v*, and *w* respectively. The relationships between strains and displacements are defined as (Morita 2021):

$$\varepsilon_x = \frac{\partial u}{\partial x} \qquad 2.9$$

$$\varepsilon_y = \frac{\partial v}{\partial y} \qquad 2.10$$

$$\varepsilon_z = \frac{\partial w}{\partial z} \qquad 2.11$$

$$\gamma_{xy} = \frac{1}{2}\left(\frac{\partial u}{\partial y} + \frac{\partial v}{\partial x}\right) \qquad 2.12$$

$$\gamma_{xz} = \frac{1}{2}\left(\frac{\partial u}{\partial z} + \frac{\partial w}{\partial x}\right) \quad 2.13$$

$$\gamma_{yz} = \frac{1}{2}\left(\frac{\partial v}{\partial z} + \frac{\partial w}{\partial y}\right) \quad 2.14$$

Here, ε is a normal strain and γ is a shear strain. Finally, for a homogeneous medium, the linear relationships between stress and strain are given by Hooke's law through the use of two elastic constants: Young's modulus E and Poisson's ratio ν (Morita 2021).

$$\varepsilon_x = \frac{1}{E}(\sigma_x - \nu\sigma_y - \nu\sigma_z) \quad 2.15$$

$$\varepsilon_y = \frac{1}{E}(\sigma_y - \nu\sigma_x - \nu\sigma_z) \quad 2.16$$

$$\varepsilon_z = \frac{1}{E}(\sigma_z - \nu\sigma_x - \nu\sigma_y) \quad 2.17$$

$$\gamma_{xy} = \frac{1+\nu}{E}\tau_{xy} \quad 2.18$$

$$\gamma_{xz} = \frac{1+\nu}{E}\tau_{xz} \quad 2.19$$

$$\gamma_{yz} = \frac{1+\nu}{E}\tau_{yz} \quad 2.20$$

Equations 2.6 through 2.20 are the fifteen equations of elasticity. If the elastic moduli of a homogeneous element are known, then there are 15 unknowns: 6 stresses, 6 strains, and 3 displacements. The radial fracture model provides an analytic solution to this system of equations, whereas the finite element and displacement discontinuity method solve them with numerical methods.

2.1.1. Radial Hydraulic Fracture Propagation

The following discussion reviews the theory of radial fracture propagation based on linear elastic theory. In 1945, Harding and Sneddon published a solution for the stresses and displacements in a three-dimensional, semi-infinite, linear elastic medium due to a rigid circular punch (Harding and Sneddon 1945). Using a similar approach, Sneddon then extended the solution to describe deformations due to a circular crack filled with pressurized fluid (Sneddon 1946). The following section provides an overview of the derivation for the purpose of understanding the parameters in Sneddon's solution and his basic assumptions. Subsequent sections highlight the portions of his solution relevant to radial fracture propagation and the displacements normal to the fracture plane, in the direction of the axis of the fiber optic cables as deployed in the experiments and in LF-DAS.

Sneddon considered a circular crack centered on the plane $z = 0$ in a semi-infinite, homogeneous, linear-elastic material with cylindrical coordinates. The location of Sneddon's crack in both cartesian and cylindrical coordinates is illustrated below. The crack radius is given by parameter c, not to be confused with the radial coordinate, r.

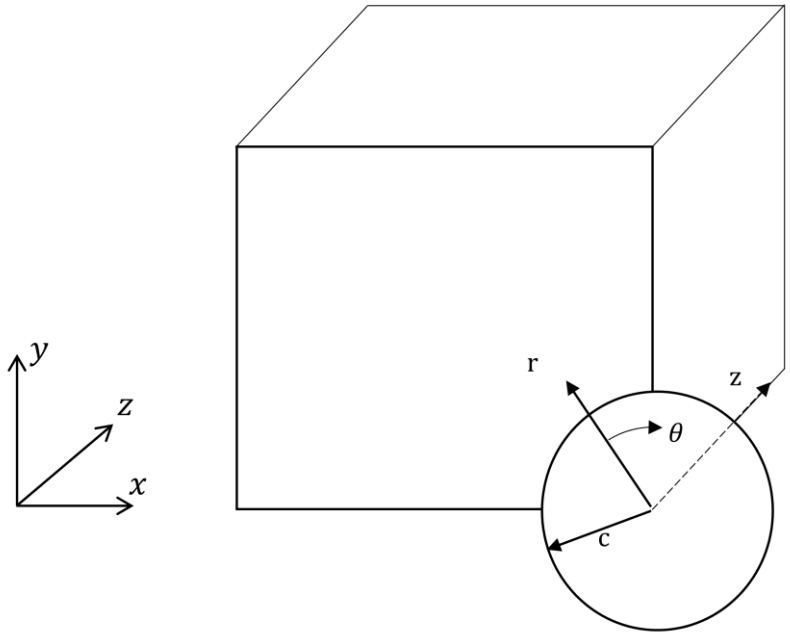

Figure 2.2 The coordinate system for Sneddon's penny shaped crack.

Considering the summation of forces around a cylindrical element, the equilibrium equations in the radial, angular, and depth directions are expressed as follows, neglecting body forces:

$$\frac{\partial \sigma_r}{\partial r} + \frac{1}{r}\frac{\partial \tau_{r\theta}}{\partial \theta} + \frac{\partial \tau_{rz}}{\partial z} + \frac{\sigma_r - \sigma_\theta}{r} = 0 \qquad 2.21$$

$$\frac{\partial \tau_{rz}}{\partial r} + \frac{1}{r}\frac{\partial \tau_{\theta z}}{\partial \theta} + \frac{\partial \sigma_z}{\partial z} + \frac{\tau_{rz}}{r} = 0 \qquad 2.22$$

$$\frac{\partial \tau_{r\theta}}{\partial r} + \frac{1}{r}\frac{\partial \sigma_\theta}{\partial \theta} + \frac{\partial \tau_{\theta z}}{\partial z} + \frac{2\tau_{r\theta}}{r} = 0 \qquad 2.23$$

Sneddon recognized the axisymmetric nature of the problem, such that $\tau_{r\theta}$, $\tau_{\theta z}$, and terms with $\frac{\partial}{\partial\theta}$ vanish. Equation 2.23 becomes trivial, and Equations 2.21 and 2.22 become:

$$\frac{\partial\sigma_r}{\partial r}+\frac{\partial\tau_{rz}}{\partial z}+\frac{\sigma_r-\sigma_\theta}{r}=0 \tag{2.24}$$

$$\frac{\partial\tau_{rz}}{\partial r}+\frac{\partial\sigma_z}{\partial z}+\frac{\tau_{rz}}{r}=0 \tag{2.25}$$

The axisymmetric strain-displacement equations are:

$$\varepsilon_r=\frac{\partial u_r}{\partial r} \tag{2.26}$$

$$\varepsilon_\theta=\frac{u_r}{r} \tag{2.27}$$

$$\varepsilon_z=\frac{\partial u_z}{\partial z} \tag{2.28}$$

$$\gamma_{zr}=\frac{\partial u_r}{\partial z}+\frac{\partial u_z}{\partial r} \tag{2.29}$$

And the stress strain relations are:

$$\varepsilon_r=\frac{1}{E}[\sigma_r-\nu(\sigma_\theta+\sigma_z)] \tag{2.30}$$

$$\varepsilon_\theta=\frac{1}{E}[\sigma_\theta-\nu(\sigma_r+\sigma_z)] \tag{2.31}$$

$$\varepsilon_z=\frac{1}{E}[\sigma_z-\nu(\sigma_\theta+\sigma_r)] \tag{2.32}$$

$$\tau_{rz}=G\gamma_{rz} \tag{2.33}$$

Sneddon also imposed the following boundary conditions:

- a constant pressure P_o applies over $r<c$ on the plane $z=0$,

- the displacement $u_z = 0$ for $r > c$ on the plane $z = 0$, and
- all stresses tend to zero as $r \to \infty$ and $z \to \infty$.

Equations 2.24 through 2.33 consists of 10 equations with 10 unknowns. This system of equations involves partial differential equations of multiple dependent variables. Harding and Sneddon showed that the number of dependent variables could be reduced by rewriting the stresses σ_r, σ_z, σ_θ, and τ_{zr} as a function of a single variable Φ called a "stress function." They showed that Equations 2.34 through 2.37 describe each stress component as a function of derivatives of Φ, where the notation Φ_z indicates $\partial\Phi/\partial$z and $\nabla^2 = \partial^2/\partial r^2 + 1/r*\partial/\partial r + \partial^2/\partial z^2$ (Harding and Sneddon 1945).

$$\sigma_r = \lambda\nabla^2\Phi_z - 2(\lambda+\mu)\Phi_{rrz} \tag{2.34}$$

$$\sigma_z = (3\lambda+4\mu)\nabla^2\Phi_z - 2(\lambda+\mu)\Phi_{zzz} \tag{2.35}$$

$$\sigma_\theta = \lambda\nabla^2\Phi_z - 2(\lambda+\mu)\frac{1}{r}\Phi_{rz} \tag{2.36}$$

$$\tau_{zr} = (\lambda+2\mu)\frac{\partial}{\partial r}\nabla^2\Phi - 2(\lambda+\mu)\Phi_{zzr} \tag{2.37}$$

λ and μ are Lamé's elastic constants which can be expressed in terms of Young's modulus and Poisson's ratio. The stress and stress function relationships are defined to satisfy the equilibrium equations. Substituting Equations 2.34 through 2.37 into the Equations 2.21 and 2.22 yields the trivial solution.

Implicit in the assumptions of linear elasticity is that the medium being deformed is continuous. This assumption of smooth deformation is formalized by stating that the second derivatives of the strain field must exist. The set of equations describing the continuity of the deformed medium are called the compatibility equations. Harding and

Sneddon invoke the compatibility equations to show that Φ must be a solution to the biharmonic equation.

$$\nabla^4 \Phi = 0 \qquad 2.38$$

Here, ∇^4 indicates $\nabla^2(\nabla^2)$. Any function Φ that satisfies Equation 2.38 describes the state of stress for a certain corresponding set of boundary conditions. For example, $\Phi=z^3$ defines a simple triaxial stress state where σ_r, σ_z, and σ_θ are constant and τ_{zr} is zero. This can be proved by substitution into Equations 2.34 through 2.37.

Sneddon made a major contribution by presenting the stress function that corresponds to the boundary conditions of a pressurized radial fracture in an infinite medium. To find the stress function, he utilized the Hankel transform and proved that the solution to the stress function Φ has the form of:

$$\Phi = \int_0^\infty \xi G J_0(\xi r) d\xi \qquad 2.39$$

In this equation, J_0 is a Bessel function of the first kind, ξ is a parameter that represents the radial coordinate in Hankel space, and G is a function of the form:

$$G = (A + Bz)e^{-\xi z} \qquad 2.40$$

Where A and B are constants solved from the boundary conditions. To produce a general solution, Sneddon non-dimensionalized the cylindrical coordinates in real and Hankel space according to the crack radius as follows:

$$\zeta = \frac{z}{c} \qquad 2.41$$

$$\rho = \frac{r}{c} \tag{2.42}$$

$$\eta = \frac{\xi}{c} \tag{2.43}$$

Sneddon then solved for parameters *A* and *B* that satisfied the boundary conditions as:

$$A = \frac{2\nu B}{\eta c} \tag{2.44}$$

$$B = \frac{1}{\eta^2}\frac{2P_o c^4(1+\nu)(1-2\nu)}{\pi E}\left(\frac{cos\eta}{\eta} - \frac{sin\eta}{\eta^2}\right) \tag{2.45}$$

The full solutions for stresses and displacements throughout the semi-infinite, linear-elastic medium are given in Sneddon's 1946 publication in Equations 3.6.1 through 3.6.5 and 3.6.9. For the purpose of this research, the most pertinent solution is that for the displacement in the z direction, normal to the plane of the fracture. This is given by:

$$u_z = \frac{-4P_o c(1-\nu^2)}{\pi E}\int_0^\infty \left(1 + \frac{\zeta\eta}{2(1-\nu)}\right)\left(\frac{cos\eta}{\eta} - \frac{sin\eta}{\eta^2}\right)e^{-\zeta\eta}J_0(\rho\eta)d\eta \tag{2.46}$$

On the crack plane, corresponding to $\frac{z}{c} = \zeta = 0$, Equation 2.46 becomes difficult to integrate numerically due to the integrand's oscillatory nature and the vanishing of the dampening term $e^{-\zeta\eta}$. By the boundary conditions, $u_z = 0$ for $r \geq c$ for $z = 0$. For displacements on the crack face, $r < c$ on the plane containing the fracture, Sneddon provided a simplified form of equation for the normal displacement as:

$$[u_z]_{z=0} = \frac{4P_0(1-\nu^2)}{\pi E}\sqrt{c^2 - r^2} \tag{2.47}$$

The crack width at any location on the crack surface is twice the normal displacement computed by the above equation. At the center of the crack, $r = 0$, the maximum fracture width is computed by:

$$w = \frac{8P_0c(1-\nu^2)}{\pi E} \qquad 2.48$$

Based on Equation **2.47**, Sneddon recognized that the so called "penny-shaped" crack is an ellipsoid whose volume can be computed by:

$$V_f = \frac{16P_0c^3(1-\nu^2)}{3E} \qquad 2.49$$

It is of interest to compare the strains measured by the fiber strain sensors to Sneddon theory. To do so requires combining Equations 2.28 and 2.46 to form:

$$\varepsilon_z = \frac{d}{dz}\frac{-4P_0c(1-\nu^2)}{\pi E}\int_0^\infty \left(1+\frac{\zeta\eta}{2(1-\nu)}\right)\left(\frac{cos\eta}{\eta}-\frac{sin\eta}{\eta^2}\right)e^{-\zeta\eta}J_0(\rho\eta)d\eta \qquad 2.50$$

The non-dimensionality of Equation 2.50 provides a basis for scaling experimental results from lab scale to field scale. To the extent that both reservoir rock and the laboratory fracture specimens can be approximated as infinite, homogeneous, linear-elastic medium, the mechanical deformations due to a circular crack are the same when normalized by the length dimension. Sneddon normalized the geometry coordinates by the crack radius, *c*. In the context of LF-DAS offset well monitoring, it is much more useful to normalize by the radial coordinate, *r*. Assuming a fracture is centered at a treatment well, the radial well spacing between the monitor well and center of the fracture is a known quantity, and can be computed by:

$$r = \sqrt{\Delta h^2 + \Delta l^2} \tag{2.51}$$

where Δh and Δl are the vertical and lateral offset between the treatment and monitor wells. Defining new dimensionless parameters

$$z_D = \frac{z}{r} \tag{2.52}$$

$$R_D = \frac{c}{r} \tag{2.53}$$

and expressing Sneddon's ζ and ρ in terms of these dimensionless parameters

$$\zeta = \frac{z}{c} \times \frac{r}{r} = \frac{z}{r} \times \frac{r}{c} = \frac{z_D}{R_D} \tag{2.54}$$

$$\rho = \frac{r}{c} = \frac{1}{R_D} \tag{2.55}$$

allows expressing Equation 2.50 as follows.

$$\varepsilon_z = \frac{d}{dz} \frac{-4P_o c(1-\nu^2)}{\pi E} \int_0^\infty \left(1 + \frac{z_D \eta}{2R_D(1-\nu)}\right) \left(\frac{cos\eta}{\eta} - \frac{sin\eta}{\eta^2}\right) e^{-z_D \eta / R_D} J_0\left(\frac{\eta}{R_D}\right) d\eta \tag{2.56}$$

No analytic solution has been published for Equation 2.46 or 2.56, and Wolfram Mathematica could not compute one programmatically. In this work, Equation 2.56 is solved by Matlab's numerical integration function and subsequent differentiation by the central difference method.

The above formulae provide a complete description of the deformation due to a static, circular crack. A model for a propagating crack requires a failure criterion. A common failure criterion in fracture modeling consists of a mode I stress intensity factor. The pressure required to extend the crack is given by (Smith and Montgomery 2015):

$$P_{cr} = K_{IC}\sqrt{\frac{\pi}{4R}} \quad 2.57$$

Combining Equations 2.57 and 2.49 to eliminate crack radius yields an expression for pressure as a function of injected volume.

$$P_{net} = \left[\frac{\pi^3 K_{IC}^6 (1-v^2)E^2}{12EV}\right]^{\frac{1}{5}} \quad 2.58$$

Combining Equations 2.49 and 2.57 to eliminate pressure yields:

$$R = \left(\frac{3V_f E'}{8\sqrt{\pi}K_{IC}}\right)^{\frac{2}{5}} \quad 2.59$$

Equations 2.58 and 2.59 were used to model the fracture pressure and geometry as a function of injected volume and epoxy mechanical properties. The models are compared to the experimentally measured pressures and radii in Chapter 4.

2.1.2. Linear Elastic Finite Element Modeling

Sneddon's radial fracture model assumes a crack in an infinite medium. The infinite-medium approximation is not valid for the 8-inch cubic fracture specimens in the experiments. To account for boundary effects associated with the finite size of the epoxy fracture specimens, we employed linear elastic finite element modeling. The finite element method can numerically solve the linear elastic equations of equilibrium continuity, and stress-strain relationships (Morita, 2021). We used Abaqus FEA, a commercially available simulator, to solve the equations of elasticity as shown in Equations 2.6 through 2.20 (2018).

Figure 2.3 illustrates the simulated domain. Symmetry in the *X*, *Y*, and *Z* planes permits simulation of only 1/8th of the epoxy fracture specimen. The fracture specimen was

discretized in 400,000-500,000 hexahedral elements with 8 nodes. The *Z* plane which contains the fracture of radius *R* is shown with normal displacements colored. The following boundary conditions were applied to obtain this result:

- a constant pressure P_o applies over $\sqrt{x^2 + y^2} \leq R$ on the plane $z = 0$,
- the symmetry condition $u_z = 0,\ \tau_{zx} = 0, \tau_{zy} = 0$ for $\sqrt{x^2 + y^2} > R$ on the plane $z = 0$,
- the symmetry condition $u_x = 0,\ \tau_{xy} = 0, \tau_{xz} = 0$ on the plane $x = 0$, and
- the symmetry condition $u_y = 0,\ \tau_{yx} = 0, \tau_{yz} = 0$ on the plane $y = 0$.

As no confining pressure was applied to the blocks in the experiments, the outer faces of the block were modeled as free boundaries.

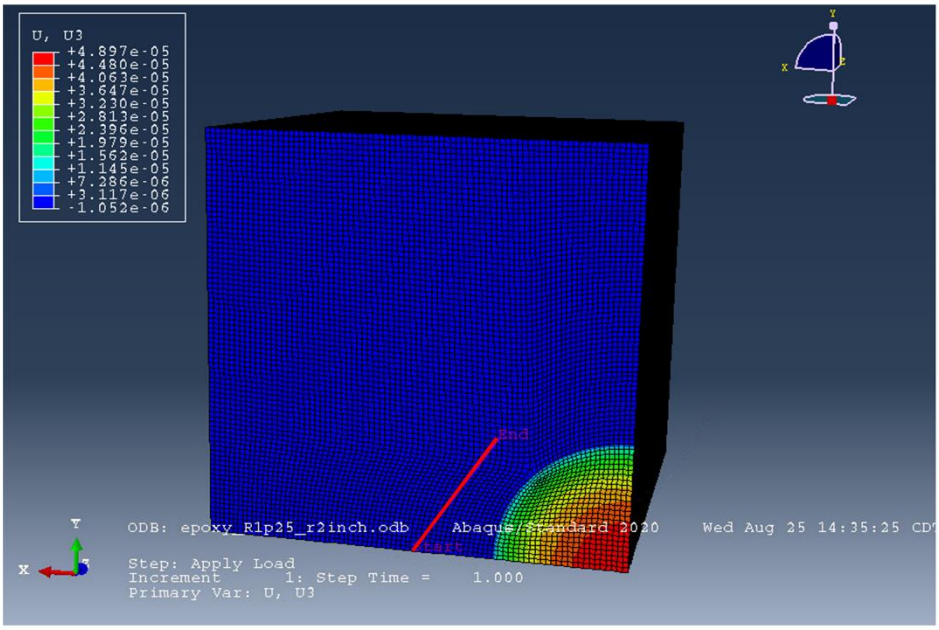

Figure 2.3 Domain of a finite element model of the fracture specimen. The color corresponds to displacement normal to the crack surface.

The red line in Figure 2.3 is parallel with the *x* axis 2 inches offset from the center of the block. This geometry corresponds to the location of the fiber optic cables in the experiments. Strains were computed along this line to compare with Sneddon's solution and experimentally measured strains.

To validate the finite element model, a 200-inch block with a 1-inch radius crack was also simulated to compare with Sneddon's model (Figure 2.4). The modeled strains agree perfectly with Sneddon's analytic solution. The 1-inch crack is small enough relative to the size of the 200-inch cube that the modeled strain matches Sneddon's infinite domain solution.

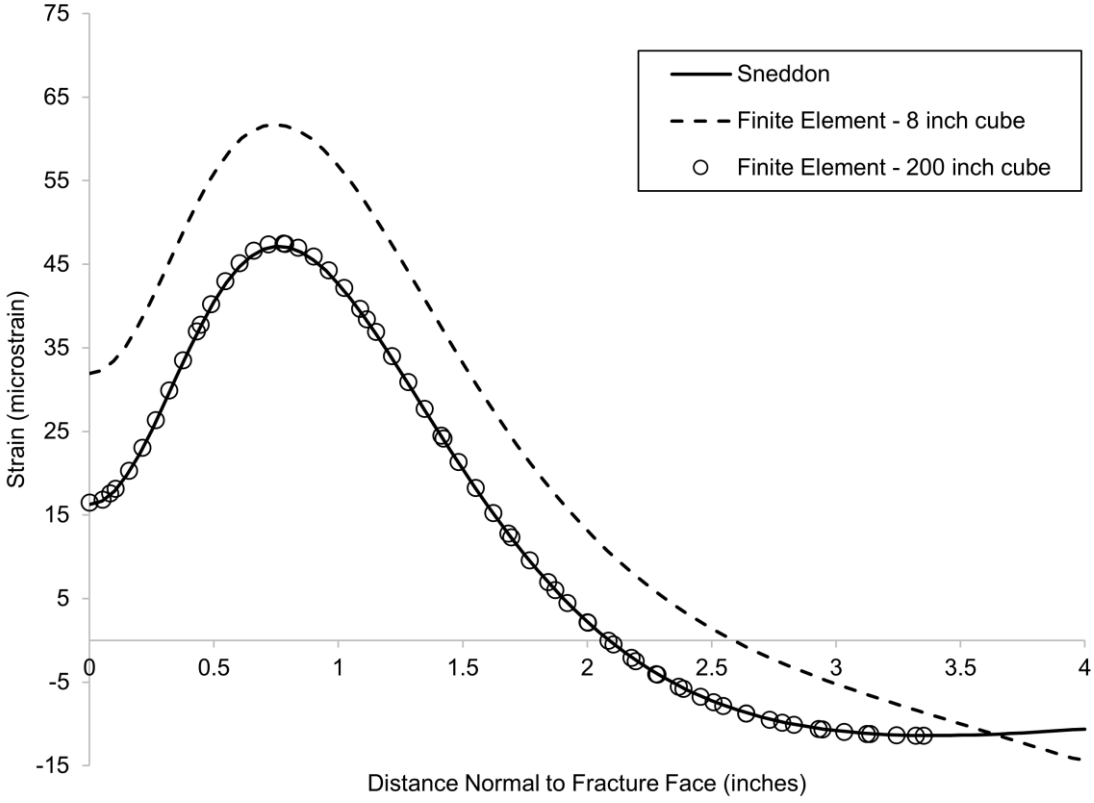

Figure 2.4 Finite element model validated with Sneddon's solution.

Sneddon's solution and the finite element model incorporate the same physics (linear elastic behavior), but with different boundary conditions. Therefore, the finite element model serves as a link between interpreting experimental results at the lab scale and Sneddon's solution for an infinite medium. Figure 2.5 illustrates the relationships between the experiment and the models schematically.

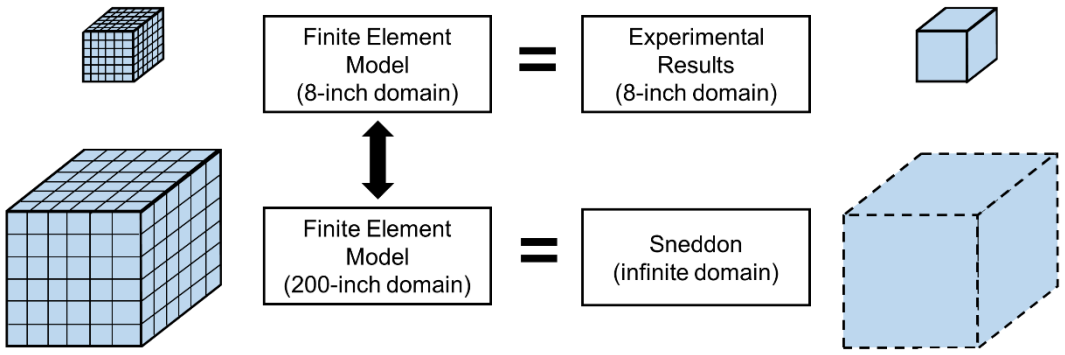

Figure 2.5 Illustration of the relationships between the various modeled domains and the experiment.

2.1.3. Displacement Discontinuity Method

It is of interest to numerically evaluate thermal effects on the LF-DAS response in unconventional completions as presented in Chapter 6. To do so requires comparing the magnitude of the thermal (temperature) and mechanical (strain) components of the LF-DAS optical phase shift for a modern hydraulic fracture completion. Simulating the strains induced by a modern, multi-cluster fracture stage necessitates a geomechanical model that can efficiently simulate multiple fractures. The displacement discontinuity method (DDM) is well suited to approximate the strains due to fractures with complex shapes in an infinite medium.

DDM involves discretizing fractures into a grid of boundary elements. Each boundary element represents a portion of the fracture modeled as a dislocated element with a

constant fracture width, *w*. The following schematic illustrates a fracture subdivided into boundary elements of length and height 2a and 2b respectively (Wu, 2014). The uppercase *X*, *Y*, and *Z* represent the global coordinates, while the lowercase x_1, x_2, and x_3 correspond to local coordinates relative to the center of a boundary element. In this research, a fiber optic cable with axis normal to a set of multiple, planar fractures is considered. For fracture element *j* with its center located at X_j, Y_j, and Z_j, and a point of interest *i* with a center location of X_i, Y_i, and Z_i, the relative coordinates are computed by:

$$x_1 = X_i - X_j \tag{2.60}$$

$$x_2 = Y_i - Y_j \tag{2.61}$$

$$x_3 = Z_i - Z_j \tag{2.62}$$

It is possible to use DDM to compute displacements due to non-parallel and non-planar fractures, or a fiber installed with an axial direction non-normal to the fracture. These considerations would require different coordinate transformations than presented in Equations 2.60 to 2.62. The appropriate coordinate transformations can be found in (Wu 2014).

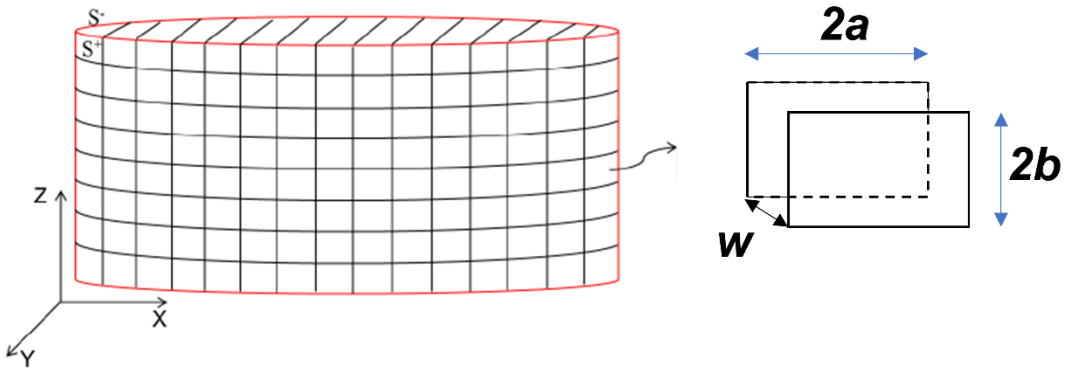

Figure 2.6 Schematic of a discretized fracture in the displacement discontinuity method (modified Wu, 2014).

Considering planar fractures, the following relationship from DDM relates the displacement at any location in an infinite, linear-elastic, homogeneous medium to the fracture geometry (Shou, 1993).

$$\boldsymbol{u_n} = \boldsymbol{B} \cdot \mathbf{w} \qquad 2.63$$

The vector $\boldsymbol{u_n}$ represents the displacements normal to the plane of the fracture at points of interest in the fracture medium. The points of interest can be selected to represent the location of the fiber optic cable relative to the treatment well. Neglecting strain transfer effects from the fracture medium to the fiber, the displacements in Equation 2.63

approximate the displacements experienced by the fiber optic cable. The vector $\boldsymbol{w}$ represents a list of fracture widths for each element of the discretized fracture. In this work, a commercially available fracture simulator (GOHFER) was used to simulate fracture geometries and widths for an unconventional completion (Halliburton 2018). The widths were exported at each time step to populate the width vector $\boldsymbol{w}$.

The matrix $\boldsymbol{B}$ contains DDM influence coefficients. For a planar fracture with purely normal dislocations (no shear movement), the influence coefficient of boundary element *j* on an arbitrary location *i* in an infinite linear-elastic medium is determined by the following set of equations (Shou, 1993).

$$\boldsymbol{B}(i,j) = \frac{1}{8\pi(1-\nu)}[2(1-\nu)I_3(i,j) - x_3(i,j)I_{33}(i,j)] \tag{2.64}$$

$$I_3 = -\tan^{-1}\left(\frac{(x_1-\xi_1)(x_2-\xi_2)}{rx_3}\right)\Bigg\| \tag{2.65}$$

$$I_{33} = \frac{(x_1-\xi_1)(x_2-\xi_2)(x_3^2+r^2)}{r(x_3^2+(x_1-\xi_1)^2(x_3^2+(x_2-\xi_2)^2))}\Bigg\| \tag{2.66}$$

$$r = \sqrt{(x_1-\xi_1)^2+(x_2-\xi_2)^2+x_3^2} \tag{2.67}$$

Here, ν is Poisson's ratio, and I_3 and I_{33} are integral equations computed based on the relative locations of the fracture element *j* and point of interest *i*. The relative locations x_1, x_2, and x_3 are given in Equations 2.60 to 2.62. The double bar represents Chinnery's notation, where the integral equations are evaluated as:

$$I_3(\xi_1,\xi_2)\| = I_3(a,b) - I_3(a,-b) - I_3(-a,b) + I_3(-a,-b) \tag{2.68}$$

ξ_1 and ξ_2 are temporary variables of integration that are substituted by *a* and *b*, the half-length and half-height of a fracture element (as shown in Figure 2.6). In Equation 2.67, *r* is a parameter representing a spherical radius used in computing I_3 and I_{33}. After computing the vector $\boldsymbol{u_n}$, consisting of a list of displacements at prescribed points of interest, the strain at any location, ε_z, can be computed by numerical differentiation using the central difference method:

$$\varepsilon_z = \frac{u_n(i+1) - u_n(i-1)}{Z(i+1) - Z(i-1)} \qquad 2.69$$

The implementation of the displacement discontinuity method was validated against Sneddon's analytic solution. A radial fracture was discretized into boundary elements. Figure 2.7 compares the computed displacement along the locations of a fiber optic cable using DDM versus the displacement computed by Equation 2.46. Similarly, Figure 2.8 compares the computed strain using DDM and Equation 2.50. The results validate the implementation of the displacement continuity method programmed for this work.

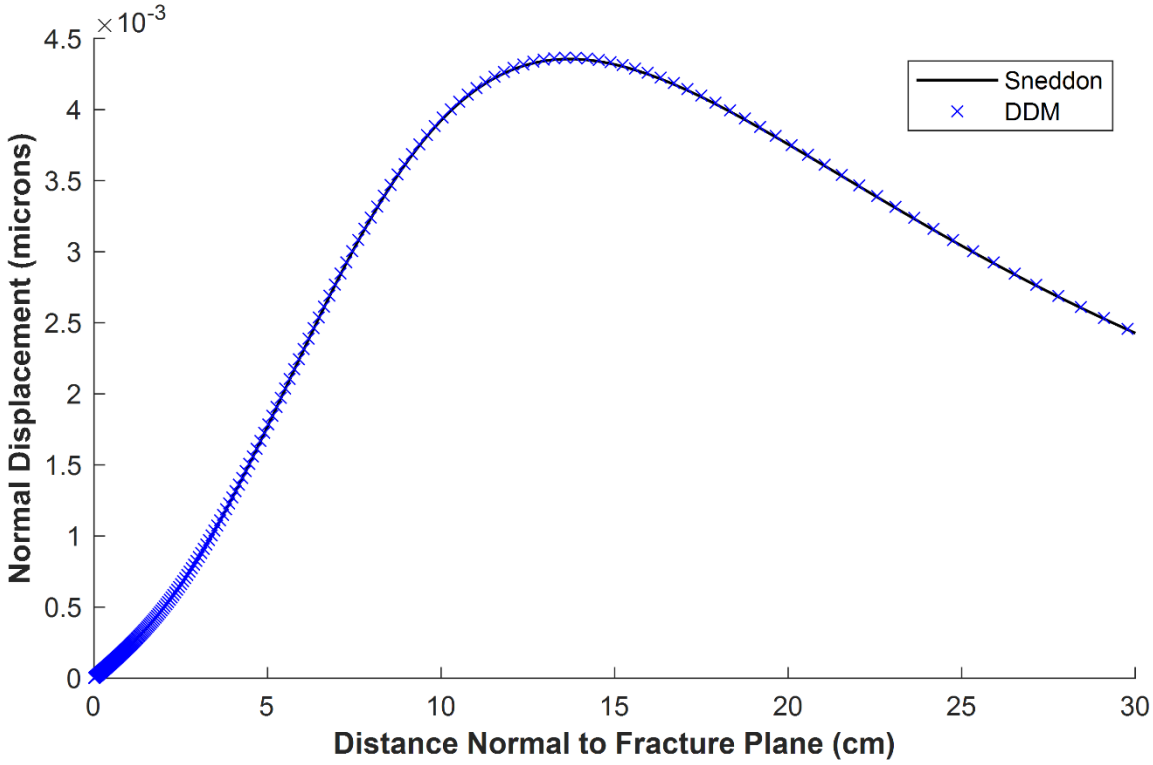

Figure 2.7 Validation of DDM displacement calculations against Sneddon's analytical solution.

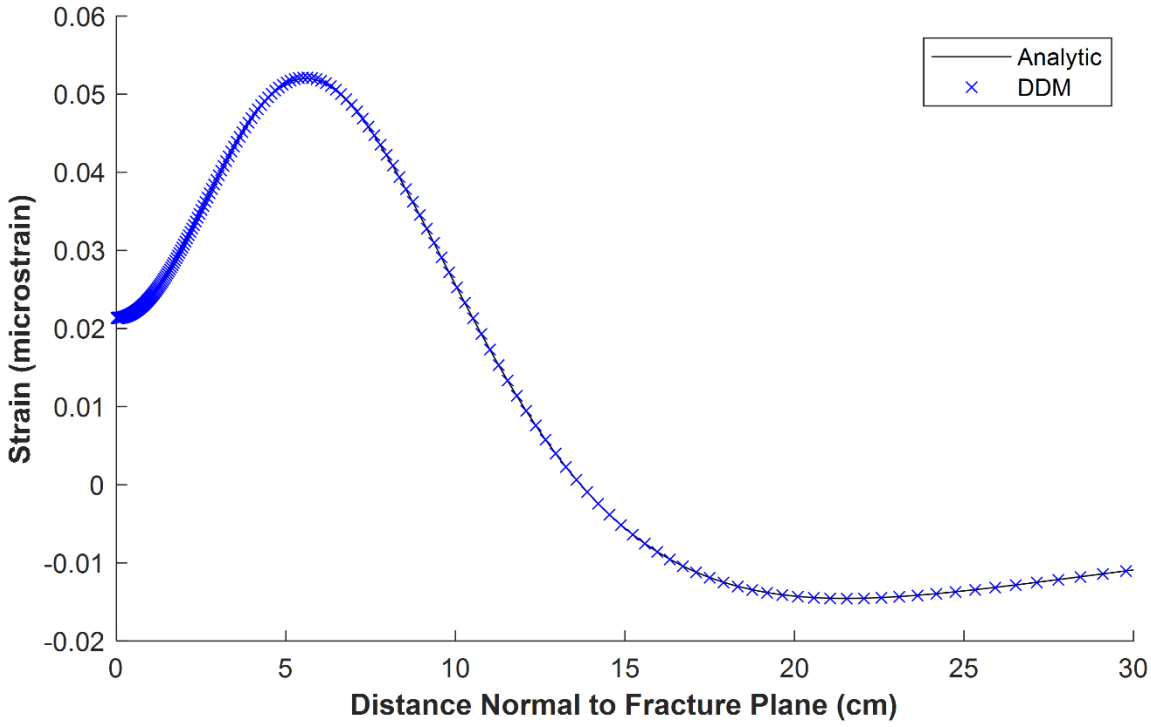

Figure 2.8 Validation of DDM strain calculations against Sneddon's analytical solution.

Each of the linear elastic models helps interpret strains measured by fiber optic cables in the field and the lab experiments. In the following section, the optical sensors used in the lab experiments are introduced and explained in detail.

2.2. Fiber Bragg Grating Strain Sensors

The spatial resolution of LF-DAS is on the order of meters. This is much too coarse to measure strains in the 8-inch experimental blocks. Fiber Bragg grating (FBG) sensors

address the concerns of the spatial resolution while satisfying the sampling rate and strain sensitivity requirements for the experiments (Krohn et al. 2015). The following sections provide the necessary background theory required to understand the FBG response in the lab experiments.

2.2.1. Fiber Bragg Grating Working Principle

In DAS, random inhomogeneities in the fiber optic cable's core act as reflectors. When a laser beam is pulsed through the fiber, these random reflectors cause backscattering events that serve as the basis for the DAS signal. Similarly, FBG strain sensing also relies on reflections of a pulsed laser. However, the reflectors are not random inhomogeneities but rather are laser-inscribed modulations to the index of refraction of the fiber's core. The portions of the fiber that have modulations in the index of refraction are called Bragg gratings. Figure 2.9 illustrates a fiber containing a Bragg grating with a uniform grating period, Λ, and grating length, L_{FBG}. Bragg gratings are typically 1 to 20 millimeters long. The modulation of the index of refraction, n, has a magnitude on the order of 10^{-3} to 10^{-5} (Krohn et al. 2015).

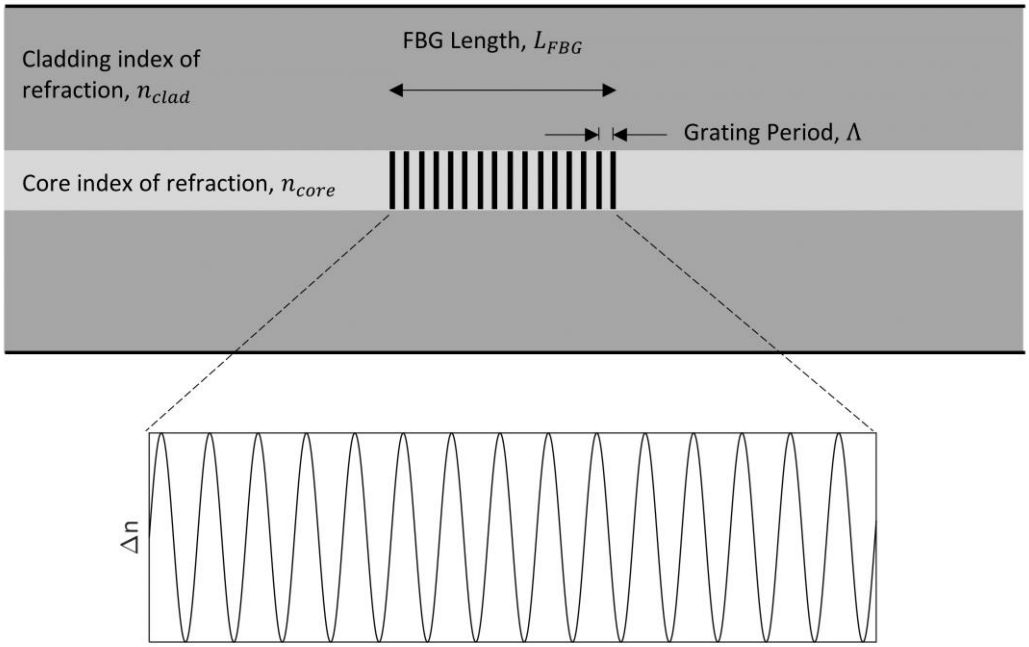

Figure 2.9 Schematic of a portion of a fiber optic cable with an inscribed fiber Bragg grating with a uniform grating period.

When a laser pulse travels through a fiber Bragg grating, a portion of the light is reflected. The strongest reflection occurs when the wavelength of the laser pulse is equal to the Bragg wavelength. The Bragg wavelength, λ_B, is the wavelength at which resonance occurs with the grating period, Λ. For a single-mode fiber, Equations 2.70 and 2.71 describe the Bragg wavelength as a function of the grating period (Krohn et al. 2015).

$$\lambda_B = 2n_{eff}\Lambda \qquad 2.70$$

$$n_{eff} = n_{clad} + 0.6(n_{core} - n_{clad}) \quad 2.71$$

The effective index of refraction, n_{eff}, depends on the indices of refraction of the core and cladding, respectively. For an effective index of refraction of 1.45, a grating period of 500 nanometers corresponds to a Bragg wavelength of 1450 nanometers.

2.2.2. FBG Strain Sensing

Equation 2.70 demonstrates that the fiber Bragg wavelength is proportionally related to the grating period. If the fiber experiences an axial extension or compression, the grating period will increase or decrease respectively, altering the Bragg wavelength. Thus, by interrogating the fiber to monitor the Bragg wavelength, FBGs become highly sensitive strain sensors. Figure 2.10 illustrates the shift in the Bragg wavelength due compressive or tensile strains.

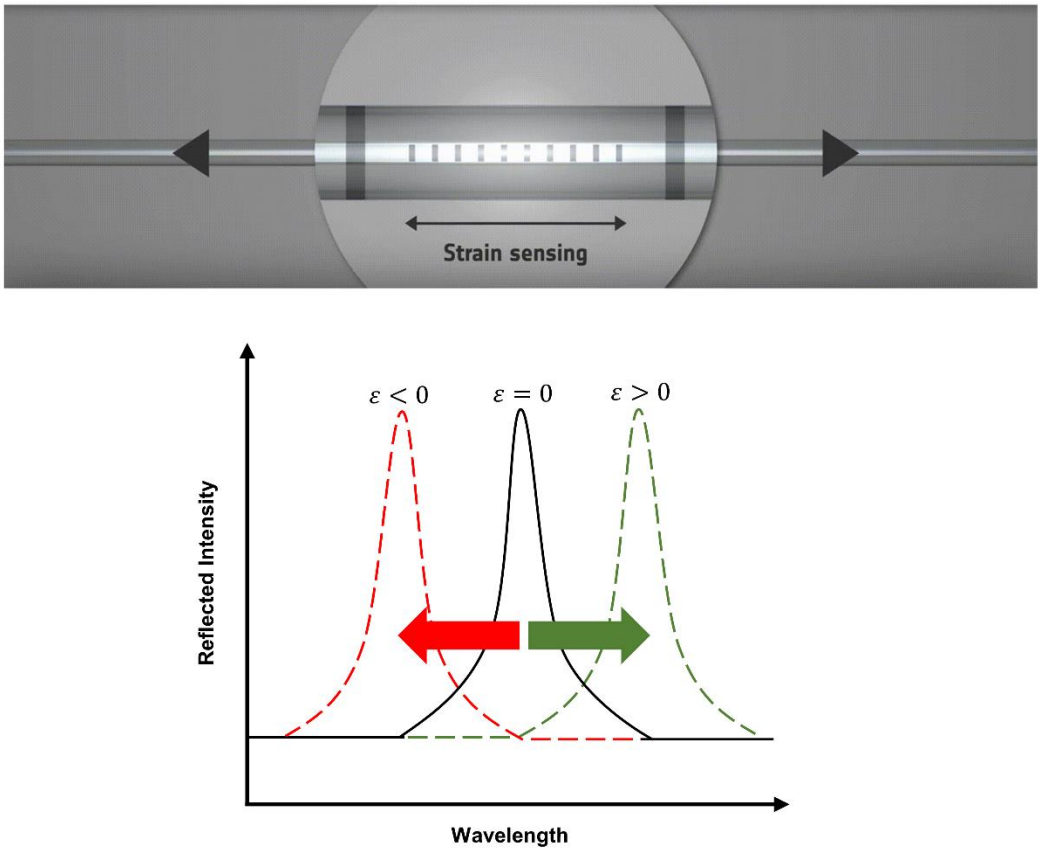

Figure 2.10 Schematic of the working principle for fiber Bragg grating based strain sensing. Adapted from FBGS, 2021.

Temperature changes can also cause the grating period to shift via thermal expansion and changes in the effective index of refraction (Kersey et al. 1997). Changes in the Bragg wavelength, λ_B, as a function of strain, ε, and temperature, T, for silica fibers are computed by (Krohn et al. 2015):

$$\Delta\lambda_B = \zeta_\varepsilon \lambda_B \varepsilon + \lambda_B \Delta T * 6.67x10^{-6} \quad 2.72$$

ζ_ε is the stress-optic coefficient for silica fibers. If temperature changes are negligible, then this equation can be reorganized to compute the strain as:

$$\varepsilon = \frac{1}{\zeta_\varepsilon} \frac{\Delta\lambda_B}{\lambda_B} \quad 2.73$$

The manufacturer suggested using 0.772 as the stress-optic coefficient for the specific FBG strain sensors used in this study.

Multiple FBGs with different grating periods can be inscribed on a single fiber optic cable (Figure 2.11). Doing so creates an array of axial strain sensors along the fiber. When a laser pulse is emitted down a fiber with an array of FBG sensors, the backscattered spectrum contains multiple peaks. The gratings on the FBG array should be designed with adequate spectral spacing between Bragg wavelength reflection peaks, typically at least 1-nanometer or greater difference. That way, the backscattered peaks will not overlap.

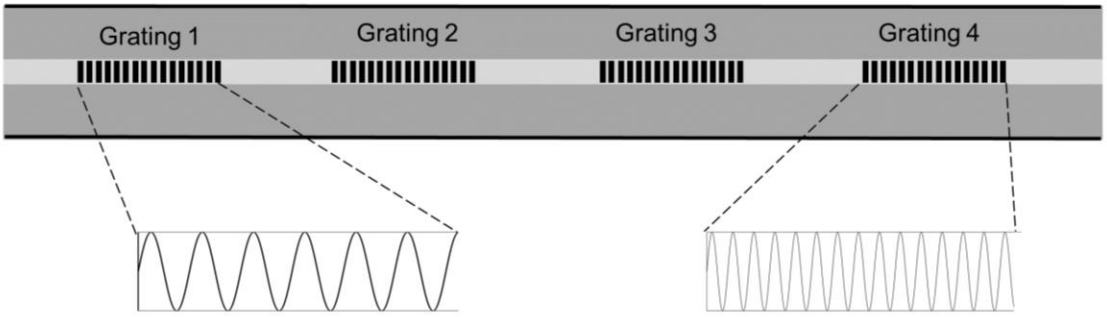

Figure 2.11 Schematic of a fiber with an array of FBG sensors. The difference in the grating period (and therefore, the Bragg grating) between Gratings 1 and Gratings 4 is exaggerated for illustration purposes.

2.2.3. Peak Detection in FBG Sensing

Using FBGs as strain sensors requires accurately tracking the Bragg wavelength as the fiber deforms. There are two primary methods for detecting the Bragg wavelength (Krohn et al. 2015). The method used by the optical interrogator in this study involves a tunable laser. The tunable laser rapidly fires pulses at incremental wavelengths to construct a spectrum as shown in Figure 2.12. A smaller wavelength increment, $\delta\lambda$ improves the ability to capture the FBG spectrum. The leftmost image of Figure 2.12 displays an acceptable spectral resolution, while the center and rightmost images exhibit non-ideal resolutions.

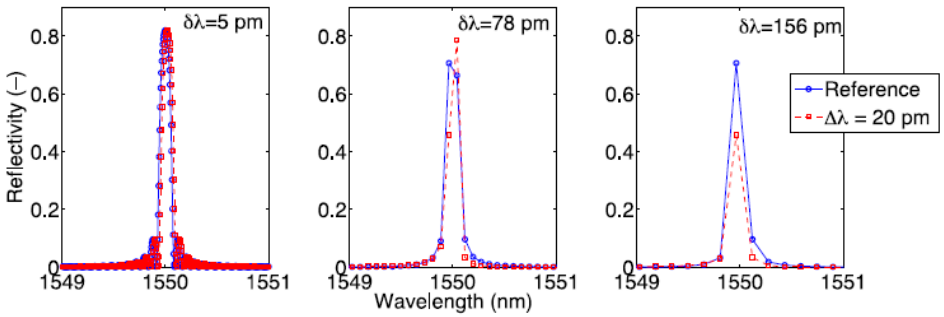

Figure 2.12 An illustration of peak detection with decreasing spectral resolution from left to right (Tosi 2017).

After obtaining the reflected intensity at incremental wavelengths, the Bragg wavelength can be computed using one of the following methods:

1. Maximum method – As mentioned, the tunable laser emits pulses at incremental wavelengths (λ_1, λ_2, … λ_n). In the maximum method, the Bragg wavelength is estimated as the wavelength λ_i at which the strongest reflection occurs. This is the least accurate method, because the resolution in determining the Bragg wavelength is limited to $\delta\lambda$, the wavelength increment of the tunable laser.
2. Centroid method – The Bragg wavelength is computed by the wavelength-weighted centroid of the spectrum., as shown in Equation 2.74. Here, I is the measured intensity of the reflected laser pulse. This results in a more accurate determination of the Bragg wavelength than the maximum method. One drawback is that this method requires specifying the wavelength range over

which the centroid is computed. This is typically accomplished by creating windows around the observed spectral peaks and defining a noise threshold. Below the noise threshold, reflected intensities are ignored in the centroid computation.

$$\lambda_B = \frac{\sum_{i=1}^{n} \lambda_i * I(\lambda_i)}{\sum_{i=1}^{n} I(\lambda_i)} \quad 2.74$$

3. Quadratic fit method – In this method, a parabolic fit is performed to a select number of data points from the reflected spectrum (Equation 2.75). The location of the peak of the parabola occurs when the derivative is zero (Equation 2.76). The Bragg wavelength can thus be computed from Equation 2.77, where *a* and *b* are the first two coefficients of the parabolic fit. This method is comparable in accuracy to the centroid method. In this work, the five data points with the strongest reflections were used for the parabolic curve fit.

$$I(\lambda) = a\lambda^2 + b\lambda + c \quad 2.75$$

$$\frac{dI}{d\lambda} = 2a\lambda + b = 0 \quad 2.76$$

$$\lambda_B = \frac{-b}{2a} \quad 2.77$$

This list of peak location determination methods is not exhaustive; a comprehensive review of FBG peak tracking methods can be found in the literature (Tosi 2017). The quadratic method was used in this study for "nice" peaks (peaks that could be approximated as parabolic in shape), while the centroid method was employed when

the shape of the peak had degraded such that a parabola did not describe the shape of the spectrum well.

3. EXPERIMENTAL METHODS

3.1. Overview of the Experiments

This chapter details the designs, procedures, and quantifications of measurement uncertainty for a laboratory-scale hydraulic fracture experiment. In the experimental study, we simulate the LF-DAS response to fracturing in horizontal wells using an 8-inch, transparent, epoxy cube. Two fiber optic cables were embedded in the cube at defined locations to record strain responses during fracture propagation. The objectives of the experiments are:

1. To validate interpretations of LF-DAS strain rate waterfall plots that indicate when and where a fracture intersects the fiber optic cable.
2. To study the relationship between the LF-DAS strain rate response and changes in fracture pressure and geometry.
3. To develop methods to estimate the distance from the fracture front to the fiber optic cable from the LF-DAS data.

A schematic representation of the experiment is depicted in Figure 3.1. A syringe pump injects dyed water into the center of the epoxy fracture specimen to propagate a fracture along an initial flaw. No confining stresses are applied. A pressure transducer records the injection pressure downstream of the pump. Arrays of fiber Bragg grating strain sensors measure the strain along lines offset and parallel to the injection tubing. This setup mimics a field condition with a treatment well (injection tubing in the experiment) and an observation well with fiber optic sensors installed along it (the fiber cable in the

experiment). A digital camera records the fracture propagation for geometry measurements.

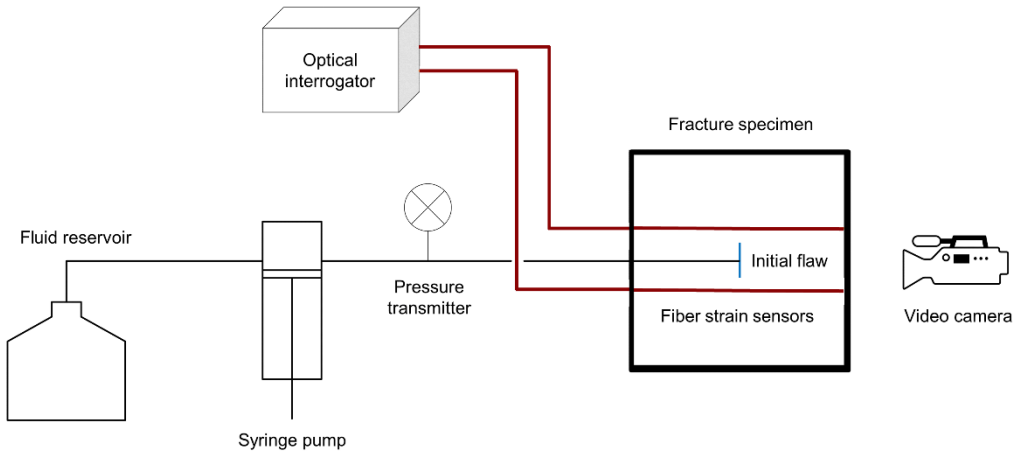

Figure 3.1 Schematic representation of the lab-scale hydraulic fracture experiment.

The fracture specimens were fashioned in a mold created with 3/4-inch plywood lined with polypropylene sheathing tape. The EcoPoxy Flowcast resin and hardener system was utilized to create the 8-inch cubic samples. The mechanical properties of the cured epoxy depend on the curing time and temperature. As such, the room temperature was maintained at 72 ºF. Epoxy cures in an exothermic reaction. The manufacturer

recommended pouring layers of epoxy no more than 1.5 inches thick to minimize heterogeneity and maintain transparency in each layer. For consistency, the 8-inch specimens were created over 6 pours, each 1.333 inches thick. Each layer cured for three days before the next layer was poured so that the heat generated during one layer's cure would not affect subsequent layers. The fracture test was conducted a week after the final epoxy layer was poured.

An initial flaw was placed in the center of the block at the top of layer three. The flaw consists of a circular piece of polypropylene sheathing tape of 1-inch radius. After pouring layer four, a 1/2-inch diameter and 1 1/2-inch deep hole was drilled through the center of the initial flaw. A 1/4-inch stainless steel injection tubing was then inserted open ended into the hole. To preserve connectivity between the open end of the tubing and the initial flaw, an O-ring was placed around the injection tubing one-tenth of an inch above the fracture layer. Figure 3.2 illustrates the main components of the fracture specimen. Figure 3.3 provides a detailed schematic exhibiting the epoxy layers, fiber optic cables, and injection tubing. A detailed procedure with step-by-step instructions to create a fracture specimen is provided in Section 3.6.

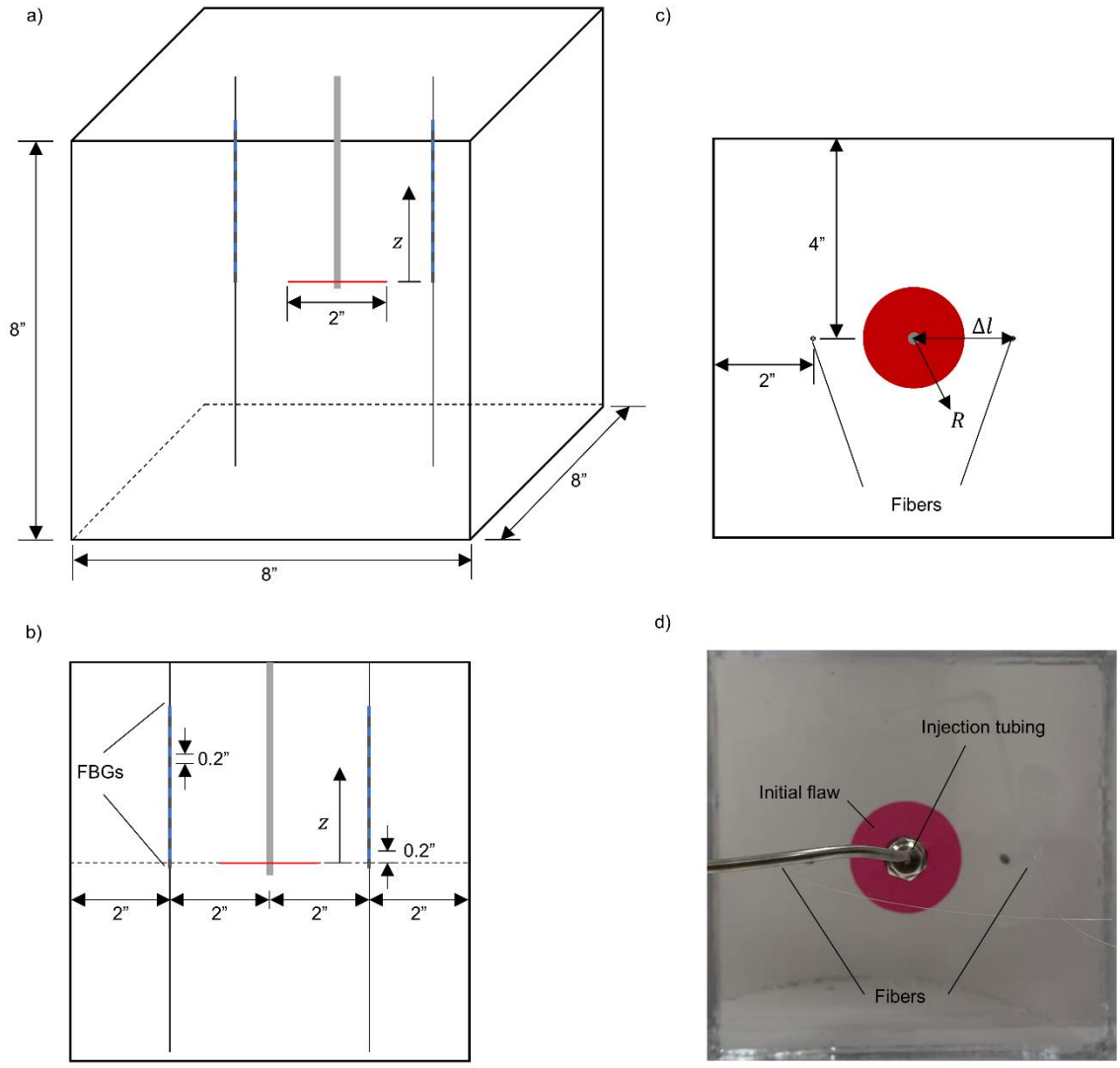

Figure 3.2 Schematic representation of the epoxy fracture specimens in a) an isometric view, b) a view normal to the fracture plane, c) a view parallel to the axis of the injection tubing and fiber optic cables and d) an image from a representative experiment.

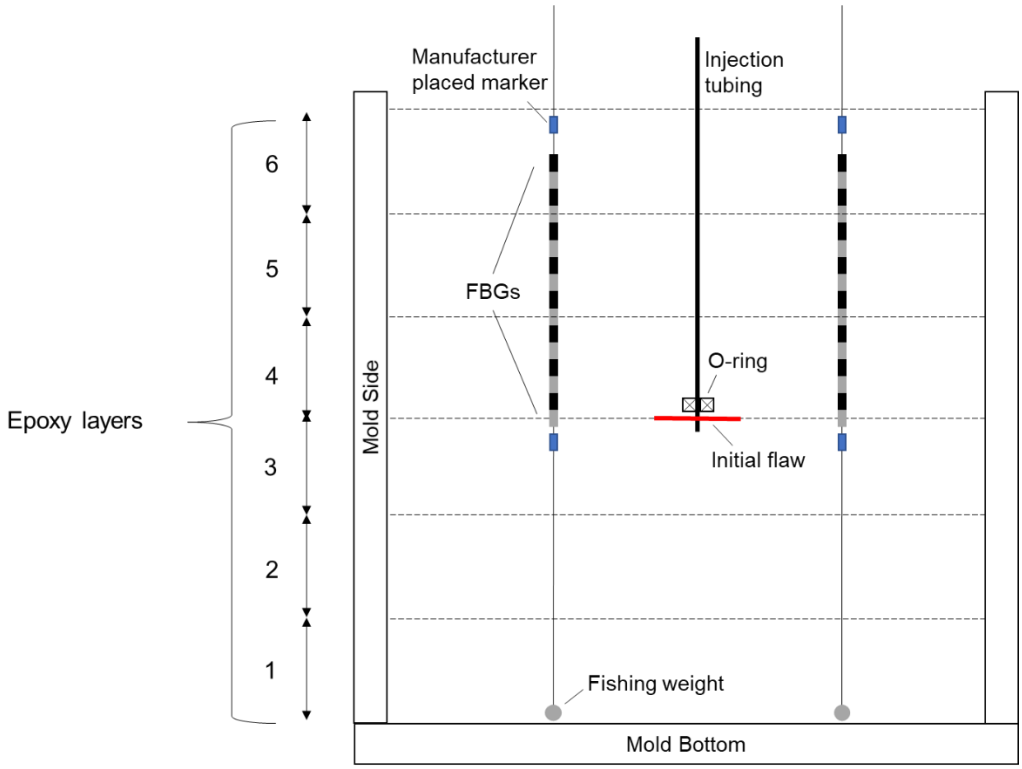

Figure 3.3 Schematic of the fracture specimen with embedded injection tubing, initial flaw, and fiber Bragg grating (FBG) strain sensors. The black and gray rectangles depicting the FBGs correspond to two separate fiber arrays that are embedded together to increase the spatial resolution of the strain sensors.

The following sections detail the design, calibration, and uncertainty of each of the various sensors used in the experiment.

3.2. Pressure Measurements

Pressure measurements were obtained from the pressure transducer within the Teledyne Isco D-Series syringe pump. The calibration of the transducer was validated against separate pressure transducers with known calibrations. Experiments were conducted at

injection rates of 0.25 mL/min, resulting in negligible pressure drops within the injection tubing and fracture. Assuming no barriers to flow exist between the open end of the injection tubing and the initial flaw, the pressure measurements represent the pressure in the fracture. The observed variability in the pressure measurements was the greater of +/- 3 psi or +/- 1% of the measured pressure.

3.3. Fracture Geometry Measurements

A digital camera was utilized to record fracture propagation at a frame rate of 30 frames/second with a spatial resolution of approximately 100 pixels/inch on the fracture plane. The digital camera and face of the epoxy block were carefully aligned with each other to avoid angular distortions of the geometry measurements. The ratio of pixels to inches was calibrated for each experiment against the known dimensions of the initial flaw. An eccentric radial fracture emanated from the initial flaw during each experiment. The fracture radius and center were computed based on an equivalent area from photogrammetry measurements. The measurements are reliable at approximately the resolution of one pixel, or one one-hundredth of an inch. Figure 3.4 illustrates the measurement of the distance from the fiber to the fracture tip. The distance was computed along a line from the fiber axis to the edge of the fracture nearest to the fiber.

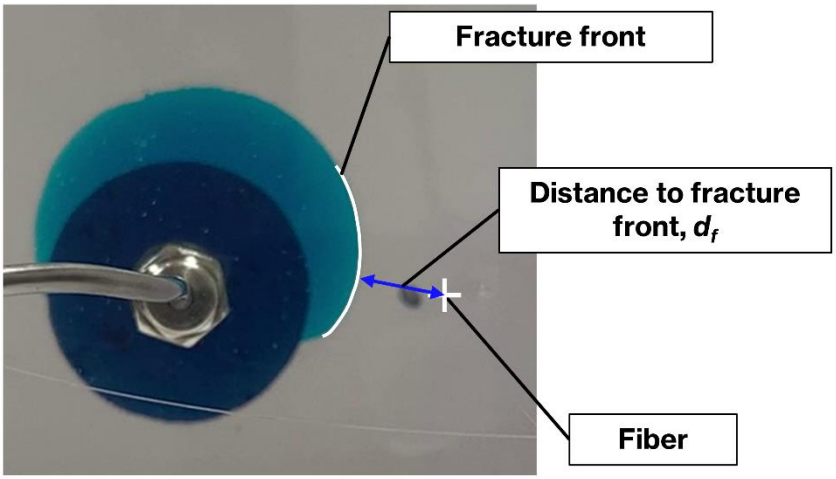

Figure 3.4 Example image of an eccentric, radial fracture observed in the experiments.

3.4. Strain Measurements

The theory of fiber Bragg grating (FBG) strain sensors was discussed in Section 2.2. The strain is measured based on a change in the Bragg wavelength, $\Delta\lambda_B = \lambda_B - \lambda_{B0}$.

$$\varepsilon = \frac{1}{\zeta_\varepsilon}\frac{\lambda_B - \lambda_{B0}}{\lambda_{B0}} \tag{3.1}$$

A SmartScope FBG interrogation unit was used to record the reflected spectrum with a tunable laser scanning a wavelength range from 1525 to 1565 nanometer at 20-picometer intervals. An example of the reflected spectrum of a fiber with an array of eight FBG sensors is shown below.

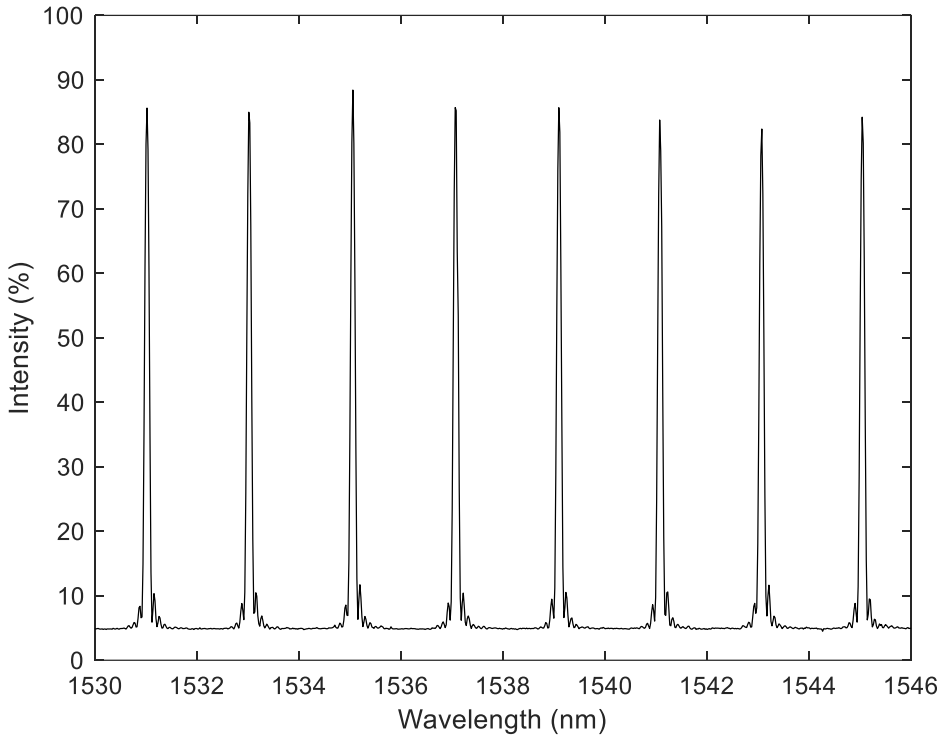

Figure 3.5 Example reflected spectrum of an array of 8 FBG sensors.

In this work, both the centroid and quadratic methods were applied to compute the Bragg wavelength, as discussed in Section 2.2.3. When using the centroid method to compute the Bragg wavelengths associated with an array of FBG sensors, the following steps were applied:

1. Window the spectrum to focus on a single FBG.
2. Exclude the portions of the signal at or near the noise threshold. (Approximately 7% in Figure 3.5).
3. Compute the Bragg wavelength via Equation 2.74.

The following subsections detail FBG sensor design, a procedure to obtain the strain data from a SmartScope interrogation unit, and the calibration and uncertainty of the strain measurements.

3.4.1. FBG Strain Sensor Design

The following provides guidance for designing and selecting FBG sensors for strain measurements in the fracture experiments. The suggested specifications assume a SmartScope interrogation unit with a spectral range of 1528 to 1568 nanometers, 4 optical channels for FBG arrays with a maximum of 16 FBGs per channel, 5 Hz sampling rate, and FC/APC connection ports. Table 3.1 provides suggested specifications for FBG design variables for the fracture experiments. These design variables must be specified to the FBG manufacturer when ordering the fiber optic sensors. The FBG sensing arrays in the experiments presented in this work were sourced from the company FBGS. A fiber lead-in of 1 to 3 feet is recommended based on experience. A lead-in of less than 1 foot does not provide sufficient length to connect the fibers protruding from the block to the interrogator. A lead-in of greater than 3 feet causes difficulty when suspending the fibers in the mold during the epoxy curing process.

Table 3.1. FBG sensor specifications.

FBG Design Variable	Suggested Specification	Notes
Coating	Ormocer	Ormocer-T coating has also been used successfully.
Minimum Bragg wavelength	1538 nm	The Bragg wavelength shifts lower due to volumetric shrinkage of epoxy.
Spectral distance between Bragg wavelengths	2 nm	For example, Bragg wavelengths of 1538, 1540, 1542… nm.
Grating length	2 – 5 mm	A smaller length degrades the signal to noise ratio but improves spatial resolution.
Fiber lead-in	1 – 3 feet	This is the amount of fiber between the connector and the first FBG.

3.4.2. Procedure to Obtain Strain Data from SmartSoft Program

The following procedure describes how to use the SmartSoft program for FBG strain sensing (2021). Separate instructions are provided for obtaining FBG measurements for the strain calibration procedure and the experiments. It is important to follow recommended safety practices when working with fiber optic cables. Safe practices include never looking at the end of a fiber optic cable that is plugged in to the laser interrogator or looking into a port on the interrogator. Doing so could cause serious eye damage. The fiber optic connections should be regularly cleaned with a Fiber Cleaning Tool for FC connectors. If the fiber has been cut, hands should be washed thoroughly to avoid accidental ingestion of fiber particles. Ingesting fiber particles can lead to damage of internal organs. This is not an exhaustive list of safe fiber handling practices.

1. Open SmartSoft v4.2.4.

2. Click the “Instrument Set Up” button.
3. Click the “Acquisition Rate” tab. Adjust the number of optical channels used to equal the number of fibers, up to 4. Do not adjust the cycle time, acquisition rate, or data rate. It is recommended to set the sample size to 1 and to the switch to “Average”. The appropriate settings are displayed in Figure 3.6.

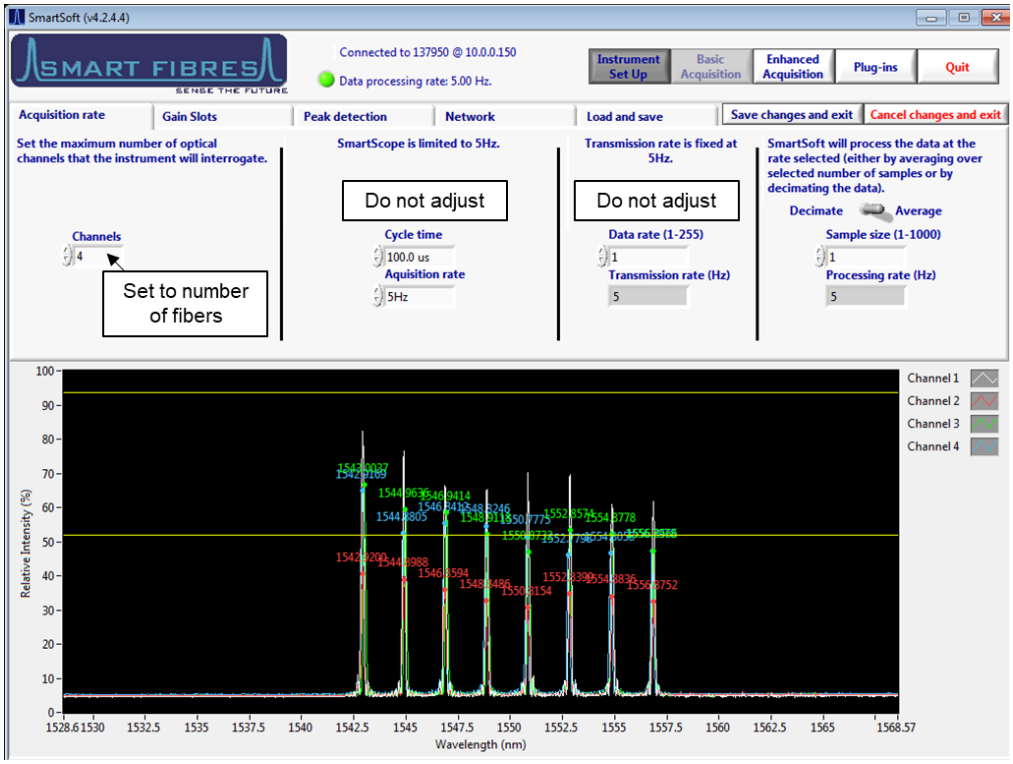

Figure 3.6 Sample screen for instrument setup in SmartSoft.

4. Click the “Gain Slots” tab. Do not adjust the AGC low or AGC high knobs. Right click on the black chart and adjust the gain to an integer such that the peaks fall within the 50-95% range.

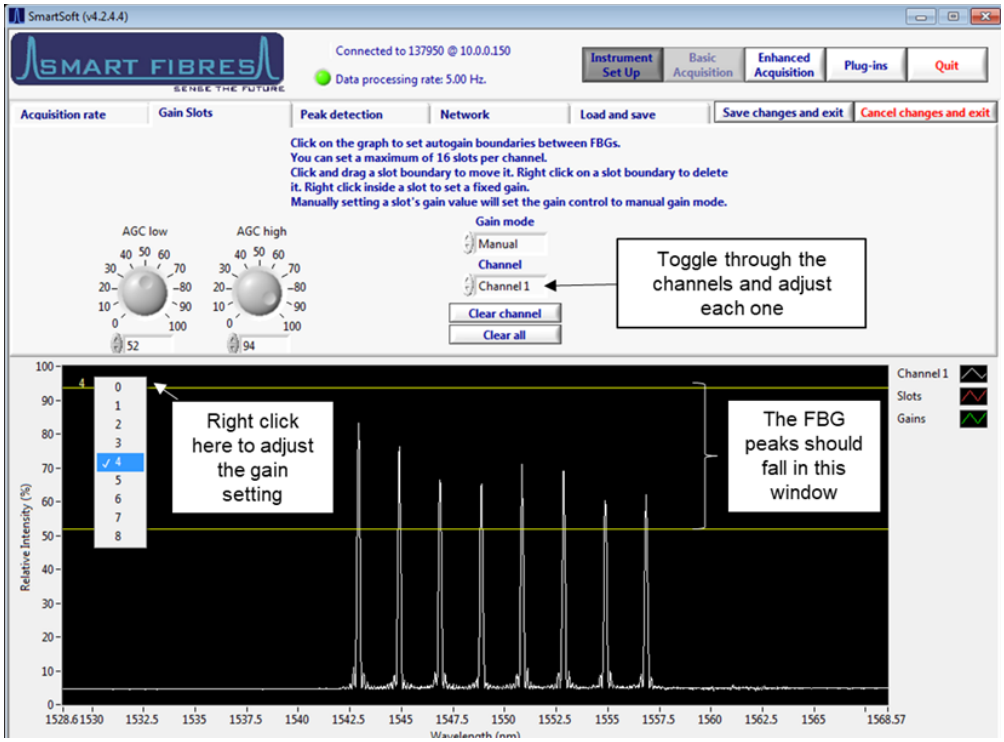

Figure 3.7 Sample screen for the gain slot settings in SmartSoft.

5. Click the “Peak Detection” tab. A peak detection threshold value of 15% is recommended but can be adjusted. This input represents the limit that a peak

must be above the noise floor for the peak detection algorithm to detect a peak. Do not adjust other parameters.

6. Click the “Enhanced Acquisition” button. Under the select sensors tab click the plus sign and name each FBG sensor detected.
7. For the strain calibration procedure:
    a. Click the “Spectrum” tab. Change the “Peak Detection” settings to “poly”. Under the “DSP function settings” tab, set the order to “2” and number of points to “5”. This uses a quadratic fit of 5 points around the peak to track the peak location according to Equation 2.77. Refer to Figure 3.8 for an image displaying the appropriate settings.
    b. Go back to the “Select sensors” tab. Specify the folder to which the FBG peak data will be saved. Set the Log time to “0” for the log to continue indefinitely. Press “Log”.
    c. Monitor the strain calibration procedure on the charts tab.

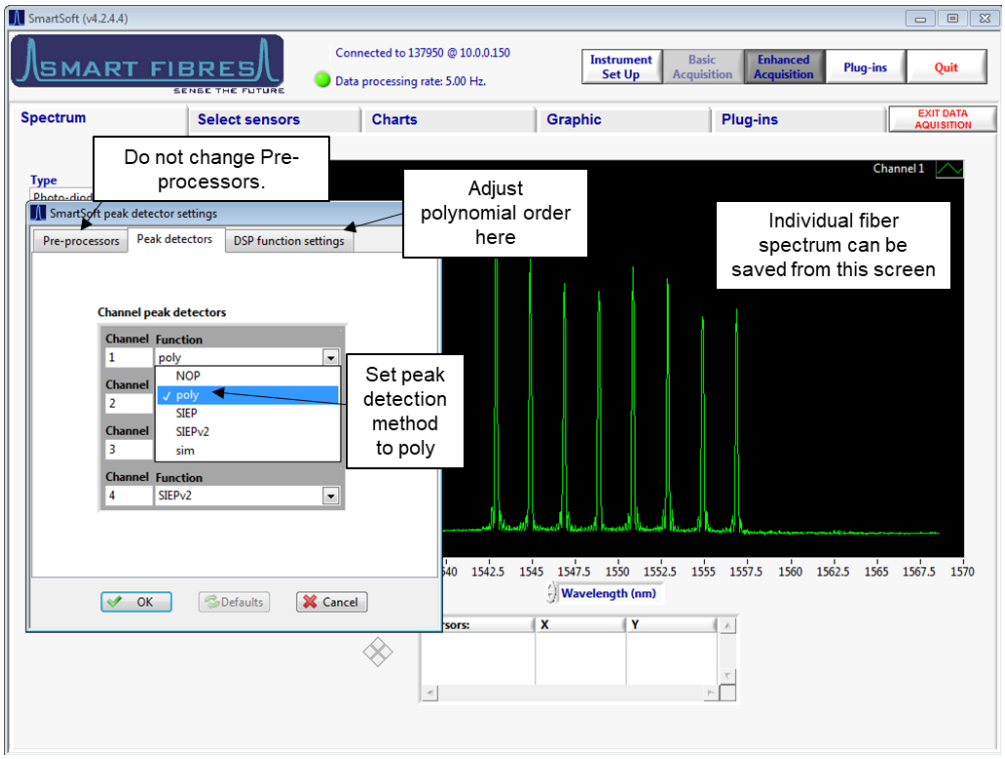

Figure 3.8 Peak detection settings in SmartSoft for the strain calibration procedure.

8. For the experiments, a different method is used to obtain the full spectrum from each of the four fiber optic cables. The procedure in step 7 relies on the SmartSoft programming to perform the peak detection and does not save the full spectrum. To obtain spectral data from each fiber for the experiments:
    a. Click the “Plug-ins” tab.
    b. Select the “Spectrum logger 4.1” plug-in.
    c. Specify the folder to which spectral data will be saved.

d. Press “Log” to start acquiring data. Refer to Figure 3.9 for an example of the plug-in screen with the spectral data of 4 fibers shown.

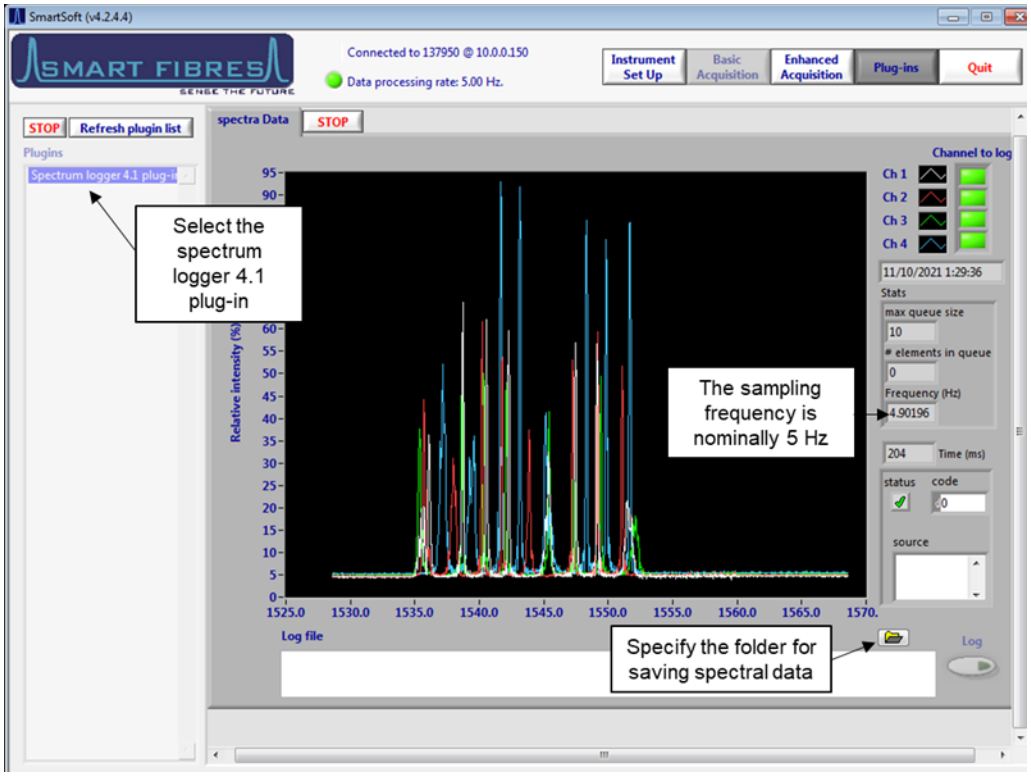

Figure 3.9 SmartSoft plug-in used for fiber spectral data acquisition.

3.4.3. Strain Calibration

The change in Bragg wavelength is measured according the procedure outlined in Section 3.4.2. This is then converted to strain by Equation 3.1. One method to validate the FBG strain measurements involves applying a known strain by suspending weights of known mass at the end of the fiber optic cables. A schematic representation of this setup is exhibited in Figure 3.10.

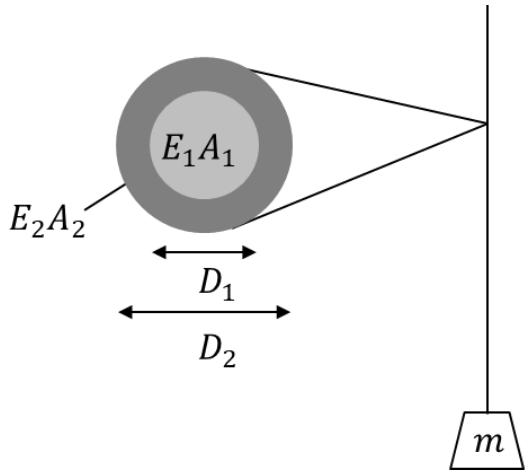

Figure 3.10 Schematic representation of the strain calibration procedure.

The relationship between the suspended mass and the applied strain can be derived considering a sum of forces on the fiber optic cable. In the following equations T_f is the tension on the fiber optic cable, m is the known mass, g is gravitational acceleration, σ is stress, E is the Young's modulus and A is cross-sectional area. The subscripts *1* and *2*

refer to the silica fiber optic cable and its protective Ormocer coating respectively, as depicted in Figure 3.10. According to the manufacturer, the Young's modulus is approximately 70 +/- 3.5 GPa for the silica fiber and 2 +/- 0.2 GPa for the Ormocer coating (FBGS 2021). The diameters of the fiber and coating are 125 and 195 microns respectively. A summation of forces yields:

$$\sum F = T_f - mg = 0 \tag{3.2}$$

$$T_f = \sigma_{eff}(A_1 + A_2) \tag{3.3}$$

$$\sigma_{eff}(A_1 + A_2) = \sigma_1 A_1 + \sigma_2 A_2 \tag{3.4}$$

$$T_f = \sigma_1 A_1 + \sigma_2 A_2 \tag{3.5}$$

Considering the uniaxial stress-strain relationship and that the strain of the core and cladding is the same:

$$\sigma = E\varepsilon \tag{3.6}$$

$$E_1 A_1 \varepsilon + E_2 A_2 \varepsilon = mg \tag{3.7}$$

$$\varepsilon = \frac{mg}{E_1 A_1 + E_2 A_2} \tag{3.8}$$

Equation 3.8 is used to compute the applied strain, ε, due to the suspended mass to compare with the strain measured by the FBG sensors. Figure 3.11 compares the applied and measured strains from a calibration experiment using weights with mass up to 14 grams. Using the manufacturer recommended value for the strain-optic

coefficient, ζ_ε=0.772, the applied and measured strains agree considering the uncertainty associated with the Young's modulus of the fiber and coating.

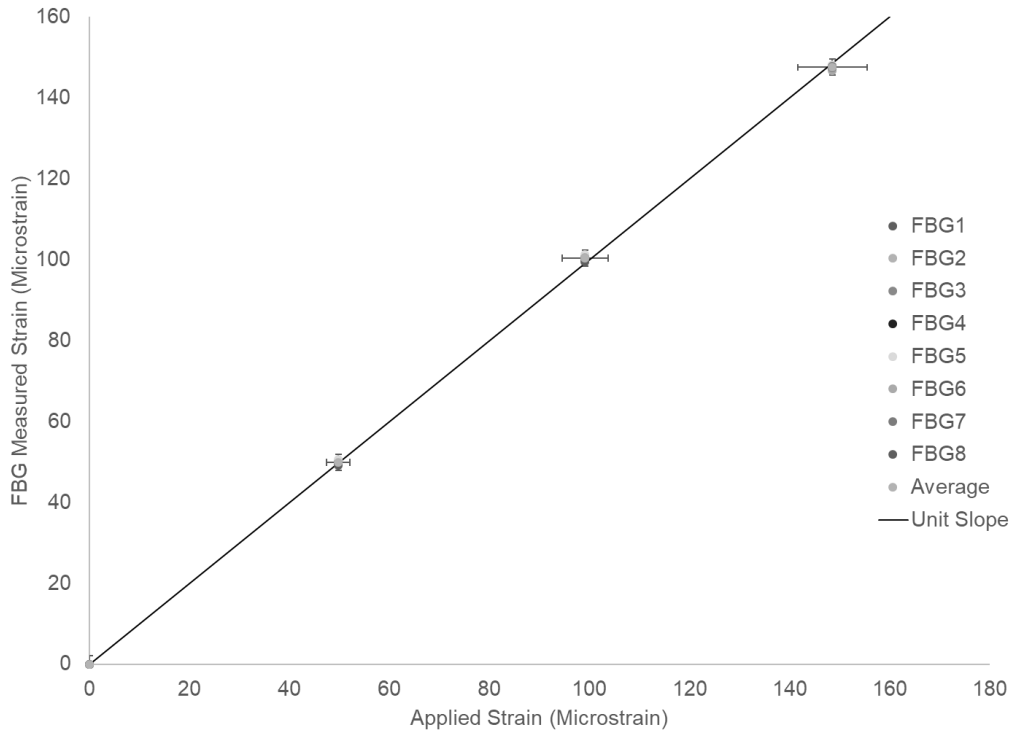

Figure 3.11 Comparison between applied and FBG measured strains with uncertainty markers and a unit slope for reference.

The following instructions provide a detailed procedure for performing the strain calibration.

1. Ensure the lab is maintained at 72 ºF, or the temperature at which the fracture experiments will be performed.
2. Acquire removable split shot fishing weights. Eagle Claw removable split shot size 2 fishing weights are recommended (Figure 3.12).

Figure 3.12 Removable split shot fishing weight used in the strain calibration procedure.

3. Measure and record the mass of three of the weights. Keep each weight in a separately labeled container to be able to know which mass corresponds to which weight.
4. Connect the fiber to be tested to the SmartScope unit. Gently rest the fiber on a smooth, round, edge of a table with no weights attached. Ensure that the way the fiber hangs does not cause the fiber to curve below the minimum bend radius of

the fiber recommended by the manufacturer. FBGS recommends a bend radius of greater than 6 millimeters for their draw tower gratings.

5. Acquire FBG Bragg wavelength data until a stable peak is observed (Section 3.4.2). This value will be used as the initial Bragg wavelength in Equation 3.1.
6. Use pliers or channel locks to crimp the weight to the bottom of the fiber, below all FBG sensors. Do not crimp a weight directly on a FBG sensor to avoid damaging the sensors.
7. Acquire FBG peak wavelength data until a stable peak is observed. Ensure the fiber is motionless and not swinging in a pendulum motion before proceeding.
8. Repeat steps 6 and 7 for the second and third fishing weights.
9. Remove the fishing weights.
10. Repeat steps 4 through 9 for all fibers to be tested.
11. Compute the applied strain on the fiber using Equation 3.8.
12. Compute the measured strains for the FBG sensors using Equation 3.1.
13. Plot the applied strains vs. measured strains for each fiber. Plot the unit slope line as in Figure 3.11 and ensure that the measured and applied strains agree within uncertainty. If they do not agree, ensure that the proper values are being used for the fiber and coating diameter and Young's Modulus. If needed, as a last resort, tune the strain-optic coefficient ζ_ε until agreement is reached.

3.4.4. Uncertainty in Strain Measurements

As a result of volumetric shrinkage during the epoxy cure, the shapes of the spectral peaks degrade to varying degrees as shown in Figure 3.13. The reflected spectrum of the FBG array prior to curing in the epoxy was exhibited in Figure 3.5.

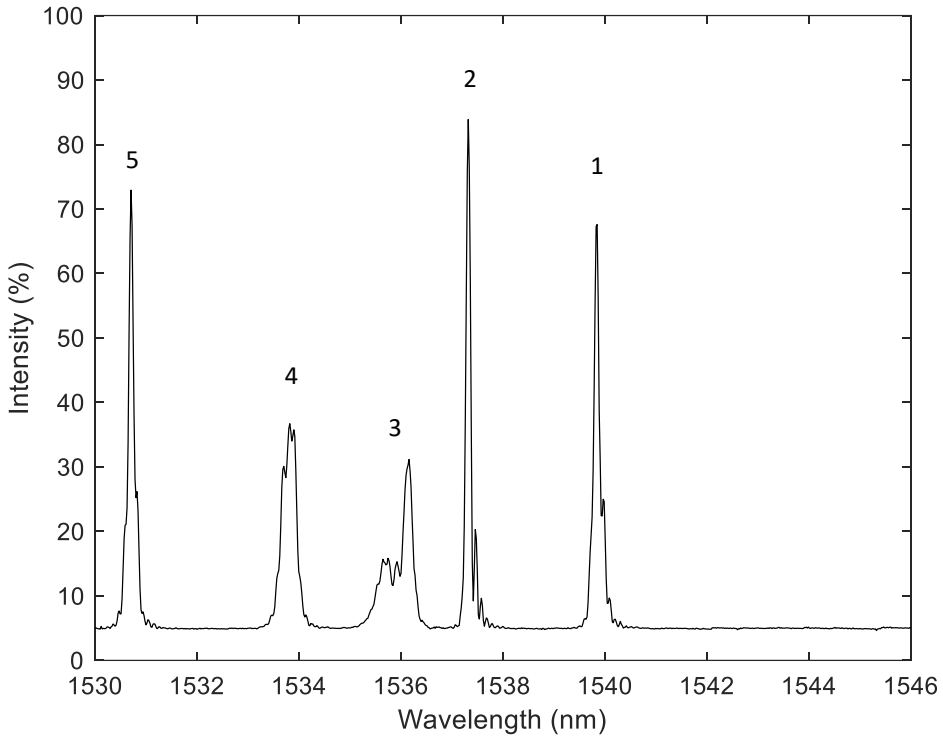

Figure 3.13 Example of reflected spectrum of 5 FBG sensors after curing in the epoxy block.

Sensor FBG 3 in this figure represents an extreme example of peak degradation, exhibiting one major peak and several minor peaks. While methods such as the quadratic method require smooth peaks as in Figure 3.5, the centroid method can accurately track the Bragg wavelength of FBGs with abnormally shaped reflected spectrums. However, the realized uncertainty in the Bragg wavelength of a nicely shaped peak is less than that from a degraded peak. Depending on the quality of the FBG reflected spectrum, uncertainties in the Bragg wavelength vary from 0.5 – 5 picometers, or approximately 0.4 – 4 microstrains for a fiber under no strain. The uncertainty in the measured strains in the experiments are conservatively estimated as the greater of either 4 microstrains or 5% of the measured strain.

3.5. Volume Measurements

It is of interest to know the fracture volume to compare measured fracture pressure and radius with radial fracture theory. The net fracture pressure, P_{net}, and radius, R, are given as a function of fracture volume, V_f, according to Equations 2.58 and 2.59 (reproduced below for reference).

$$P_{net} = \left[\frac{\pi^3 K_{IC}^6 (1-\nu^2) E^2}{12 E V_f}\right]^{\frac{1}{5}} \tag{3.9}$$

$$R = \left(\frac{3 V_f E}{8\sqrt{\pi} K_{IC} (1-\nu^2)}\right)^{\frac{2}{5}} \tag{3.10}$$

Recall that in these equations, K_{IC} is fracture toughness, ν is the Poisson's ratio of the epoxy, and E is Young's modulus of the epoxy.

During the fracture tests, the syringe pump displaced fluid at a constant rate of 0.25 mL/min. The accuracy of the injection rate setting was validated by pumping at a constant rate into a burette for a set period. Negligible uncertainty is associated with injected fluid volumes. However, because the injected fluid volumes are small, fluid compressibility is non-negligible in determining the fracture volume. As the pressure increases in the injection tubing and syringe pump cavity, some displaced volume is stored in the system as the injected fluid is compressed. Therefore, the injected volume does not represent the volume in the fracture.

3.5.1. Model of System Compressibility to Estimate Fracture Volume

The volume injected into the fracture, V_f, is the difference of the injected volume, V_{inj}, and volume stored in the system due to fluid density changes, V_{sys}.

$$V_f = V_{inj} - V_{sys} \tag{3.11}$$

Calculating the volume in the fracture depends on estimating the volume stored in the system due to compressibility. Although the experimental procedure is designed to minimize air in the fluid system and wellbore, invariably a small but non-negligible amount of air remains in the system. The system compressibility is thus modeled as a two-phase system comprised of air (gas) and water (liquid). The isothermal compressibility of a fluid is defined as (Moran and Shapiro 2000):

$$c = \frac{-1}{V}\frac{dV}{dP} \tag{3.12}$$

where V is the total volume in the system and P is the absolute system pressure. It is convenient to rearrange Equation 3.12 for the differential change in volume due to a differential change in pressure.

$$dV = -cVdP \tag{3.13}$$

The gas and water phases are modeled as insoluble, so any change in the total system volume, V_t, is the sum of the change in volume of gas and water.

$$dV_t = dV_g + dV_w \tag{3.14}$$

Substituting Equation 3.13 yields:

$$c_t V_t dP = c_w V_w dP + c_g V_g dP \tag{3.15}$$

The volumetric fractions of the water and gas, F_w and F_g sum to unity.

$$F_w + F_g = 1 \tag{3.16}$$

Therefore, canceling out dP in Equation 3.15 and dividing by the total volume yields:

$$c_t = c_w F_w + c_g F_g \tag{3.17}$$

Thus the total compressibility can be modeled as a linearly weighted sum of the water and air compressibility and their volumetric saturations. Combining the definition of the total system compressibility (Equations 3.12) and 3.17 yields:

$$(F_g c_g + F_w c_w)dP = \frac{1}{V} dV \tag{3.18}$$

The compressibility of water, c_w, is assumed constant, while the isothermal compressibility of an ideal gas depends on pressure (Dake 1978).

$$c_g = \frac{1}{P} \tag{3.19}$$

Further combining and posing the integral yields:

$$\int_{P_i}^{P} \left(\frac{1}{P}(1 - F_w) + F_w c_w \right) dP = \int_{V_i}^{V_i + V_{sys}} \frac{-1}{V_i} dV \tag{3.20}$$

Here, V_i represents the initial volume of fluid and V_{sys} represents the change in volume stored in the system. It is not safe to assume the volumetric water saturation is constant with pressure. Air compresses much more quickly than water, especially at low pressures. A better model is:

$$F_w = \frac{V_w}{V_w + V_g} \approx \frac{V_{wi}}{V_{wi} + V_{gi}\frac{P_i}{P}} \tag{3.21}$$

where V_{wi} and V_{gi} are the initial volumes of water and gas in the system. P_i here represents the initial absolute pressure, which was atmospheric in the experiments. Integrating Equation 3.20 after substituting Equation 3.21 yields:

$$V_{sys} = V_i \left[1 - \frac{P_i}{P} e^{c_w (P_i - P)} \left(\frac{V_w P + V_{gi} P_i}{V_w P_i + V_{gi} P_i} \right)^{1 - \frac{c_w V_{gi} P_i}{V_w}} \right] \tag{3.22}$$

3.5.2. Model Application to Estimate Fracture Volume

Equation 3.22 proved useful in accounting for the volume stored in the fluid system due to fluid compressibility effects when estimating the volume in the fracture. The unknown variables V_w, V_{gi}, and effective c_w are tuned in each experiment to match the measured pressure prior to fracture initiation. Figure 3.14 shows an example where Equation 3.22

was tuned to match the measured data during a fracture experiment prior to fracture fluid filling the initial flaw. The tuned parameters are provided in Table 3.2.

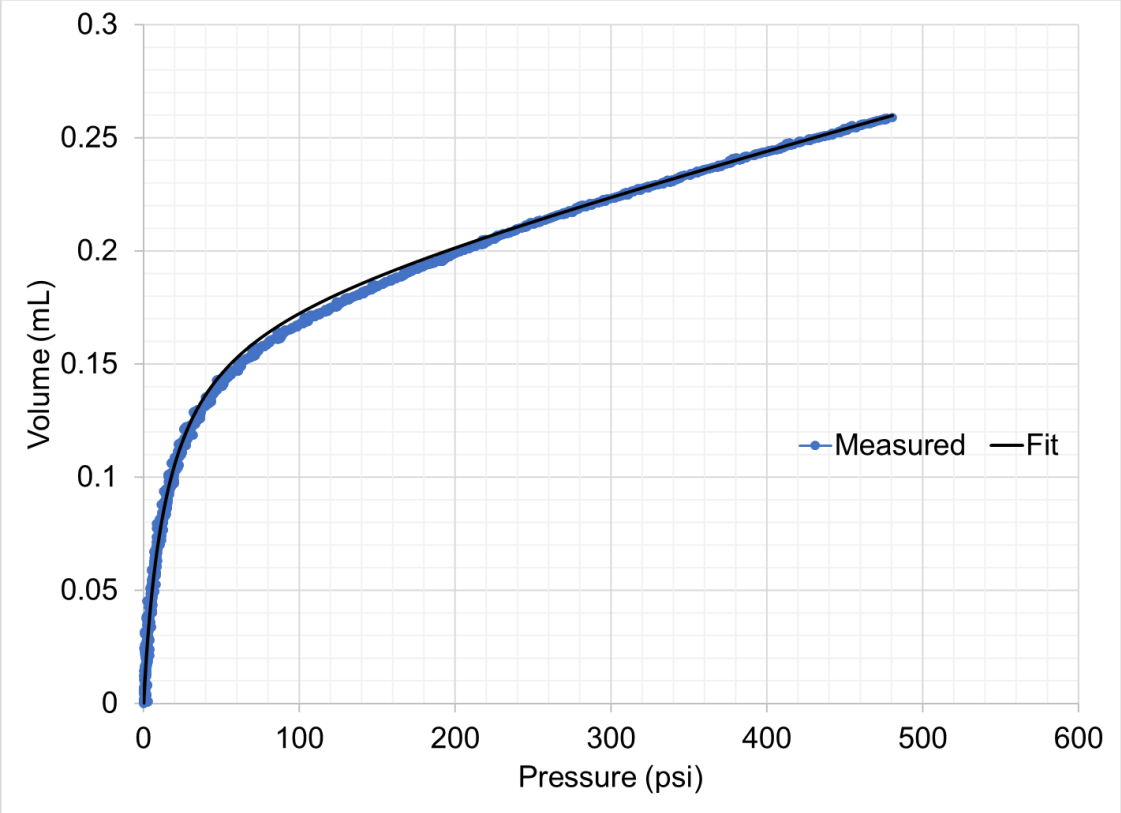

Figure 3.14 Measured and best fit injected volume vs. pressure prior to fracture initiation.

Table 3.2 System compressibility model tuned parameters

Parameter	Tuned Value
V_i, initial volume (mL)	11.75
$F_{w,i}$, initial water volume fraction	0.985
c_w, water compressibility (1/psi)	1.60e-5
P_i, initial pressure (psia)	14.7

The initial volume of 11.75 mL is close to the initial volume of the syringe pump plus the capacity of the injection lines. The curve fit suggests that 98.5% of the volume in the system is initially occupied by water. If there was no air in the system, the volume-pressure relationship would be a straight line. The curve in the volume-pressure relationship comes from the 1.5% volume of air that is estimated to be in the system. Using published values for water compressibility did not result in a good match with measured data. One reason may be that the dye used to color the water altered the compressibility significantly. More probably is that elastomeric sealing components within the syringe pump deform significantly with increasing pressure. Therefore, the water compressibility and initial water fraction were tuned to include effects of any material in the system that compresses linearly with pressure.

To show the significance in compressed fluid volumes, Figure 3.15 illustrates the difference between the injected volume and fracture volume in one of the fracture tests. When fracture fluid fills the initial flaw at 62 seconds, the injected fluid volume is 0.26 mL, whereas the estimated fracture volume is 0.05 mL. The red curve indicates the volume estimated to be stored in the system (V_{sys}). This is exactly equal to the difference in the injected volume and fracture volume. Prior to fracture fluid filling the initial flaw, 100% of injected volume is stored in the system. At the end of the experiment, the

volume stored in the system represents 13% of the total injected volume. Error in estimating the volume in the fracture would propagate to the modeled fracture pressure and radius. From Equations 3.9 and 3.10, fracture pressure is proportional to $V_f^{-1/5}$, and fracture radius is proportional to $V_f^{2/5}$.

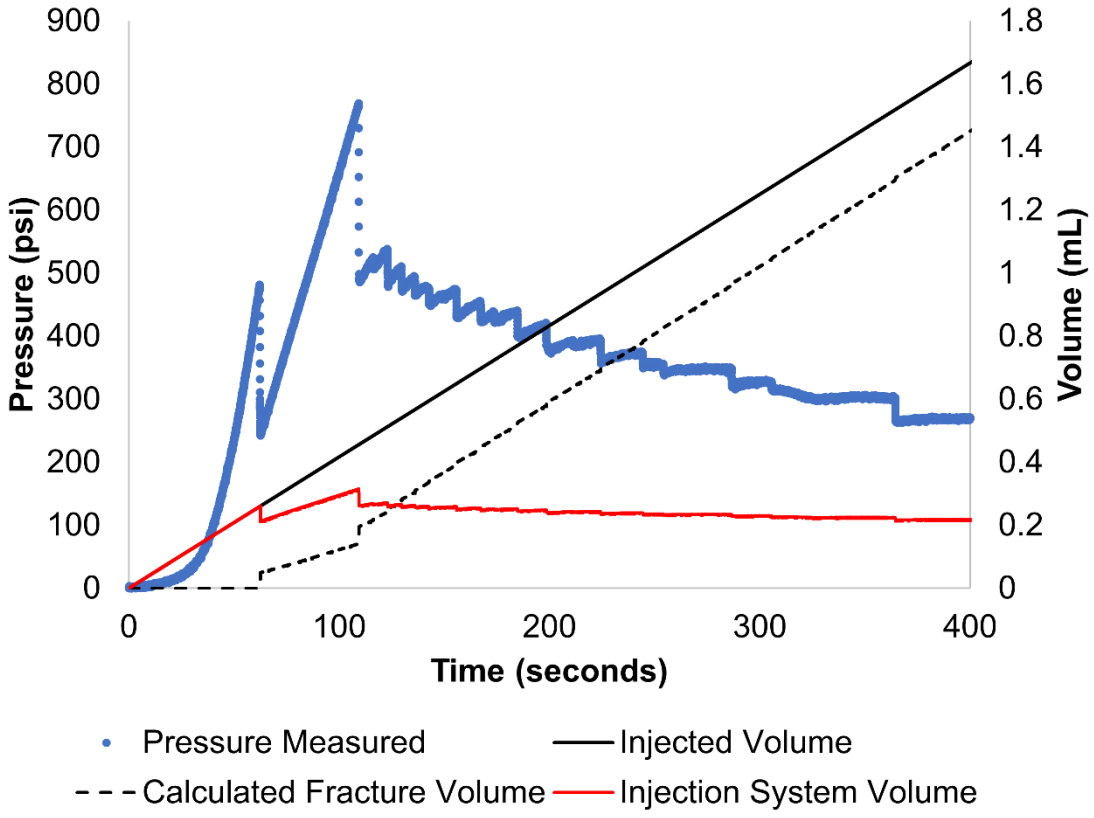

Figure 3.15 Example of difference between injected volume and fracture volume.

3.6. Specimen Preparation Procedure

The following list contains a detailed procedure for creating an epoxy fracture specimen with embedded FBG strain sensors. Steps 1 through 9 deal with creating the mold and the fiber positioner. These steps are not necessary if an existing mold and fiber positioner are reusable.

1. Prepare the wooden mold for the epoxy block. Use a table saw to cut pieces with the following dimensions from 3/4-inch plywood. To attain uniform heights for the mold sides, it is recommended to make all the 8 ½-inch cuts at one time (do not adjust the table saw rip fence between cuts). The same reasoning applies for the 9 ½-inch and 8-inch cuts.
    a. (2) 9 ½-inch x 9 ½-inch pieces (for the base and fiber positioner)
    b. (2) 8-inch x 8 ½-inch pieces (sides)
    c. (2) 9 ½-inch x 8 ½-inch pieces (sides)
2. Measure and record the actual dimensions of the cut pieces accurately to within $1/100^{th}$ of an inch.
3. Select the smoothest surfaces of the plywood pieces to be used for the inside of the mold and cover with two layers of Tuck Tape Construction Sheathing Tape. Ensure that the second layer of tape covers the seams of the first layer to prevent any seepage of epoxy between the tape edges into the plywood. Using only one layer of tape or not overlapping the seams has resulted in epoxy seepage into the plywood mold in the past.

4. Using calipers, dimension and mark the center of the base with a fine-tipped pen. Also place cross-shaped marks 2 inches offset from the center towards each edge. These are used as location markers to verify that the fiber optic cables are hanging in the correct position.
5. Using square clamps, carpenter squares, an electric drill, and #6 x 1 ½-inch screws, construct a rectangular box with 8-inch x 8-inch x 8 ½-inch inner dimensions as shown in Figure 3.16. The mold height is designed at 8 ½ inches, so the epoxy does not need to be poured to the very brim for an 8-inch block. Pre-drill the screw holes with a countersunk top to prevent the plywood from cracking. Mark the top and bottom of each side and label the sides as North, South, East, and West, to make it easier to reassemble the box. The labels also serve as a reference for placing the mold in the exact same position on the table to achieve level surfaces.

Figure 3.16 Epoxy block mold.

6. Caulk the inner seams of the box using silicone caulk to prevent epoxy from leaking out of the mold. Smooth the seams with a caulk finishing tool. After the caulk dries, fill the mold completely with water and check for leaks. Images of the necessary tools and caulked seams are exhibited in Figure 3.17.

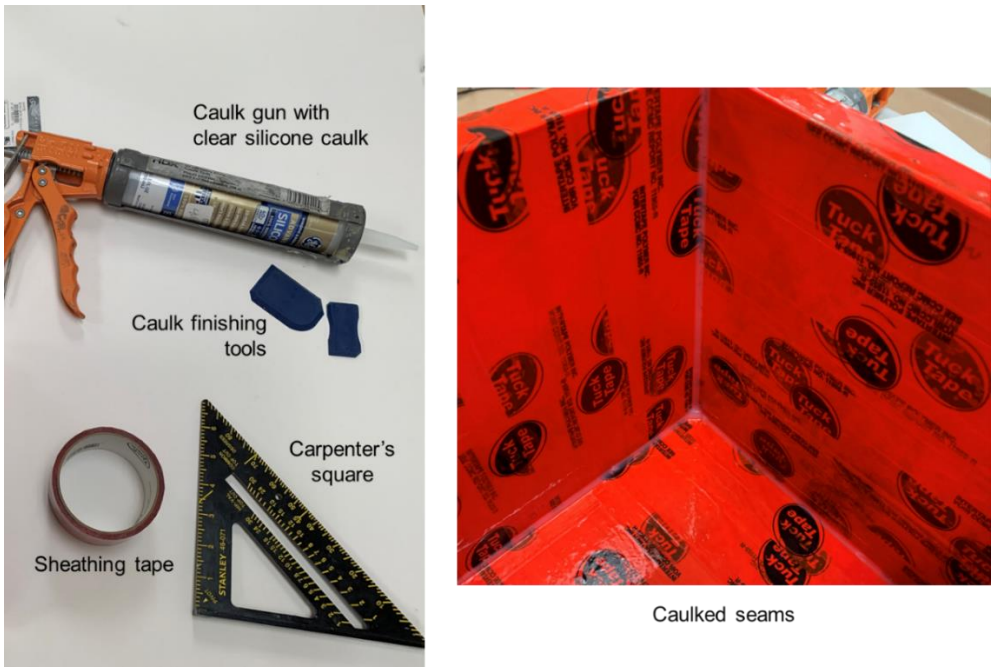

Figure 3.17 Tools used for constructing the epoxy mold.

7. Using a table saw and electric drill, construct the fiber positioner out of the remaining 9 ½-inch x 9 ½-inch plywood piece as exhibited in the following figures. The 1/8-inch slots are used to guide the fibers to rest at exactly 2 inches away from the center of the block. Sand the edges of the 1/8-inch slots to avoid any sharp edges that might cut or damage the fibers.

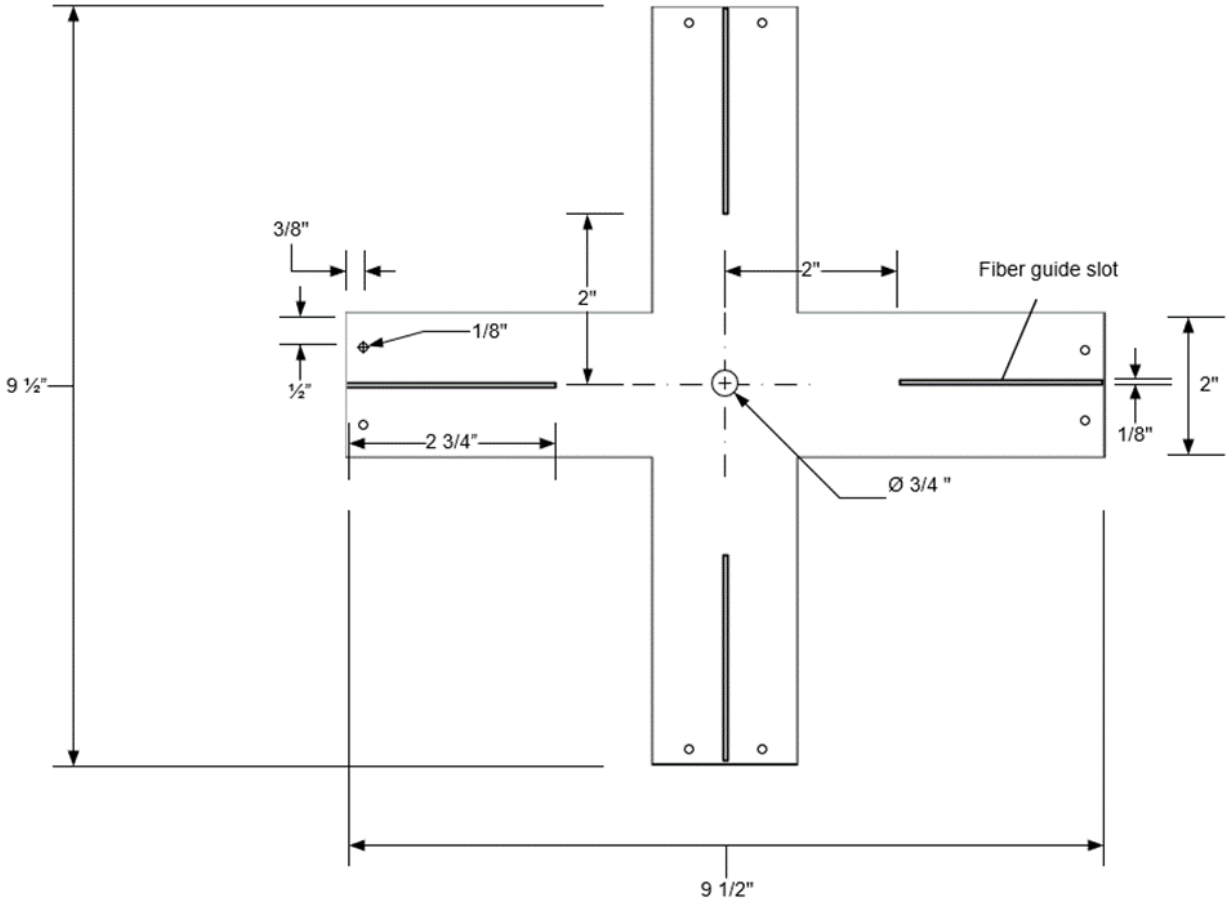

Figure 3.18 Dimensioned schematic of the fiber positioner.

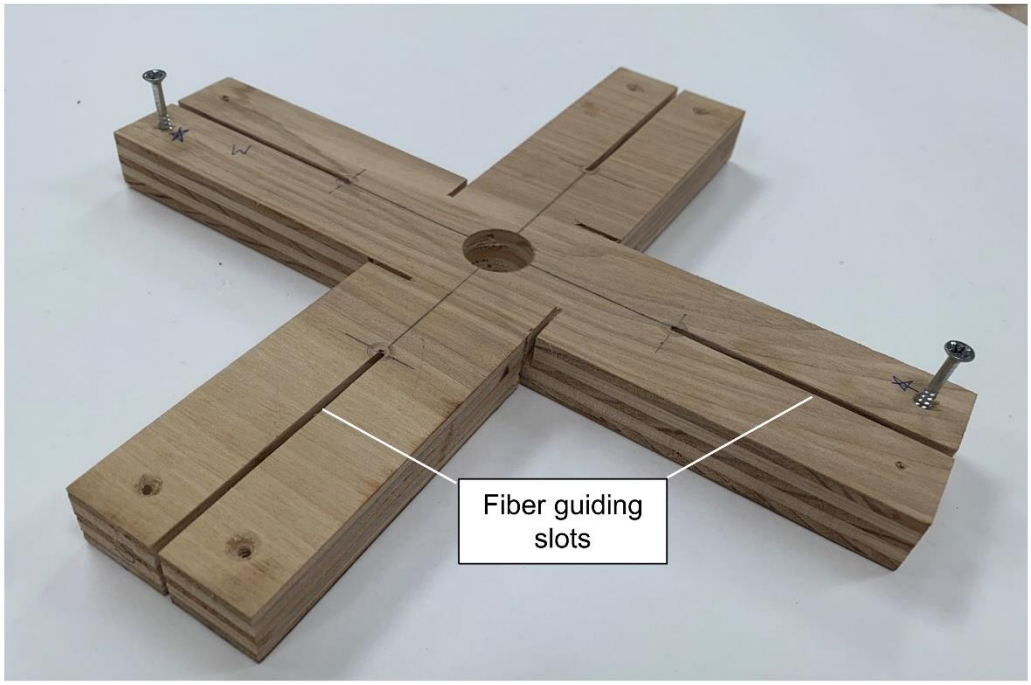

Figure 3.19 Image of a constructed fiber positioner.

8. Measure the thickness of the fiber positioner. Nominally 3/4-inch plywood is closer to 0.73-inches thick.
9. Place the fiber positioner on top of the mold. Ensure it is centered by aligning its ends with the edges of the mold and screw the fiber positioner in place. Be sure to mark which side is facing up and which sides are North, South, East, and West so that it can be put back into the exact same position when removed.

Figure 3.20 Fiber positioner assembled to the top of the epoxy mold.

10. Prepare to pour the epoxy in the mold. Ensure the box is in a well-ventilated, temperature-controlled environment. Maintain the room temperature at a constant 72 ºF +/- 1 ºF on days, nights, weekends, and holidays. The location should be away from windows and not directly under an air vent. Major walkways in the room should be avoided so the box is not accidently bumped or jostled.
11. Use a bubble surface level to ensure that the table the mold is resting on is level. Place scrap wood and washers under the legs of the table to adjust the level as

needed. Verify that the bottom of the mold and the top of the fiber positioner are level.

12. Conduct the fiber-strain calibration procedure for the fiber(s) to be embedded.
13. Design the depth placement of the FBG sensors. The following figure includes an example design for co-located arrays of FBG sensors spaced 5 millimeters apart. Key design considerations include:
    a. All FBG gratings in the array should fit within an 8-inch span.
    b. The center of one of the FBG sensors should pass through the fracture plane, 4 inches above the bottom of the mold.
    c. Place a mark on the fiber that will align with the top of the fiber positioner. This fiber depth marker, displayed as a red dot on the following figure, is used when hanging the fiber in place to ensure the fiber is in position.

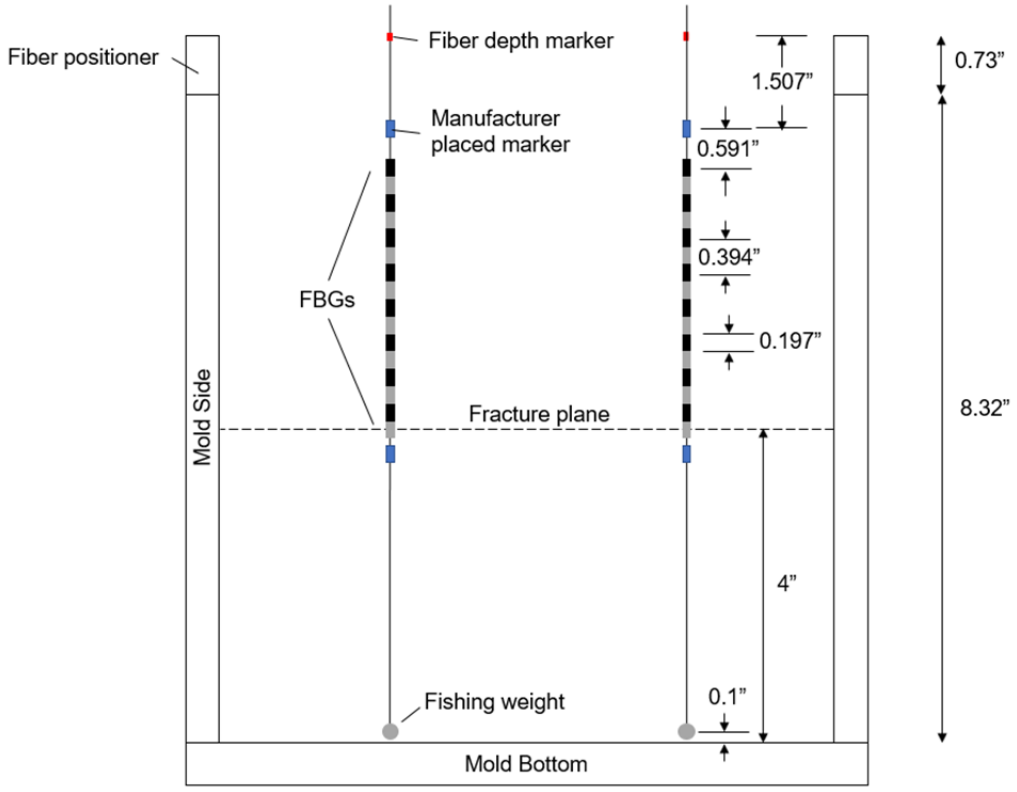

Figure 3.21 Example design of the locations of the FBG sensing arrays. Each fiber is located 2 inches offset from the center of the initial flaw.

14. Trim excess fiber on the bare, non-connectorized end so that the end of the fiber hangs approximately 0.1 inches above the mold bottom. Best practices for trimming the end of the fiber include:
    a. Connect the fiber to SmartScope and ensure the noise floor is not above ~7%.
    b. Use pliers and cut a small portion of the fiber at a 45° angle to minimize reflection of the laser at the end of the fiber.

c. View the reading on the SmartScope and ensure that the cut did not cause the noise floor to rise above 7%.

15. Prepare the fiber(s) to be embedded as follows.
    a. Take a baseline measurement of the FBG peaks on the SmartScope and save the spectrum. This will be used to monitor distortion of the reflected spectrum due to volumetric shrinkage of the epoxy.
    b. Disconnect the fiber from the SmartScope and put the protective cap back on the end of the fiber.
    c. Thread the bare end of the fiber through a slot in the fiber positioner.
    d. Clamp a fishing weight to the end of the fiber. Round split shot size 3/0 weighing 0.85 grams works well.
    e. Using magnetic kitchen clips and the metal test tube stand, suspend the fiber in place. Ensure the fiber depth marker aligns with the top of the fiber positioner.
16. If the hanging fiber does not line up over the cross marks at the bottom of the box, the surface on which the mold is resting may not be level, or the box may be slightly non-square. Level the table surface as needed. Figure 3.22 and Figure 3.23 show how the fibers should suspend over the epoxy block held in position by the fiber positioner.

Figure 3.22 FBG sensing arrays suspended over the epoxy mold through the fiber positioner (left). Fishing weights hang slightly above the bottom of the epoxy mold 2 inches offset from the center (right).

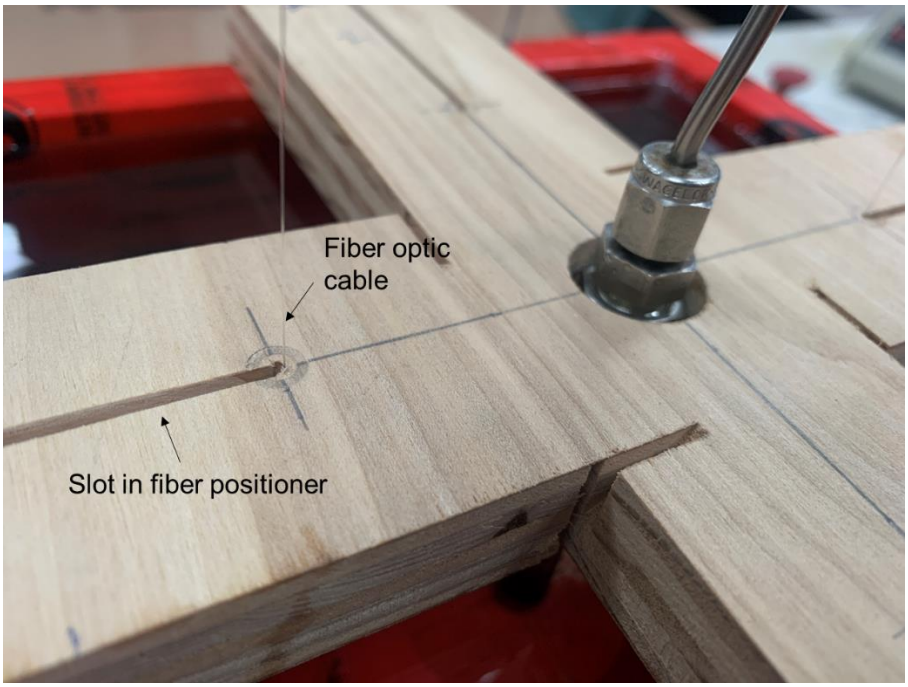

Figure 3.23 Close up view of fiber placement in the slot of the fiber positioner.

17. Make four measurements of the distance from the bottom of the mold to the top of the fiber positioner, one in each quadrant of the box. The measurements will be used to determine the actual thickness of each epoxy pour.
18. Vacuum the inside of the box to remove any particles that could contaminate the epoxy.
19. Mix 987.9 mL (1096.6 grams) of EcoPoxy Flowcast Resin with 494.0 mL (484.09 grams) of EcoPoxy Flowcast Hardener in a plastic beaker. Immediately stir with an electric mixer and stirring paddle for 3 minutes. Pour the first layer of the epoxy. The volumes provided here should result in an 8-inch x 8-inch x

1.333-inch-thick layer. If modified, the volumetric ratio of resin to hardener should remain at 2:1.

20. Wait 5 to 10 minutes after pouring and look for bubbles. Eliminate them by using a paper clip to disturb them or by applying brief blasts from a heat gun. Remove any floating particles of debris that the vacuum did not remove. Clean the beaker and stirring paddle with isopropyl alcohol.
21. Repeat steps 17 through 20 twice to pour layers 2 and 3, waiting 72 hours between pouring each layer. If the measured thicknesses are not precisely 1.333 inches, consider adjusting the volumes of resin and hardener as needed, always maintaining a 1:2 ratio of hardener to resin by volume.
22. Create the initial flaw. Obtain sticker paper from a local print store. Using the punch tool, cut out a 2-inch diameter hole and remove the sticker part. Use the 2-inch diameter non-stick plastic as a guide to cut a 2-inch initial flaw from a piece of sheathing tape. Measure the actual diameter and mark the center of the sheathing tape. The following images display the required tools and end result.

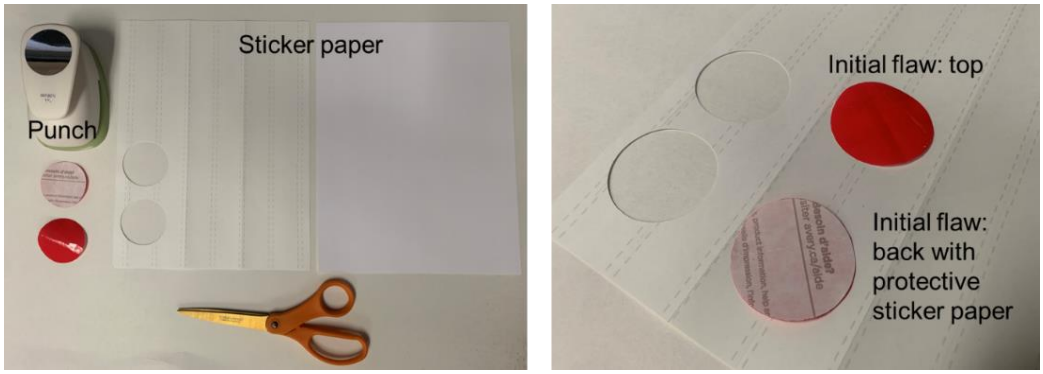

Figure 3.24 Tools used to create the initial flaw.

23. Remove the fiber positioner from the mold. Mark the center location between the two fibers and measure the relative distance between this mark and each fiber, as well as to the edges of the mold. These measurements are important for accurately knowing the distance from the tip of the initial flaw to the fibers.
24. Carefully place the center of the tape to be used as the initial flaw on the marked center of the block. Measure the shortest distance from the tip of the tape to each fiber.
25. Repeat steps 17 through 20 to pour the fourth epoxy layer.
26. Measure layer four thickness as in step 17.
27. Remove the fiber positioner and carefully tape the loose ends of the fibers to the edges of the outside of the block. Mark the center of the block.
28. Use a mill press to drill a ½-inch diameter hole for the injection tubing. Check the mill press alignment with a carpenter square to ensure the drill bit is

perpendicular to the drill table. Clamp the model to the mill press table as shown in Figure 3.25. Failure to do this can result in a hazardous scenario where the drill bit catches on the epoxy and spins the entire block.

29. Drill a ½-inch diameter by 1.5 to 1.6-inch deep hole in the center of the cube that penetrates the center of the tape. The end of a drill bit is tapered; ensure the full ½-inch diameter portion of the bit fully penetrates the initial flaw. Secure the mold with clamps so that the block cannot rotate or rock out of position.

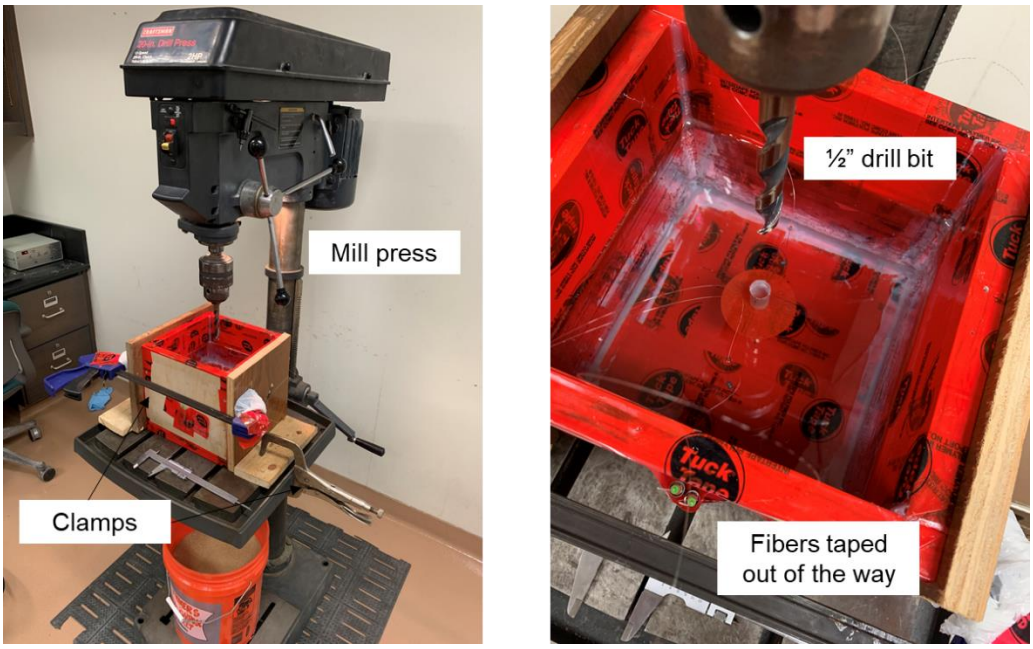

Figure 3.25 Mill press setup used to the drill the hole for the injection tubing.

30. Epoxy the injection tubing in place as follows:

a. Prepare a 5-inch long by ¼-inch diameter by .035-inch wall thickness 316 stainless steel tubing open ended on one end with a compression fitting and ¼-inch by 1/8-inch reducer fitting on the other end. Connect a short piece of 1/8-inch SS tubing and a 6,000 psi rated ball valve to the end with the compression fitting.

b. Rough up the surface of the tubing with 120 grit sandpaper to improve adhesion with the epoxy.

c. Slide a Buna N black 70 Shore A (NBR 70) AS568 (#-202) 1/8x1/4 O-ring over the bare end of the tubing. Measure the O-ring thickness; it should be slightly less than 0.15 inches.

d. Connect the injection tubing to the syringe pump. Fill the tubing with distilled water mixed with 2 drops of food coloring per milliliter of water. Ensure the system is purged of air. Slide the tubing through the fiber positioner.

e. Insert the tubing into the hole in the epoxy block. Use a stand and clamps to support the tubing and to hold it in the center of the hole. Position the O-ring such that it is approximately 0.1 inches above the initial flaw. This can be verified by measuring the distance from the top of epoxy layer four to the top of the O-ring, which should be approximately 1 to 1.1 inches for a 1.333-inch thick epoxy layer.

f. Set the syringe pump at 0.25 mL/min, and slowly fill the anulus beneath the O-ring with dyed water. The goal is to purge air from the system. Look for air pockets trapped beneath the O-ring. If water rises above the O-ring, remove it with a fine tipped syringe.

g. Fill the tubing-hole annulus with 5 minute instant mix Loctite epoxy. Work out any air bubbles with a paper clip. Wipe away excess epoxy that spills over. Wait approximately 1 hour for the epoxy to harden before proceeding.

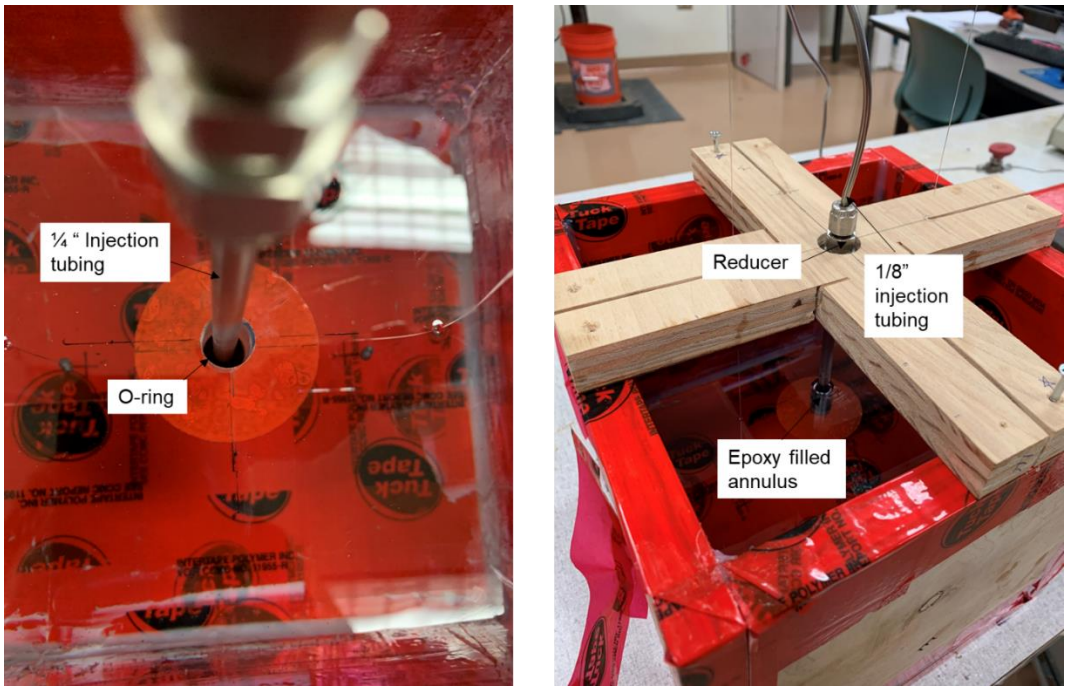

Figure 3.26 Injection tubing before and after it is epoxied in place.

31. Secure the injection tubing so that it has no stored energy and cannot accidently spring free and damage the fibers or epoxy. Screw the fiber positioner back on and re-align the fibers.
32. Repeat steps 17 through 20 to pour layers five and six. Wait one week after layer six is poured. Measure layer six height and calculate the actual thickness of the block.
33. Remove the block from the mold by gently prying the mold sides and bottom off with a flathead screwdriver. Enlist help from a second person to avoid damaging the fibers. Proceed to test the block according to the fracture test procedure.

3.7. Fracture Test Procedure

This section details the procedure for performing the fracture test with embedded optical fibers.

1. Ensure two people are present to handle a block with fibers in it to avoid damaging the fibers when moving the block. Place it on the center of the table.
2. Set up the syringe pump as follows:
    a. Fill the syringe pump with dyed fluid to an initial volume of approximately 6.5 milliliters.
    b. Set the desired flow rate (0.25 mL/min suggested) and run it to make sure it is correct.
    c. Set the desired refill flow rate (0.1 mL/min suggested) to simulate flowback/fracture closure.
    d. Ensure that air is purged from the syringe pump system.
    e. Ensure there is no pressure built up in the system and connect the tubing protruding from the epoxy cube to the system.
    f. Ensure all the valves are open to the correct positions to inject fluid into the epoxy cube. If valves are replaced, ensure they have a pressure rating of at least 2,000 psi.
    g. Record the initial volume of the syringe pump.
    h. Ensure the maximum syringe pump output pressure is set at 2,000 psi.

3. Open the Labview file: "Hydraulic_Fracture_test_data_collection_producer_consumer.vi" and perform a test to make sure the pressure data is saving properly.
    a. Press "Run" and then
    b. Check the "write to file settings" and test the program to make sure it is saving pressure data in an accessible location.
4. Ensure the computer clocks for the computers recording pressure and FBG reflected wavelengths are synchronized to within 0.1 seconds. Check this by simultaneously entering with the "time" command on command prompt of both computers. If the time needs to be adjusted, do so, but make sure the SmartSoft program is closed so that the strains are saved at the correct datetime.
5. Connect the fibers to the SmartScope unit and open the SmartSoft data acquisition program.
6. Ensure the computer has sufficient memory for the acquisitions.
7. Do a test acquisition with the "full spectrum plug-in" to ensure that datetime and FBG wavelengths are recorded at 0.2 second intervals.
8. Place the protective plexiglass shield around the epoxy cube.
9. Set up two smartphone cameras to capture footage of the experiment. Position one camera to view the initial flaw and fracture propagation. This camera should be aligned precisely parallel to the plane containing the initial flaw. Position another camera to visualize any fluid leaking along the pipe. Things to consider:

a. Use a bubble app (calibrated to level using a surface bubble level) to ensure the cameras are level.
b. Turn phones onto airplane mode and turn the Wi-Fi off.
c. Place a neutral background behind the cube in the line of the camera. A white piece of posterboard, for instance.
d. Ensure the cameras have enough memory to capture the anticipated duration of the experiment.

10. Start the SmartSoft data acquisition using the plugin that saves the full spectrum.
11. Start the video recording on both cameras.
12. Make sure the cameras are stable and not oscillating.
13. Countdown “3, 2, 1, 0” for the video audio to pick up. Simultaneously on “0”:
    a. Start the pressure acquisition.
    b. Press the start button on the syringe pump.
14. Monitor the pressure and frac growth. When the fracture is approximately ½ inches away from the edge of the block, stop the pump.
15. Immediately record the final volume of the syringe pump, and then run the pump in reverse to simulate fracture closure. Do this by pressing “Refill” on the pump controller. A rate equal to or less than the injection rate is recommended.
16. Monitor the pressure. Stop the syringe pump when the pressure reaches 0 psi.
17. Stop the pressure acquisition. Stop the SmartScope and collect the saved files.

3.8. Epoxy Mechanical Property Characterization

Using epoxy for the fracture specimens provides desirable strain transfer from the fracture medium to the embedded fibers. The suitability of epoxy as a proxy for reservoir rock depends on the extent to which both epoxy and rock can be modeled as linearly elastic. Figure 3.27 exhibits a representative stress-strain relationship for the epoxy from uniaxial tensile tests on dogbone specimens machined from cured epoxy blocks. Stress was computed from the measured force and initial cross-sectional area of the tensile specimens. The strain was measured using an extensometer. Although some creep behavior is observed, a linear fit approximates the stress-strain behavior with an R^2 value of 0.996. The Young's modulus was estimated from the slope of this best fit line as 354,000 psi.

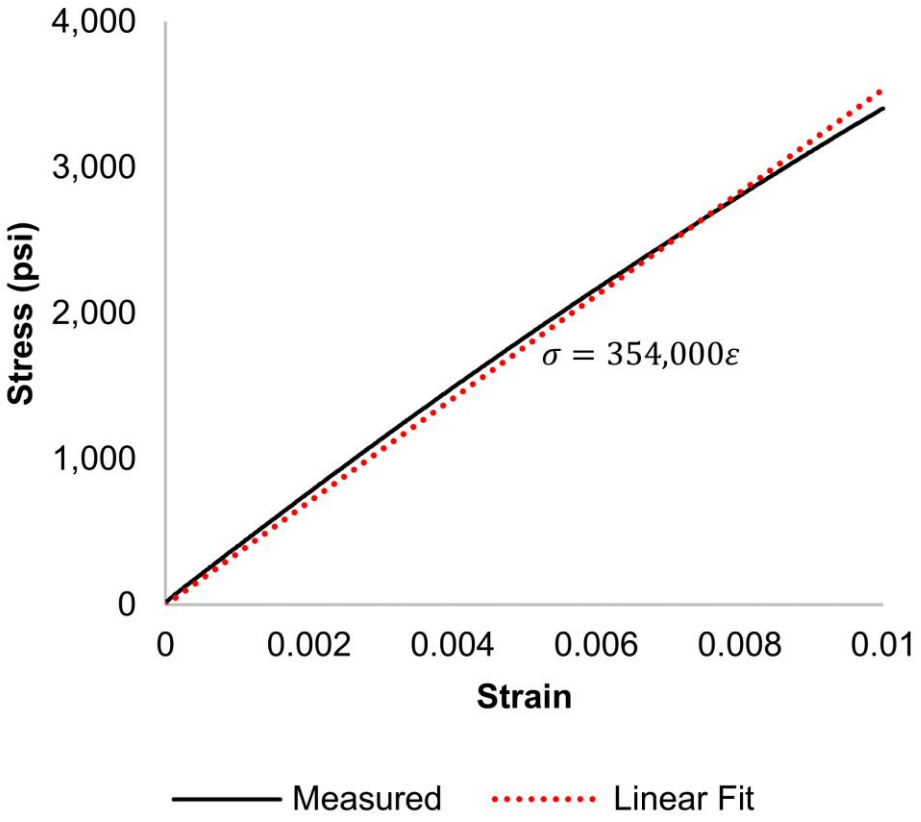

Figure 3.27 Representative epoxy fracture specimen stress-strain curve from a uniaxial tensile test.

4. EXPERIMENTAL RESULTS*

This chapter includes results from the hydraulic fracture lab experiments with embedded fiber optic cables. Fracture geometry and net pressure measurements are compared to radial fracture propagation theory. The measured strains are compared to Sneddon's solution for a radial crack and results from finite element modeling. Heat maps akin to LF-DAS waterfall plots are presented from the experimentally measured strain data. The experiments provide insight into determining where and when a fracture intersects an offset fiber optic strain sensor based on measured strains. Results are provided in dimensionless form to facilitate upscaling the results from lab scale to field scale.

The following sections discuss the measured fracture radius, pressure, and resulting offset strains obtained during the fracture experiments.

4.1. Fracture Radius and Pressure

Radial fractures were propagated when dyed water was injected into the epoxy block through the centered tubing. Figure 4.1 provides an example of a radial fracture generated in the experiments and the location of the embedded fiber optic strain sensing arrays. The fracture specimen in this experiment was oriented such that the fracture propagated in a horizontal plane. The images include: fluid occupying the region of the initial flaw (a), radial fracture propagation in the epoxy towards the fibers (b, c), the fracture intersecting the sensors (d), the fracture propagating past the sensors (e), and the

* Part of this section is reproduced with permission from "Experimental Investigation of Low-Frequency Distributed Acoustic Strain-Rate Responses to Propagating Fractures" by Leggett, S., Reid, T., Zhu, D., and Hill, A.D. 2021. SPE-209135-MS. Copyright 2021, Society of Petroleum Engineers. Further reproduction prohibited without permission.

fracture approaching the edge of the block (f). When the fracture intersects the fiber, the fiber reinforces the epoxy, temporarily deflecting fracture propagation and creating a heart or polar lobe shape (Figure 4.1d). Eventually, the fracture resumes a radial form and continues propagating towards the edge of the block.

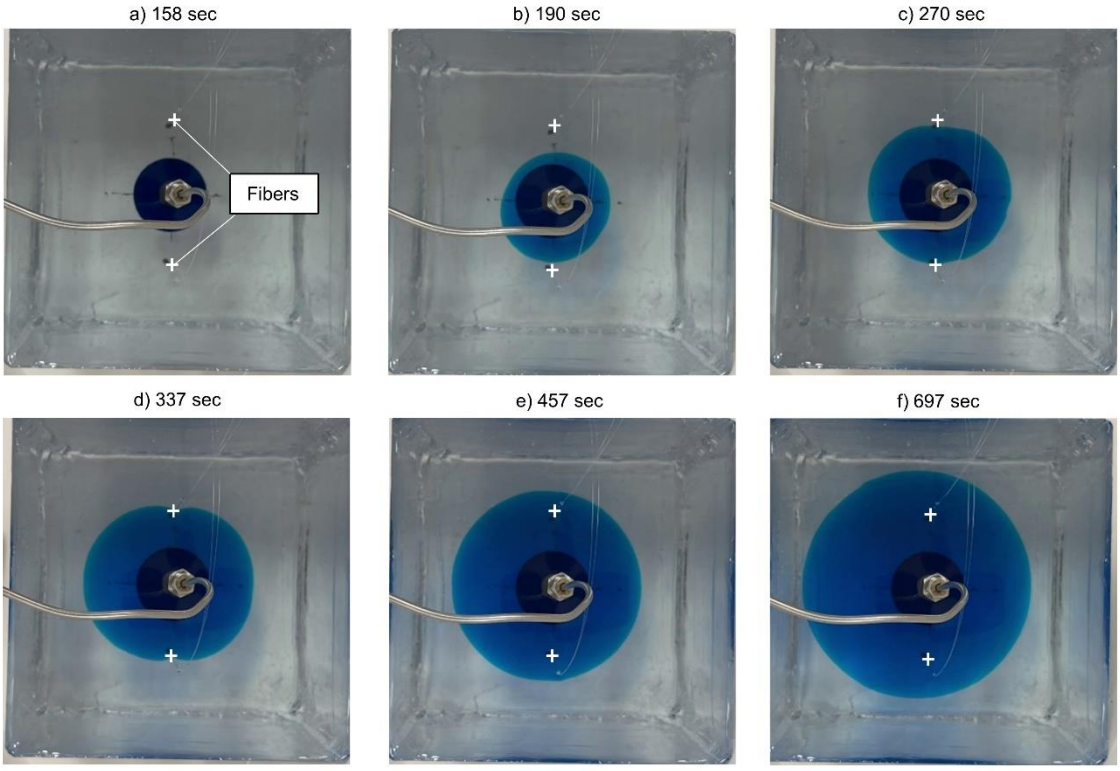

Figure 4.1 Succession of images highlighting radial fracture propagation.

The measured fracture pressure and radii from this experiment are compared with the injection rate in Figure 4.2. The period between 0 and 160 seconds represents the pressure buildup until the fracture propagates beyond the initial flaw. The decrease in pressure at 90 seconds corresponds to the moment when fracture fluid filled the initial 1-inch radius flaw. At 620 seconds, the fracture approached the edge of the block, and the injection rate was reversed to simulate fracture closure.

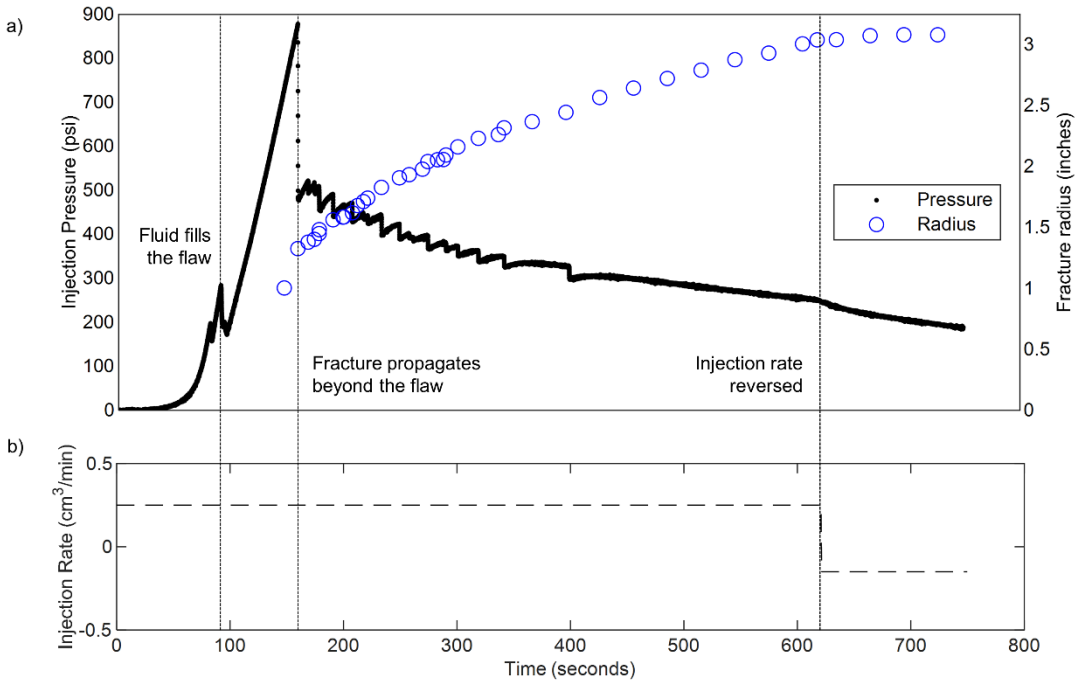

Figure 4.2 Measured pressure and fracture radius compared with injection rate.

The fracture propagated between 160 and 400 seconds in rapid bursts. Each drop in pressure corresponds to a fracture growth event. This sawtooth pressure behavior was observed in each experiment. The correspondence between the radius growth and pressure drop is illustrated in Figure 4.3.

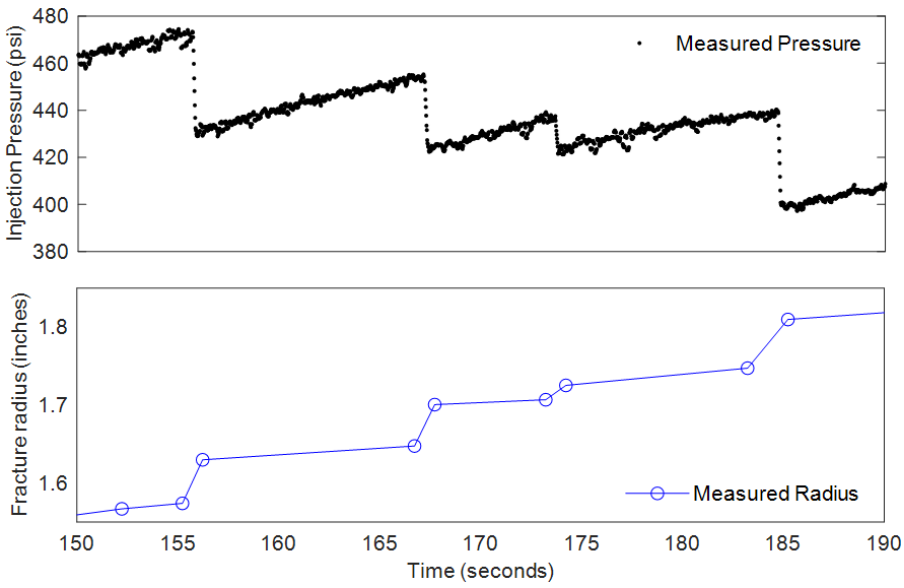

Figure 4.3 Zoomed in view of measured pressure and radius highlighting the correspondence between pressure drops and bursts of fracture growth.

Using estimated values for Young's modulus and fracture toughness, the fracture pressure and geometry can be predicted as a function of volume from Equations 2.58 and 2.59. A Poisson's ratio of 0.35 was assumed. Using the known fracture radius, pressure,

and volume between 90 and 160 seconds, a Young's modulus of 389,000 psi was determined by a rearrangement of Equation 2.49. This agrees with the Young's modulus determined from tensile tests within a 10% uncertainty. A K_{IC} of 665 psi-in$^{0.5}$ results in the modeled curves in Figure 4.4. Here the modeled and measured fracture pressure and radius are compared.

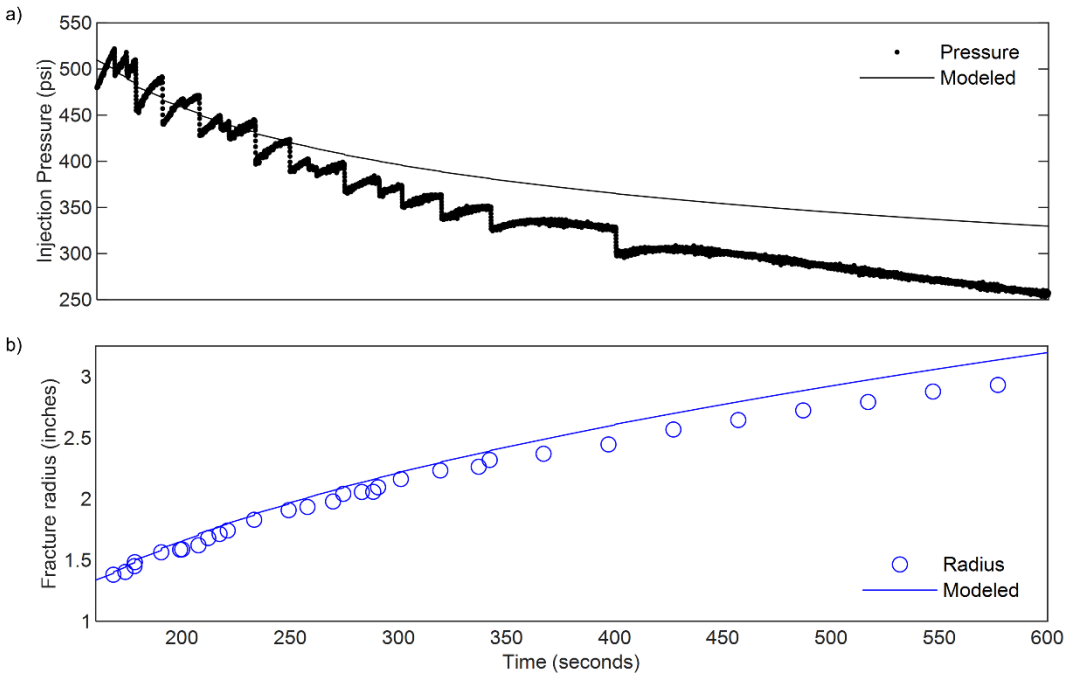

Figure 4.4 Comparison of measured and modeled fracture pressure and radius.

The measured pressure and radius are lower than modeled at later times. Two explanations for the disparity are offered. First, the model assumes an infinite medium, but the epoxy block is only 8 inches in each dimension. Therefore, it is likely that boundary effects become significant as the fracture nears the edge of the epoxy block. Finite element simulations show that the fracture volume for a given radius and pressure is greater in the 8-inch cube compared to the infinite case. Therefore, for a given volume injected into the fracture, the radius observed in the experimental block is expected to be less than predicted by classic radial fracture models, all other things equal. Secondly, the viscoelastic behavior of the epoxy evidenced by the non-linearity of the stress strain curve in Figure 3.27 may contribute to the observed difference. Figure 4.5 displays the measured and modeled pressure and radius behavior from another experiment. Here, the modeled pressure and radius agree more closely with the measurements when compared with Figure 4.4. However, the same trend of the models overpredicting pressure and radius at late times is exhibited.

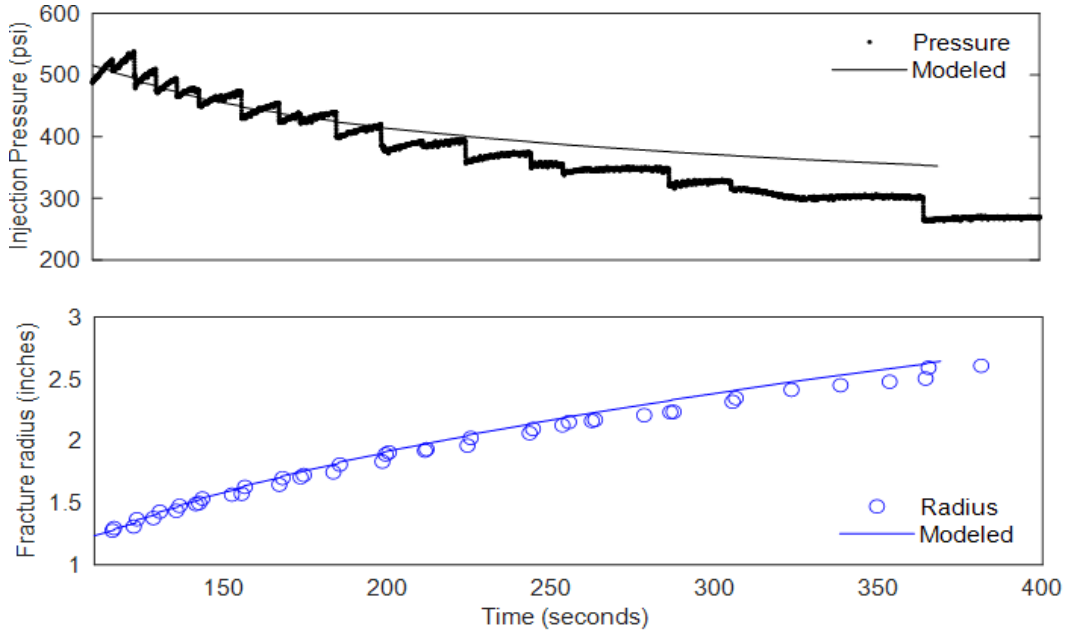

Figure 4.5 Measured verse modeled fracture pressure and radius.

4.2. Measured Strains at Offset Fiber Optic Cables

Strains are computed based on changes in the Bragg wavelength associated with each FBG sensor according to Equation 2.73, reproduced here for reference.

$$\varepsilon = \frac{1}{\zeta_\varepsilon}\frac{\Delta\lambda_B}{\lambda_B} \tag{4.1}$$

Here, ε is axial strain on the fiber, λ_B is the initial Bragg wavelength and $\Delta\lambda_B$ its change, and ζ_ε is the stress-optic coefficient for silica fibers (0.772 in this study).

The measured strains are compared to Sneddon's solution for the far-field strain due to a radial fracture (Equation 2.56, reproduced here for reference).

$$\varepsilon_z = \frac{d}{dz}\frac{-4P_o c(1-\nu^2)}{\pi E}\int_0^\infty \left(1+\frac{z_D\eta}{2R_D(1-\nu)}\right)\left(\frac{cos\eta}{\eta}-\frac{sin\eta}{\eta^2}\right)e^{-z_D\eta/R_D}J_0\left(\frac{\eta}{R_D}\right)d\eta \quad 4.2$$

Here, ε_z is strain in the z direction, P_o is net fracture pressure, c is fracture radius, E and ν are the Young's modulus and Poisson's ratio of a homogeneous, infinite, linear-elastic material, and η is a variable of integration corresponding to the radial coordinate in Hankel space. z_D is the dimensionless z coordinate, R_D is the dimensionless crack radius, both are made dimensionless by dividing by the radial well spacing, or the radial distance from the axis of the fiber to the center of the crack.

4.2.1. Measured Strains vs. Time

Figure 4.6 presents the measured Bragg wavelength over the duration of an experiment for a fiber not intersected by a fracture. Figure 4.7 provides the corresponding strain computed from the FBG response. The FBG locations are detailed in Table 4.1. To interpret the FBG and strain response, the measured fracture pressure, fracture radius, and injection rate are provided in Figure 4.8. Prior to fracture fluid filling the initial flaw (62 seconds), there is understandably no response from the FBGs. The period between when the fracture fluid fills the initial flaw and when it propagates past the flaw into the epoxy (62 – 110 seconds) is marked by a nearly linear change in strain. This is because the fracture radius is not changing; the pressure during this time is increasing almost linearly (Figure 4.8); and strain is proportional to net pressure (Equation 4.2). The responses of the FBGs differ due to their distance from the fracture plane (z coordinate). By symmetry around the plane $z=0$, the response of FBG 3 and FBG 5 are nearly identical. After 110 seconds, the FBGs respond to the propagating fracture until the injection rate is reversed to simulate fracture closure (407 seconds). At this point, the

magnitudes of the strain responses decrease proportionally with fracture pressure until the fracture pressure reaches zero.

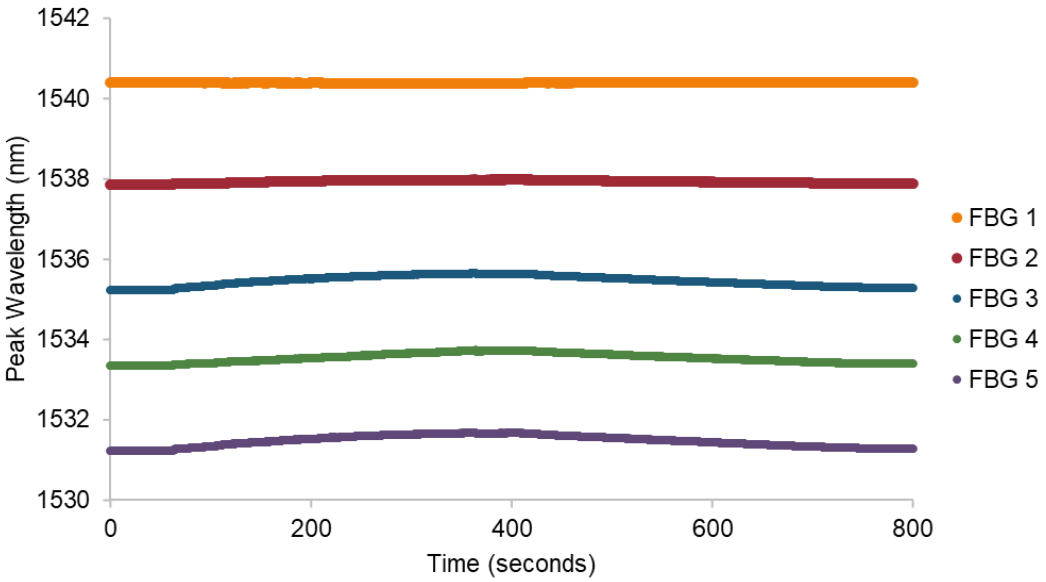

Figure 4.6 FBG response to a propagating fracture when the fracture does not intersect the fiber.

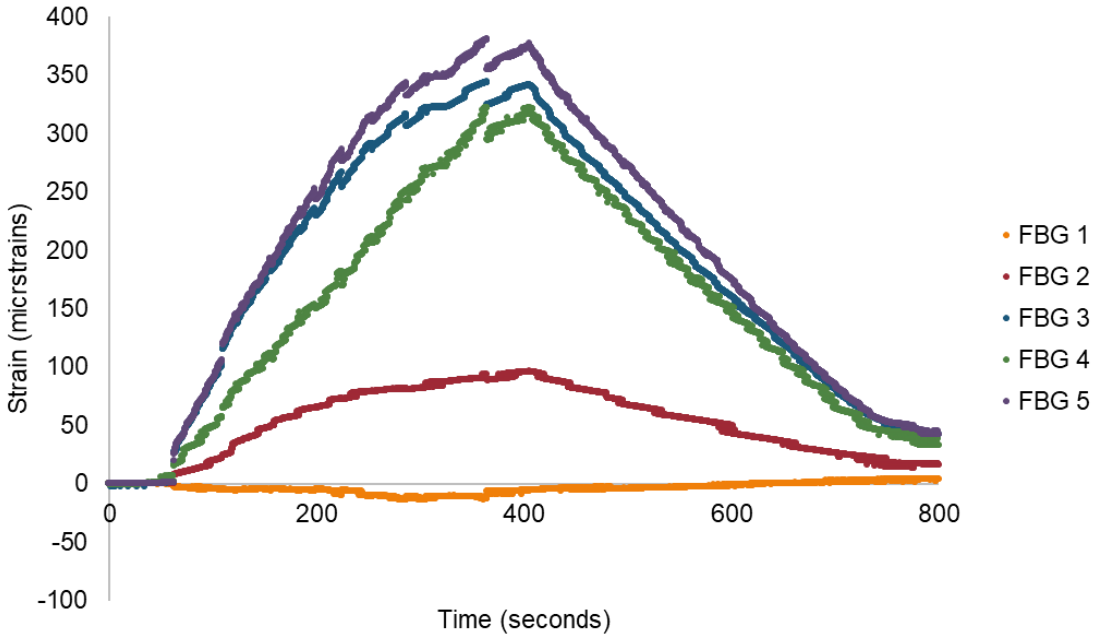

Figure 4.7 Strain computed from the FBG response when the fracture does not intersect the fiber.

Table 4.1 FBG locations.

FBG	Z coordinate (inches)
1	3
2	2
3	1
4	0 (Fracture plane)
5	-1

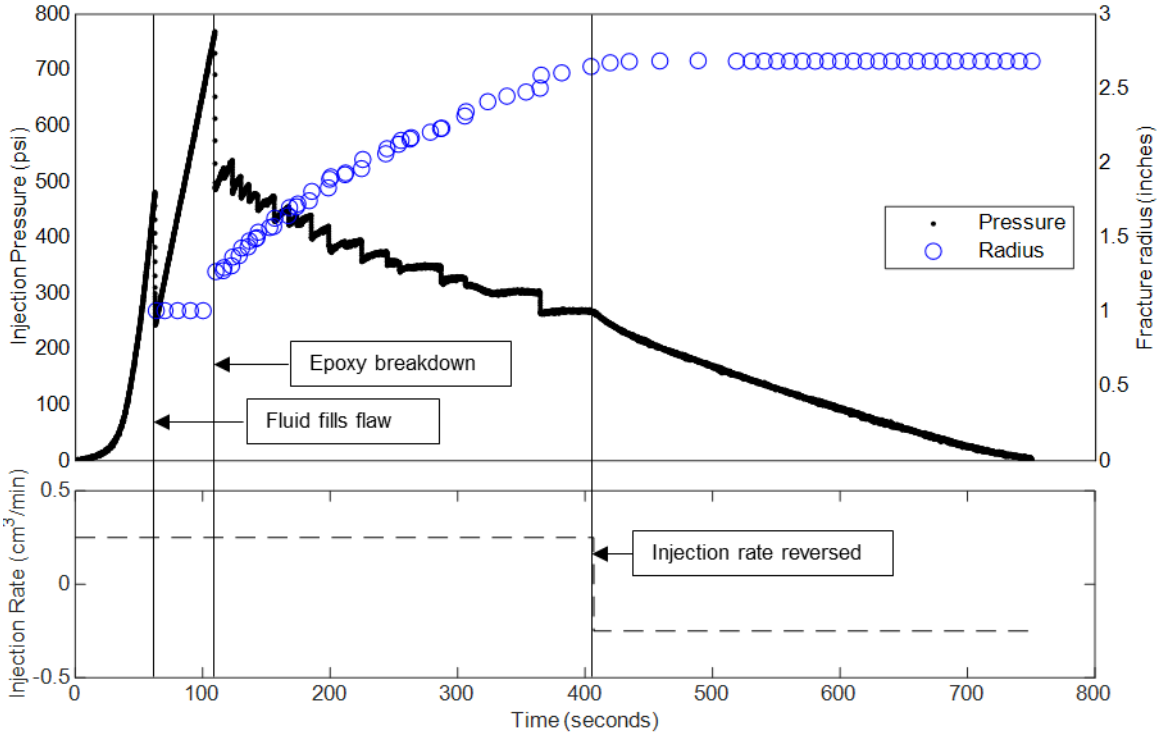

Figure 4.8 Fracture pressure, radius, and the corresponding injection rate for a fracture test.

Figure 4.9 presents the FBG response from a fiber that was intersected by a propagating fracture. The computed strain response is shown in Figure 4.10. These data are associated with the same experiment and FBG locations as the non-frac hit fibers discussed above (see Figure 4.8, Table 4.1). As such, much of the prior discussion needs not be repeated. The major difference is in the response of FBG 4, the sensor located in the fracture plane on the fiber intersected by the fracture. As the fracture approaches and intersects the fiber, the strain at this FBG increases by approximately two orders of magnitudes greater than the other FBGs. Figure 4.10 limits the y axis to visualize the

response of all the FBG gratins; Figure 4.11 expands the y axis to show the full response of FBG 4. The timing of the fracture intersection is indicated by the vertical black line. The apparent discontinuities in the response of FBG 4 between 200 – 400 seconds are rapid, large changes in the strain response corresponding to fracture growth events or debonding events. These phenomena are discussed in detail in section 4.5. Shortly after the fracture intersection, all other FBGs other than FBG 4 show a compressive (negative) strain response. In the non-frac hit fiber, the majority of the FBGs registered a tensile (positive) strain.

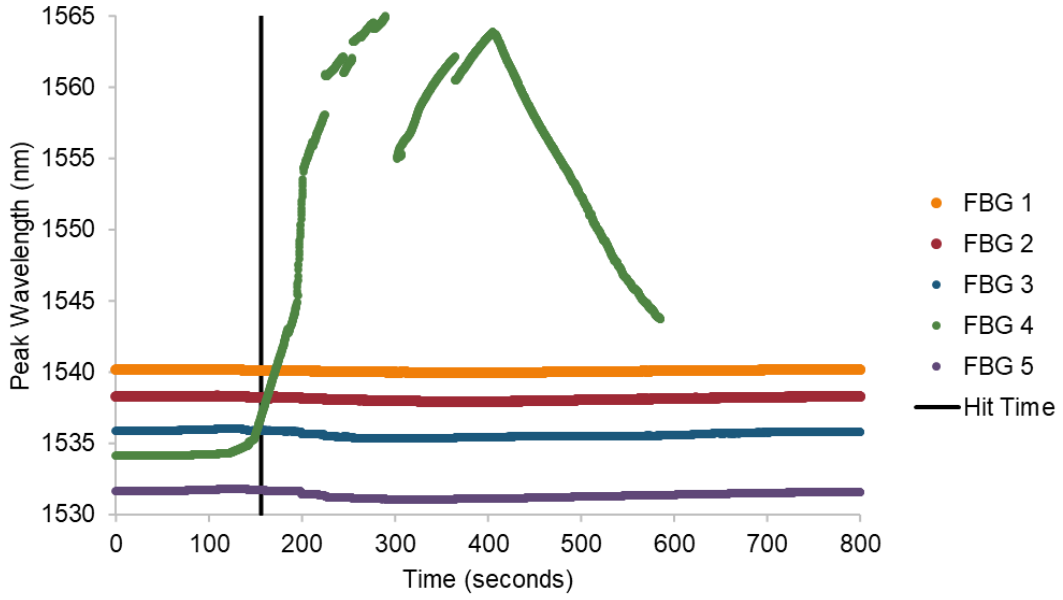

Figure 4.9 FBG response to a propagating fracture that intersects the fiber. The center of FBG 4 was located on the fracture plane.

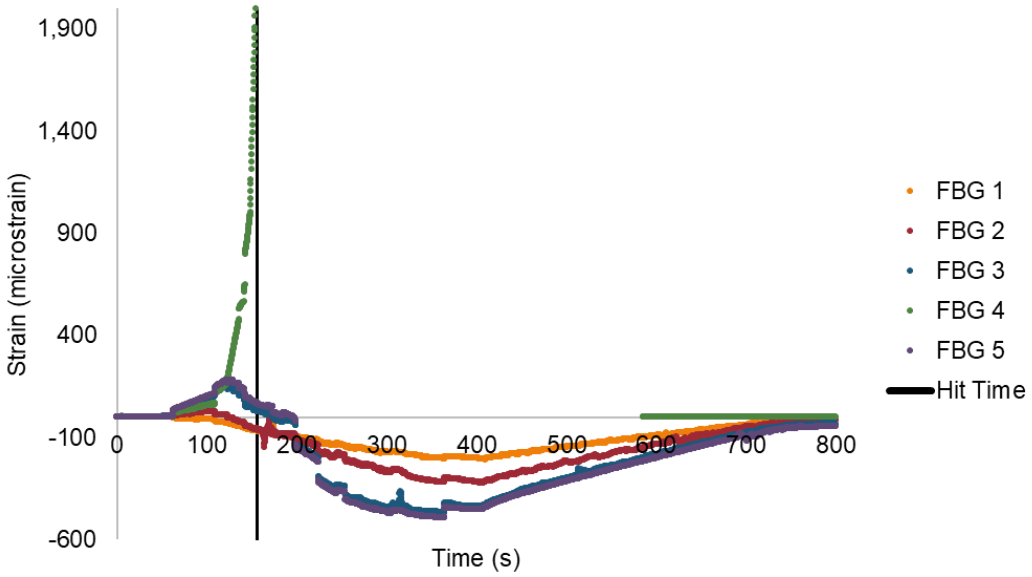

Figure 4.10 Strain computed from the FBG response when the fracture intersects the fiber. The center of FBG 4 was located on the fracture plane. Y axis cropped at 2,000 microstrains to highlight response of gratings not hit by the fiber.

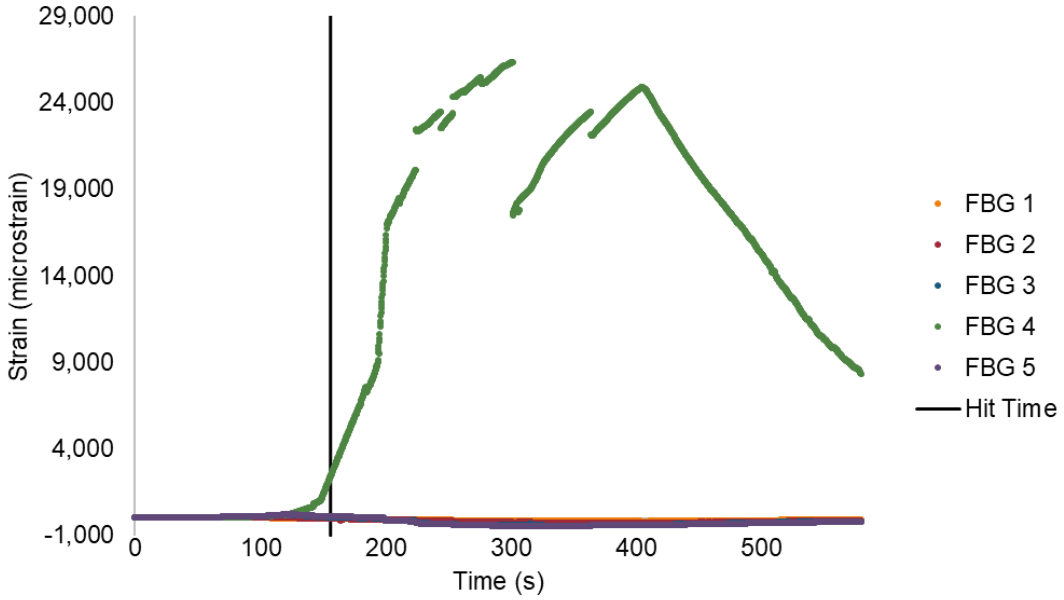

Figure 4.11 Strain computed from the FBG response when the fracture intersects the fiber. The center of FBG 4 was located on the fracture plane. The same data is plotted as in the prior figure with an expanded Y axis to show the full response of FBG 4.

4.2.2. Measured Strains vs. Distance Normal to the Fracture Plane (Z Coordinate)

The measured strains versus the distance each FBG is located from the fracture plane are illustrated in Figure 4.12 at a moment when fracture fluid filled the initial flaw (Figure 4.1a). The strains predicted by Sneddon's solution (Equation 4.2) and the linear-elastic finite element model (section 2.1.2) are plotted for comparison. Two cases from the finite element model are exhibited. The 200-inch cube case validates the finite element model against Sneddon's solution, whereas the 8-inch cube case simulates the actual boundary conditions of the experiment. The 8-inch cube simulation results match the

measured strain within uncertainty. The general shape of the strain curves from Sneddon's solution and the 8-inch finite element model are similar; however, strains predicted by Sneddon's solution do not agree with the measured strains. This is due to the invalid assumption that the 8-inch fracture specimen can be modeled as an infinite medium relative to the 1-inch radius crack.

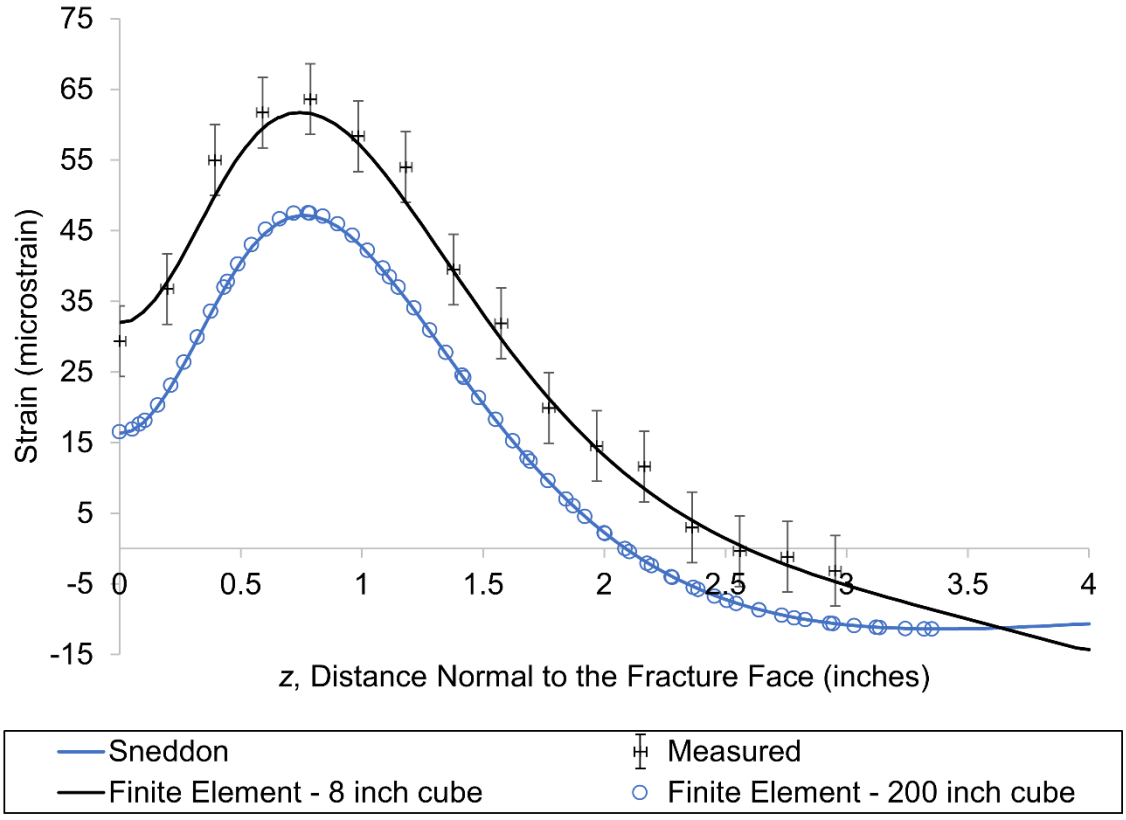

Figure 4.12 Comparison of measured and modeled strains at a single time prior to the frac hit.

To summarize, the 8-inch finite element model agrees with experimentally measured results. When the 8-inch finite element model is expanded to 200 inches, it agrees with Sneddon's solution. The finite element modeling can be viewed as a mapping of Sneddon's solution to the boundary conditions of the experiment. As will be discussed in Chapter 5, it is of special interest to identify the *z* coordinate at which the strain curve crosses the *x* axis, or the location of zero strain. Interpolating from the experimental results and finite element model, the *z* coordinate of zero strain is 2.6 inches. Sneddon's solution predicts a zero strain at 2.1 inches. The ratio of 2.1 and 2.6 is 0.81. A correction or "mapping" factor of 0.8 was found to adequately map the zero strain location predicted by Sneddon to the finite element model across a range of crack radii.

It is assumed in this work that the earth can be modeled as an infinite medium relative to the size of subsurface hydraulic fractures in unconventional oil and gas completions. Therefore, Sneddon's solution is useful in predicting the LF-DAS strain response in field-scale investigations. Applications of Sneddon's solution to interpret the LF-DAS response are provided in Chapter 5.

4.3. Waterfall Plots

LF-DAS data is typically visualized in waterfall plots of strain and strain rate as function of time and depth. Such plots derived from experimentally measured strains are shown in Figure 4.13. These plots were constructed by using Matlab to import a table consisting of the FBG measured strains for the duration of an experiment and plotting the table using the "surf" function. The y axis is specified as the z coordinates corresponding to each FBG (see Table 4.1 for example), and the time axis is normalized to the beginning

of injection. Extension (positive) is warm colored and compression (negative) is cool colored. To better visualize the transition from positive to negative values, a pseudo log transformation is applied to the measured strains as follows:

$$\varepsilon' = \begin{cases} \log_{10}\varepsilon & for \quad \varepsilon > \varepsilon_c \\ 0 & for \quad -\varepsilon_c \leq \varepsilon \leq \varepsilon_c \\ -\log_{10}|\varepsilon| & for \quad \varepsilon < -\varepsilon_c \end{cases} \tag{4.3}$$

Here, ε is the experimentally measured strain in units of microstrain, ε' is the transformed strain, and ε_c is a cutoff strain set at 10 microstrains, near the noise threshold of the strain measurements. The same transformation is applied to visualize strain rates with the cutoff strain rate set at 1 microstrain/sec.

The characteristic signature of a wide region of extension (yellow) surrounded by compression (blue) that converges to the location where the fracture intersects the sensor is visible between 100 – 140 seconds on the strain rate waterfall plot. The moment when the strain rate waterfall plot exhibits this convergence occurs prior to the actual fracture intersection time (indicated by a red vertical bar at 156 seconds). This is due to spatial resolution and the discrete nature of the experimentally measured strains compared to LF-DAS, which is a true distributed sensor. As the next set of figures show, increasing the spatial resolution of the strain sensors causes the convergence of positive strain rate to approach the timing of the fracture intersection.

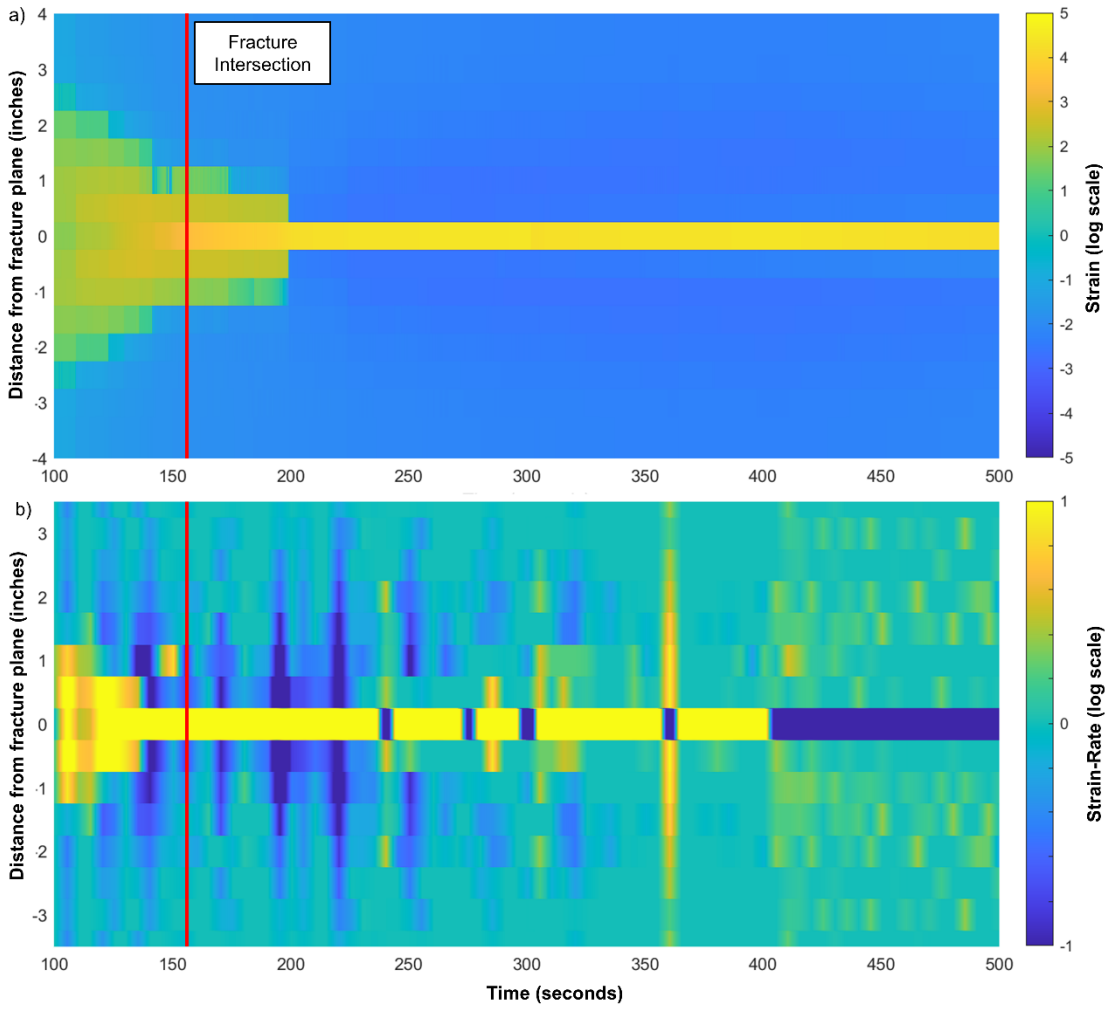

Figure 4.13 Strain (a) and strain rate (b) waterfall plots from a fracture experiment. The vertical line near 155 seconds denotes the time when the fracture intersected the embedded fiber.

To study the effect of spatial resolution on the strain rate waterfall plots, multiple tests were performed with various spacings of the FBG sensors. This would correspond to improving the spatial sampling resolution of LF-DAS measurements. Figure 4.14a

through Figure 4.14c present heat maps from three separate experiments with increasing spatial resolution. These are like LF-DAS waterfall plots with the exception that the time axis is replaced by R_D, the dimensionless crack radius measured in the experiment. The dashed red lines denote the dimensionless fracture radius at the moment of positive strain rate convergence. The solid red lines denote a dimensionless fracture radius of unity, indicating the fracture has intersected the fiber. As the spatial resolution increases, the collapse of the yellow pattern approaches a dimensionless radius of one, indicating intersection occurring. The dependence on the spatial resolution of the strain sensors can be modeled using Sneddon's solution (Equation 4.2). Modeled heat maps corresponding to the measured heat maps at the same spatial resolution are provided in Figure 4.14d through Figure 4.14f. The general trend of the yellow pattern converging towards one agrees with the measured results. This indicates that poor spatial resolution of strain rate sensors installed in the field could adversely impact the accuracy of determining the timing of a frac hit event from patterns on strain rate waterfall plots.

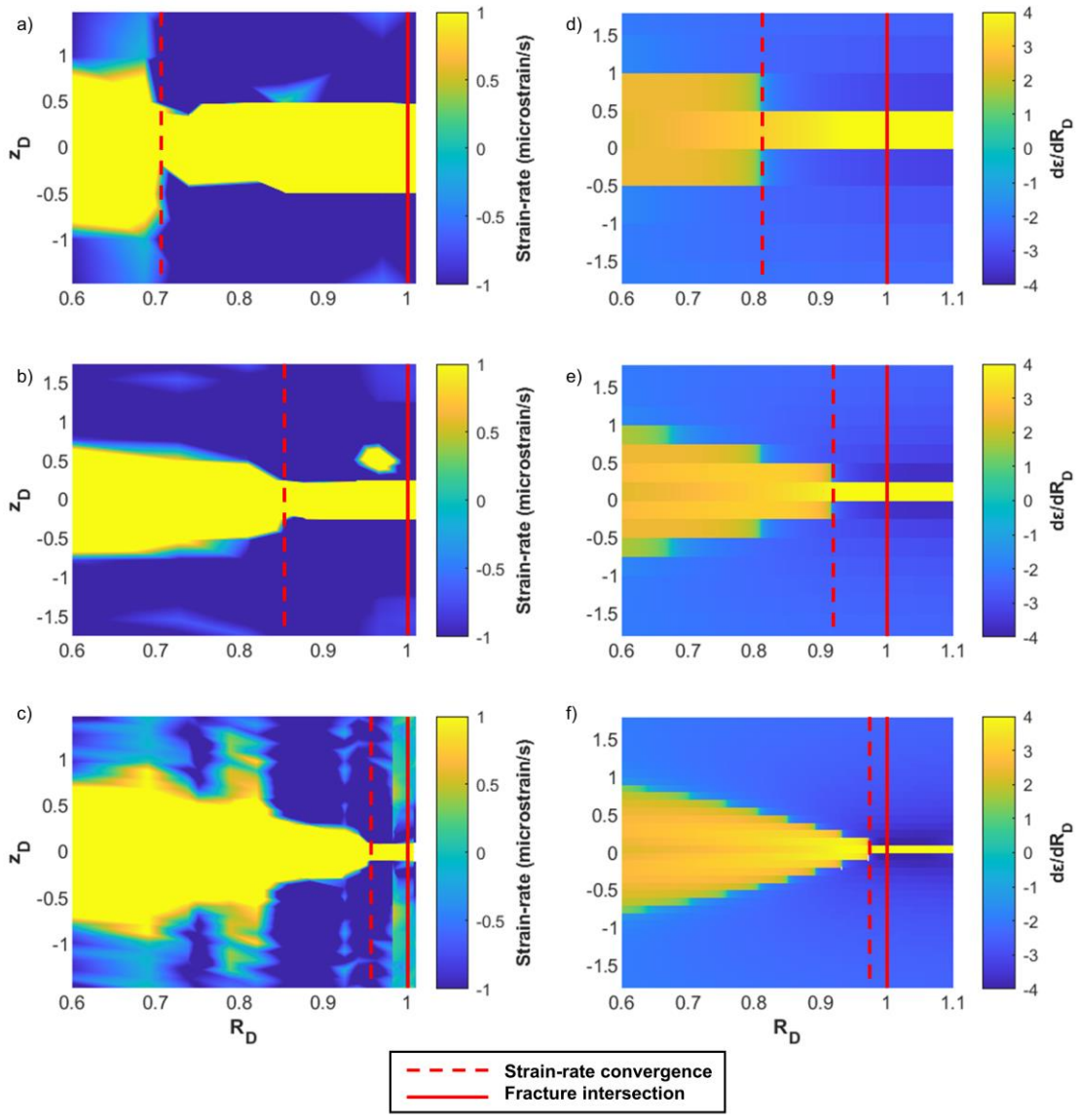

Figure 4.14 Strain rate waterfall plots from experiments (left column) and model predicted (right column) with dimensionless spatial resolution of a) and d) 0.5, b) and e) 0.25, and c) and f) 0.1.

4.4. Results from Experiments with Eccentric Fracture Propagation

In a few of the experiments, slight eccentricity in the fracture propagation led the fracture to intersect only one of the fibers. This provided an opportunity to examine the differences in the strain rate response between a frac hit and non-frac hit fiber. Figure 4.15 displays images from such an experiment.

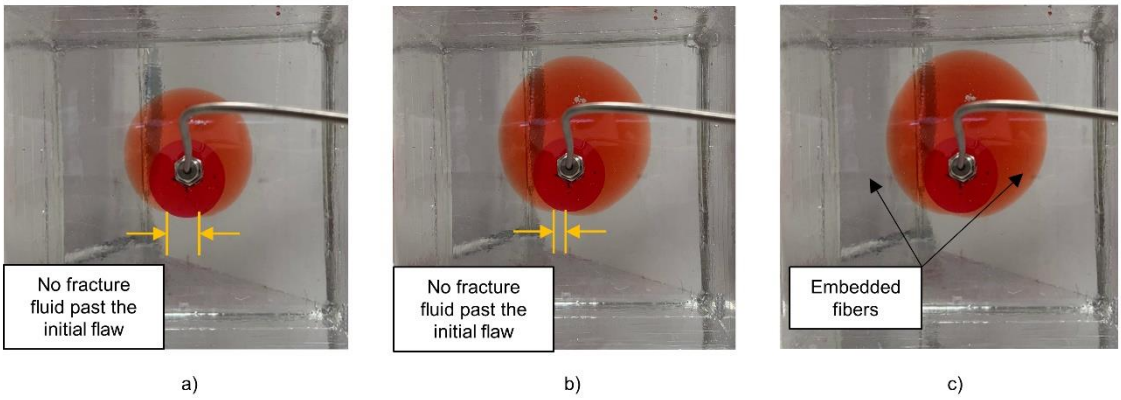

Figure 4.15 Photos from an experiment with eccentric fracture propagation.

The cause of eccentric fracture growth is attributed to inhomogeneities on the edge of the initial flaw that cause the fracture to preferentially propagate in one direction. In Figure 4.15a, fracture fluid has penetrated beyond all portions of the initial flaw except for the lower part. The barrier to downward propagation persists as the fracture grows to

the size shown in Figure 4.15b. This behavior, where the fracture delays propagating past part of the initial flaw, was observed in multiple experiments. Eventually, the fracture spreads beyond the initial flaw as shown in Figure 4.15c, at which point only one of the fibers is intersected.

Strain rate heat maps from an experiment with eccentric crack growth are exhibited in Figure 4.16. Both plots have the same dimensionless axis and color scale. The plot on the left is the response from a fiber intersected by a fracture, the plot on the right is from a fiber that did not experience a frac hit. The extending and compressing responses of the frac hit fiber are stronger than the non-frac hit fiber. In addition, the non-frac hit fiber does not exhibit a narrow region of extending fiber surrounded by intense compressing fiber, the characteristic pattern indicative of a fracture intersection.

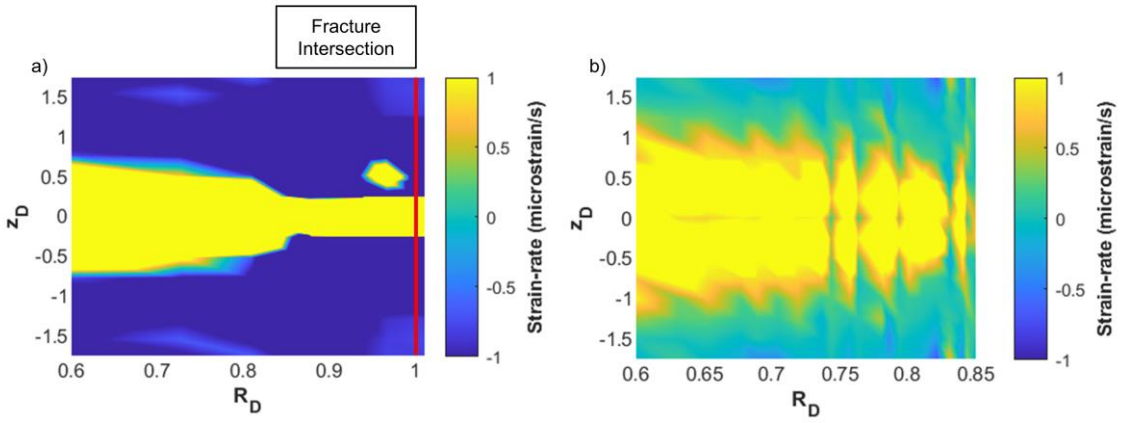

Figure 4.16 Comparison of the strain rate response between two fibers in the same experiment, one frac hit a), the other not hit b).

4.5. Debonding

In the experiments, the fiber decoupled from the epoxy near the plane of the fracture. Out of all the fibers intersected by fractures throughout the experiments, not one broke or split apart. In each case, the optical interrogator successfully sampled the strains on the FBGs after a fiber was intersected. At a minimum, the fracture debonds over a length equal to the fracture width, otherwise the fiber would break. Figure 4.17 displays the reflected spectral intensity from a FBG sensor near the fracture plane prior to and after debonding. The degradation of the single peak at the Bragg wavelength into two smaller, separate peaks indicates that different regions of the sensor are experiencing significantly different strains. The nearest edge of this FBG was 0.1 inches away from the plane of the fracture, significantly greater than the estimated fracture width at the fiber.

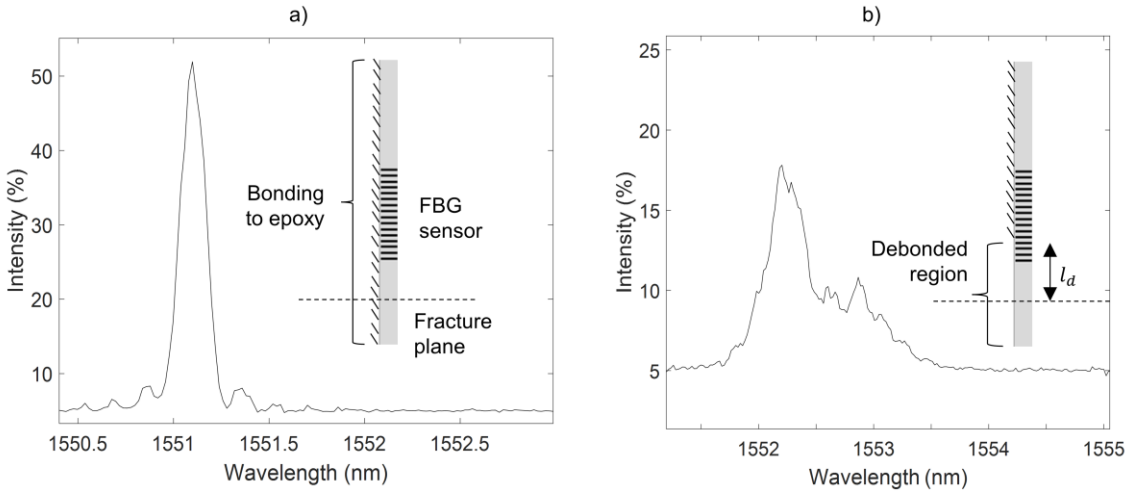

Figure 4.17 The spectral intensity of reflected light for a FBG sensor near the fracture plane a) prior to debonding a) and b) after debonding.

In essence, debonding reduces the spatial resolution of the strain measurements which can affect the strain rate pattern. This phenomenon can be modeled by defining a debonding length, l_d, over which the fiber is no longer coupled to the formation. If $|z| > l_d$, the displacement and strain can be computed from Equations 2.46 and 2.50. For portions of the fiber within the debonding region, $|z| \leq l_d$

$$\varepsilon_d = \frac{u_z(l_d)}{l_d} \tag{4.4}$$

$$u_z = \varepsilon_d z \tag{4.5}$$

where u_z is the displacement along the fiber, and ε_d is the strain over the debonded length of the fiber.

This debonding model was applied to study the effect of debonding between the cement, casing, fiber system and the formation. Figure 4.18 juxtaposes three separate modeled strain rate heat maps with dimensionless radius on the x axis. Each plot refers to a gauge length L_g or debonding length l_d normalized by the crack radius R. The first two plots exhibit the modeled response of a fiber fully coupled to the formation. Figure 4.18a has a relatively small gauge length compared to Figure 4.18b, but both plots show convergence of the extending portion of the strain rate signal at the time of the fracture intersection. The final plot exhibits the strain rate response with debonding considered on either side of the fracture over a dimensionless length of 0.1. The loss of spatial resolution causes the strain rate convergence to occur at a dimensionless radius of 0.96. In terms of a field example, if a horizontal treatment and monitor well at the same true vertical depth are offset laterally 500 feet, a dimensionless debonding length of 0.1 corresponds to 50 feet of debonding between the fiber, casing, cement system on either side of the fracture. According to the proposed model, the strain rate convergence would occur when the fracture is 20 feet away from the monitor well, a 4% error. The error increases with the debonded length. The significance of this result is that debonding essentially reduces the spatial resolution which can lead to early interpretations of the timing of a frac hit event.

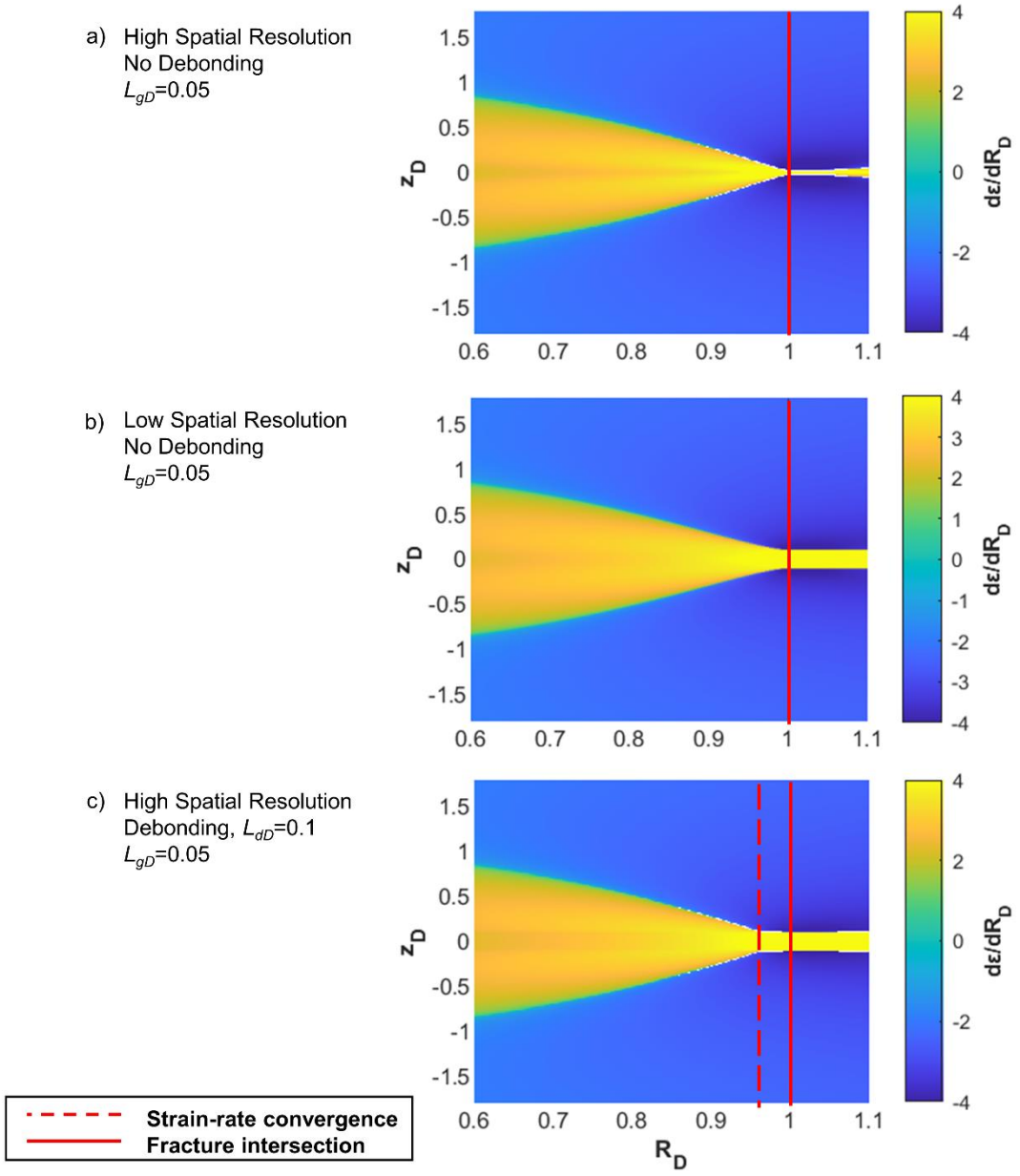

Figure 4.18 Modeling the strain rate response comparing cases with perfect coupling and a a) small and b) large gauge length versus a c) a debonded case with a small gauge length.

Debonding also explains some features observed on the experimental strain rate waterfall plots. Figure 4.19 compares the strain rate waterfall plot from one of the experiments to the measured fracture geometry, pressure, and strain at the center location, $z = 0$. The time the fracture intersected the fiber is denoted by the vertical red line just after 150 seconds. As the fracture continued to propagate, the FBG intersected by the fracture exhibited pulses of negative strain rate. These pulses are outlined in black rectangles. The first type of pulses corresponds to a fracture growth event with a sharp decrease in measured fracture pressure. This type of pulse is marked by strain sensors on either side of the fracture plane synchronously exhibiting a yellow or extending pulse. The second type of blue pulse does not correspond to a pressure drop, and the strain sensors around it do not exhibit notable changes. These pulses are caused by debonding of the fiber-epoxy interface. From Equation 4.4, an increase in the debonded length causes a decrease in the strain. The negative strain rate pulses within the rectangles labeled “2” correspond to debonding events that affect the strain around the fracture plane. Such pulses have been noted in LF-DAS responses in the field and may reflect debonding of the fiber-casing-cement-formation system (Ugueto et al. 2019).

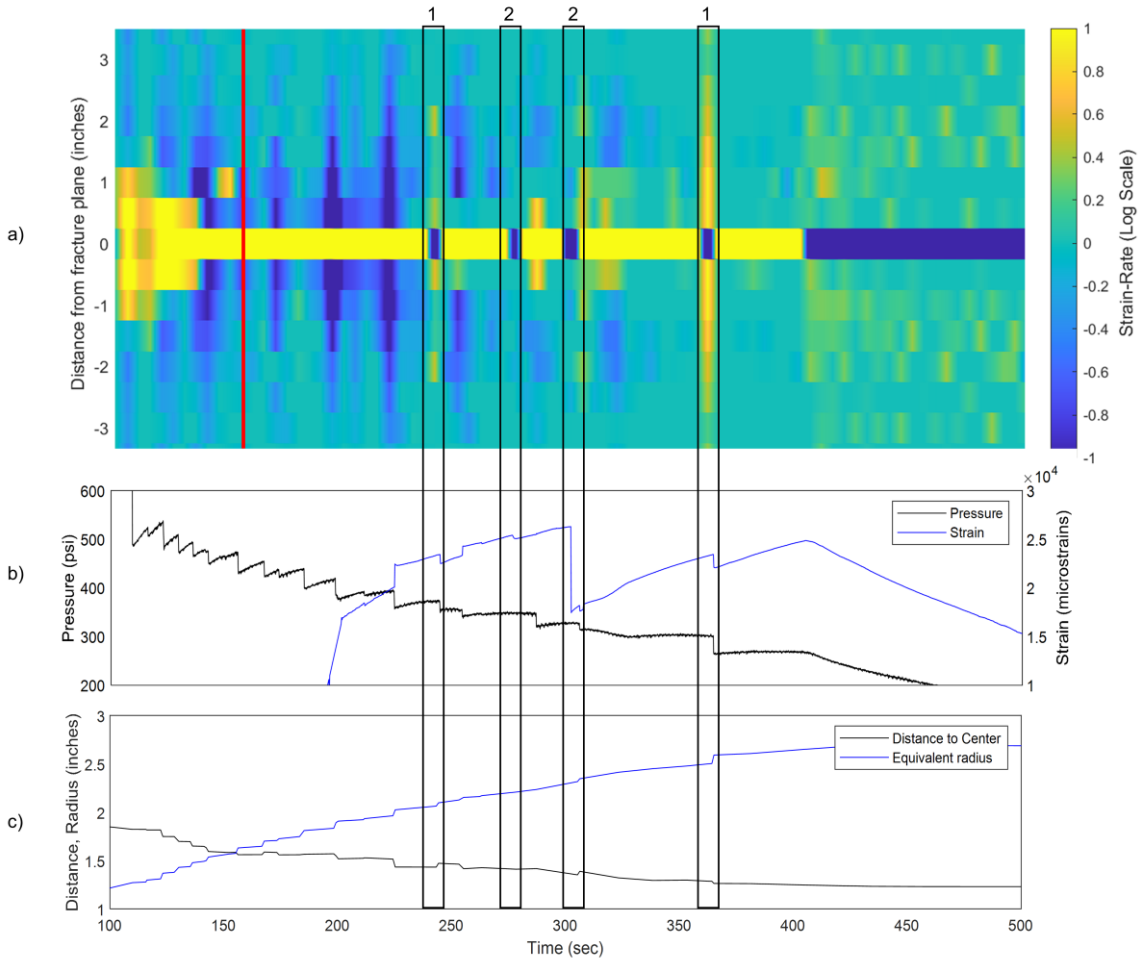

Figure 4.19 Strain rate waterfall plot a) plotted synchronously with the pressure and strain at z = 0 b) as well as the fracture geometry c).

5. ZERO STRAIN AND ZERO STRAIN RATE LOCATION METHODS*

Information about the geometry of propagating hydraulic fractures from the measured strain data is useful for characterizing unconventional completions. The “cone shape” of the tensile portion of LF-DAS strain and strain rate waterfall plots has been well documented in field observations and modeling. Since this feature is often readily distinguishable, a straightforward model is developed to estimate the fracture front location from the transition from positive to negative strain. The “zero strain location method” and “zero strain rate location method” for fracture front estimation are introduced, validated experimentally, and applied to a field case.

Figure 5.1 illustrates a treatment well and a monitor well instrumented with fiber optic cable. Using LF-DAS measurements, the nearest distance from the fiber to the front of a propagating fracture can be estimated using these methods. The z coordinate illustrated in this figure is zero at the plane of the fracture and increases away from the fracture. It is the z coordinate where the strain or strain rate is zero that is utilized in these methods to estimate fracture geometry.

* Part of this section is reproduced with permission from “Experimental Investigation of Low-Frequency Distributed Acoustic Strain-Rate Responses to Propagating Fractures” by Leggett, S., Reid, T., Zhu, D., and Hill, A.D. 2021. SPE-209135-MS. Copyright 2021, Society of Petroleum Engineers. Further reproduction prohibited without permission.

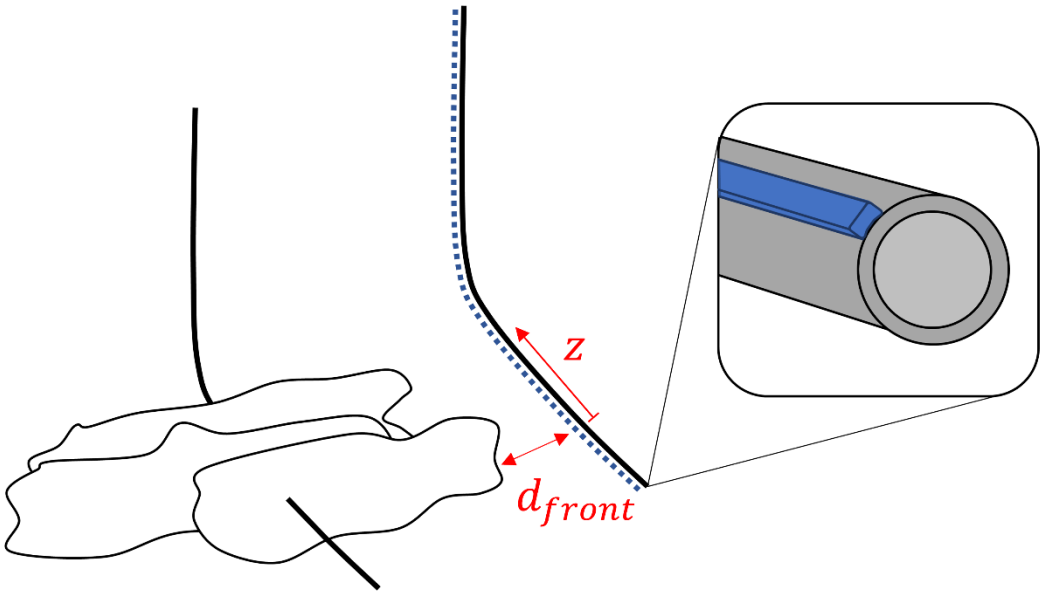

Figure 5.1 Schematic representation of LF-DAS sensing. The zero strain and zero strain rate location methods estimate the distance to the fracture front based on the z coordinate of zero strain.

5.1. Zero Strain Location Method

For a radial fracture, there is a one-to-one correspondence between the location on the fiber where the axial strain is zero ($\varepsilon = 0$) considering a fiber normal to the plane containing the fracture. Using Equation 4.2, one can solve for the *z* coordinate where the strain is zero (zero strain location). The zero strain location depends on the fracture radius, the observation well vertical and horizontal offset from the treatment well, and a representative Poisson's ratio for the formation. Notably, the location of zero strain is

independent of Young's modulus and the fracture net pressure. It is not required to transform the measured cumulative LF-DAS optical phase shift to units of strain when using this method. Because the phase shift is proportional to strain rate, a zero strain corresponds to a zero cumulative phase shift. A domain to illustrate the zero strain location method is shown in Figure 5.2. As a fracture emanates from a treatment well towards a fiber-instrumented monitor well, there is z coordinate z_n where the strain is zero corresponding to each time t_n. Each time corresponds to a separate fracture geometry, and it is assumed that the fracture front can be approximated as an arc with radius R. The location of zero strain at each time step corresponds to the boundary of the yellow and blue sections of the waterfall plot.

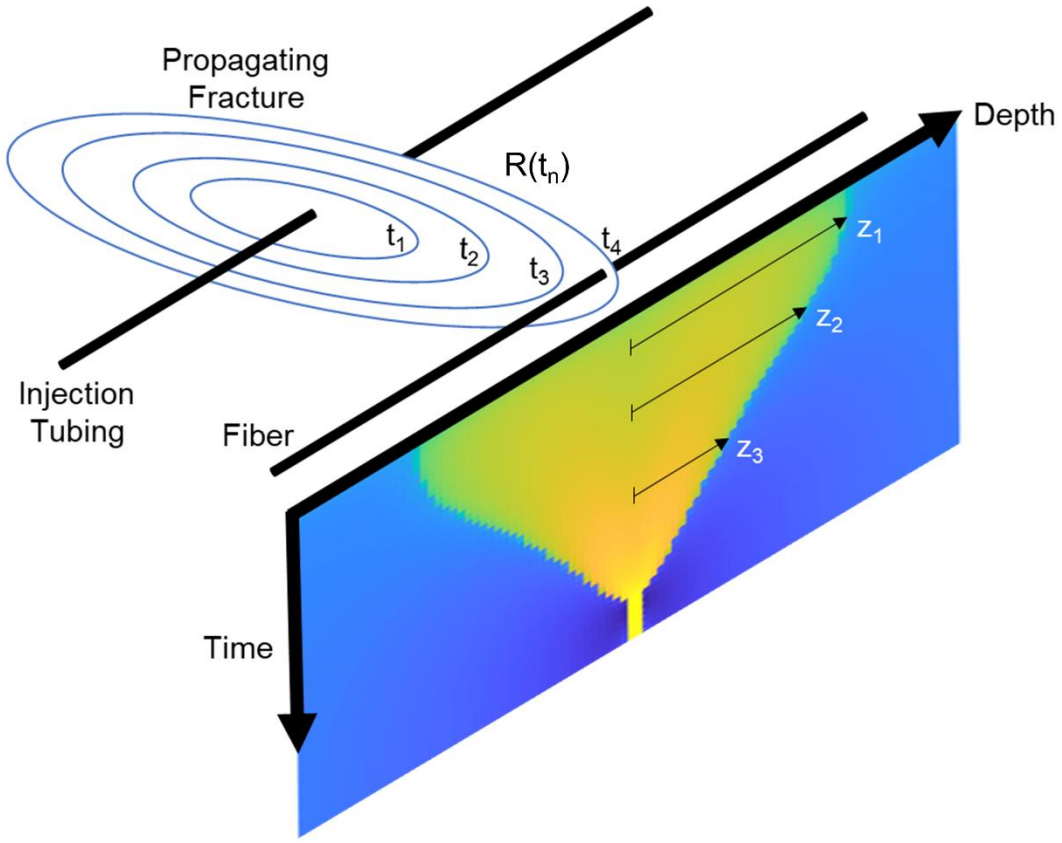

Figure 5.2 Schematic illustration of the correspondence of a zero strain location to fracture geometry.

Figure 5.3 was obtained by the following steps. A detailed code is provided in Appendix A.

1. A Matlab program was created to evaluate Equation 4.2. The code solves for strain as a function of the *z* coordinate, Poisson's ratio *v*, and crack radius *R*, with other parameters (such as radial well spacing, *r*) specified as constants.

2. For a given Poisson's ratio and crack radius, the function was used to compute the strain for a range of *z* coordinates.
3. The *z* coordinate corresponding to the minimum absolute value of strain was identified. Interpolation was then applied to determine the zero strain location for the given crack radius.
4. Steps 2 – 3 were repeated for varying crack radii and Poisson's ratios to create lists of corresponding zero strain locations and crack radii for a given Poisson's ratio.
5. The z coordinates of zero strain and corresponding crack radii were non-dimensionalized by dividing by the radial well spacing, *r*. Curves of dimensionless radius R_D as a function of dimensionless zero strain location z_{0D} were plotted for various Poisson's ratios.

The "cone-shaped" pattern is reflected in the shape of the resulting curve. When the fracture is small, $R_D \leq \sim 0.5$, small changes in the zero strain location correspond to large changes in fracture radius. For $R_D > \sim 0.5$, the zero strain location decreases relatively rapidly as the half-length increases. Thus, the stability of the estimate increases with R_D, or decreasing distance to the fracture front d_f.

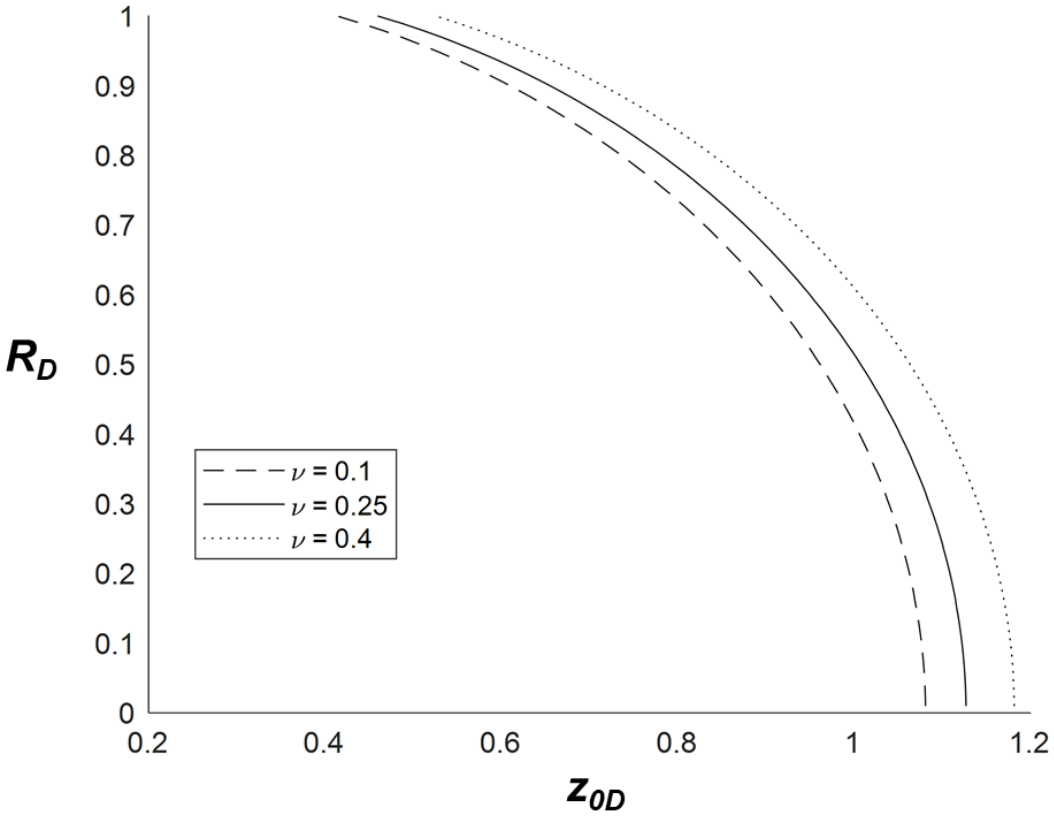

Figure 5.3 Dimensionless fracture radius versus dimensionless zero strain location for various values of Poisson's ratio.

To avoid solving the infinite integral in Equation 4.2, a series of parabolic curve fits were created. The fracture radius as a function of the zero strain location can be approximated by:

$$R_D = \frac{-b - \sqrt{b^2 - 4a(c - z_{0D})}}{2a} \qquad 5.1$$

where z_{0D} is the dimensionless zero strain location. The coefficients in Equation 5.1, *a*, *b*, and *c*, are functions of Poisson's ratio, *v*, and can be calculated as shown in Table 5.1.

Table 5.1 Zero strain location method curve fit coefficients.

	$z_{0D} > 1$	$0.75 \leq z_{0D} \leq 1$	$z_{0D} < 0.75$
a	$-0.141\nu - 0.473$	$-1.23\nu - 0.702$	$-4.06\nu - 3.01$
b	$0.0707\nu + 0.00106$	$1.72\nu + 0.142$	$7.82\nu + 3.73$
c	$0.331\nu + 1.05$	$-0.246\nu + 1.04$	$-3.39\nu - 0.348$

A coordinate transformation is required to convert the observed measured depths of zero strain from LF-DAS data to a *z* coordinate. This transformation is accomplished by:

$$z_{0D} = \frac{|D_0(t) - D_{hit}|}{\sqrt{\Delta l^2 + \Delta h^2}} \tag{5.2}$$

$D_0(t)$ is the measured depth along the fiber where the integrated LF-DAS phase shift is zero. This corresponds to the locations where the strain waterfall plot transitions from yellow to blue. D_{hit} is the measured depth where the fracture intersects the fiber, which corresponds to the center of the cone-shaped region of extension. Normalization is performed by the radial well spacing which depends on the lateral and vertical well spacing Δl and Δh. The curve fit is at least 10% accurate for $R_D \geq 0.25$. The accuracy generally increases with fracture radius. Alternatively, one can use Equation 4.2 to construct a curve as in Figure 5.3.

Finally, the nearest distance from the fracture front to the fiber, d_f, can be computed by:

$$d_f = \sqrt{\Delta l^2 + \Delta h^2}(1 - R_D) \tag{5.3}$$

5.1.1. Example Illustrating the Zero Strain Location Method

Consider the following example using the zero strain location method. A horizontal monitor well instrumented with fiber optic cable is located 1,000 feet laterally offset from a treatment well at the same true vertical depth. A Poisson's ratio of 0.2 is typical for the targeted formation. From the waterfall plot, the measured depths where the strain was zero were observed as in the following table. The measured depth along the fiber that the frac hit was observed was 10,000 feet.

Table 5.2 Zero strain location method example.

Time (minutes)	Measured depth of zero strain, D_0 (feet)
15	11,000
25	10,910
35	10,770
45	10,660
55	10,590

Broken out into a series of steps, the zero strain location method can be summarized as follows:

1. Identify the necessary input parameters: Poisson's ratio, v, and the radial offset between the treatment and fiber-instrumented well. The radial offset r is computed by Equation 5.4. Δl is the lateral offset and Δh is the vertical offset. In the example, there is no offset in true vertical depth of the horizontal well, so the radial well spacing is 1,000 feet.

$$r = \sqrt{\Delta l^2 + \Delta h^2} \quad 5.4$$

2. Identify the location of the fracture hit, D_{hit}. This corresponds to the middle of the converging pattern in LF-DAS strain rate responses, and 10,000 feet in the example.
3. At each time step during the fracture treatment, identify the location of zero strain, $D_0(t)$. This is done by marking the boundary between positive and negative LF-DAS strain responses on waterfall plots. Table 5.2 provides the locations for the example.
4. Use Equation 5.2 to compute the dimensionless *z* coordinates of zero strain. Table 5.3 shows the results of applying the coordinate transformation in the example.

Table 5.3 Example dimensionless zero strain locations

Time (minutes)	Measured depth of zero strain, D_0 (feet)	Dimensionless zero strain locations z_{0D}
15	11,000	1
25	10,910	0.91
35	10,770	0.77
45	10,660	0.66
55	10,590	0.59

5. Compute the appropriate curve fit parameters, *a*, *b*, and *c* from the correlations provided in Table 5.1. The computed curve fit parameters for the example are provided in Table 5.4. Different coefficients are used for dimensionless zero strain locations less than 0.75 than those greater than 0.75 in accordance with the conditions specified in Table 5.1.
6. Calculate the dimensionless radius and location of the fracture front using Equations 5.1 and 5.3. The results are tabulated in Table 5.4 and graphed in Figure 5.4.

Table 5.4 Results of the zero strain location method example.

Dimensionless zero strain locations z_{0D}	*a*	*b*	*c*	R_D	d_f (feet)
1	-0.948	0.486	0.9908	0.493	507
0.91	-0.948	0.486	0.9908	0.645	355
0.77	-0.948	0.486	0.9908	0.803	197
0.66	-3.822	5.294	-1.026	0.889	111
0.59	-3.822	5.294	-1.026	0.931	69

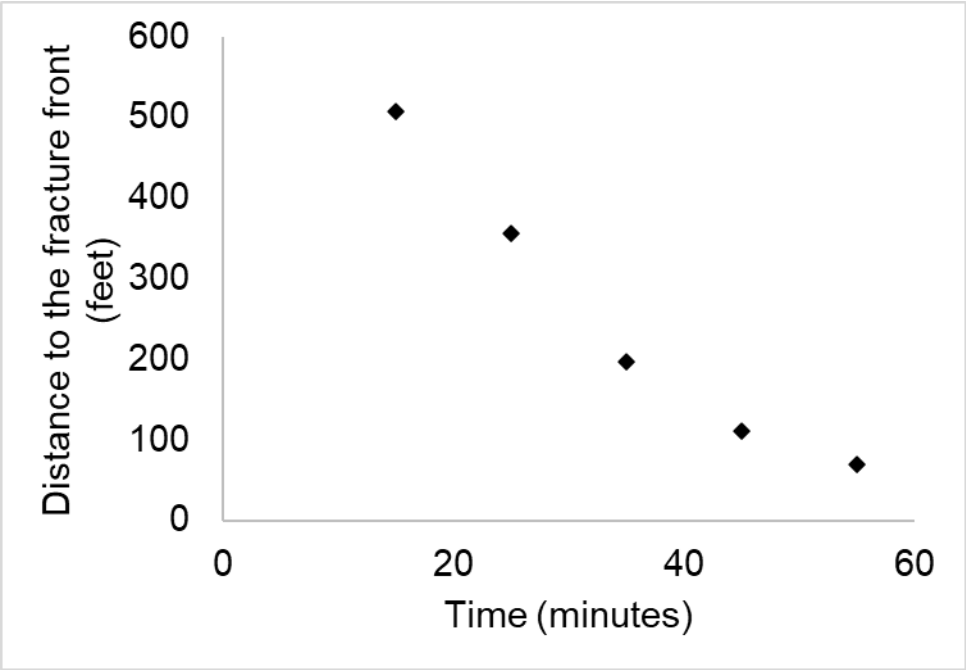

Figure 5.4 Nearest distance from the fiber to the fracture front for the example.

5.2. Experimental Validation

The experiments provide data that includes measured strains and known fracture geometries relative to the positions of the fiber optic cables. Thus, the experiments provided an opportunity to validate the zero strain location method. As shown in Figure 4.12, non-negligible boundary effects in the experiments caused variance between measured strains and modeled strains using Equation 4.2. On the other hand, the finite element model was able to accurately predict the measured strains. Therefore, as discussed in Section 4.2.2, a mapping factor of 0.8 was employed to convert a Sneddon zero strain location to a finite element zero strain location.

Radial fractures are not likely common in unconventional completions. To test the application of the zero strain location method to a non-ideal fracture geometry, results from an experiment with a non-radial, eccentric fracture were utilized. Figure 5.5 shows the fracture geometry at one point in time as the fracture propagated toward the embedded fiber beyond the initial flaw.

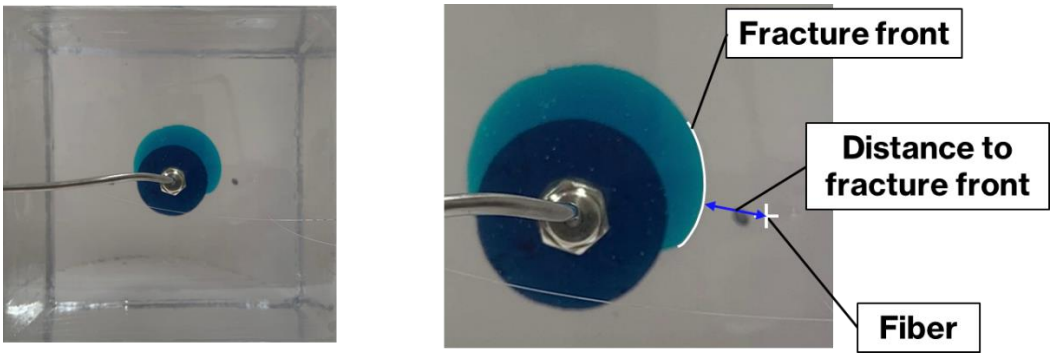

Figure 5.5 Eccentric fracture with non-radial geometry used to validate the zero strain location method

Applying the zero strain location method to the experimentally measured strains at each time step yields the following result in Figure 5.6. Apart from the time interval prior to 110 seconds, the estimated d_f from the interpolated zero strain locations agree with the measured d_f. The early times correspond to when the fracture is not propagating but pressuring up the region occupied by the 1-inch radius initial flaw. This radius

corresponds to a dimensionless fracture half-length of 0.5. The zero strain method appears to perform adequately for fracture radii greater than 0.5.

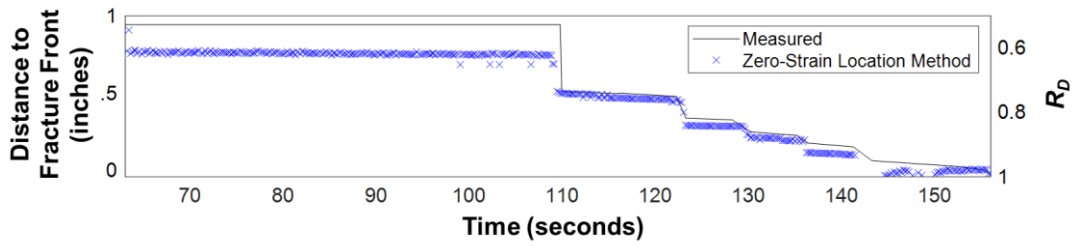

Figure 5.6 Measured and estimated fracture radius using the zero strain location method.

The zero strain location method can accurately estimate d_f, the shortest distance from the fiber to the fracture front, even for non-radial fracture geometries. The strain response on the fiber appears to be dominated by the portions of the fracture that are nearest the fiber. Therefore, LF-DAS strain monitoring provides information on how a fracture is approaching the monitoring well before a frac hit occurs. As the next section shows, the same information can be gathered from LF-DAS strain rate measurements as well.

5.3. Zero Strain Rate Location Method

Depending on the LF-DAS acquisition, the LF-DAS strain rate signal may provide a clearer response than the integrated LF-DAS strain. Therefore, it useful to have a method to extract information about the distance to the front from both strain and strain rate waterfall plots. The zero strain rate location method is developed similarly to the zero strain location method. Sneddon's model for strain due to a hydraulic fracture is static; there is no time component. Therefore, the following transformation is considered to predict the location on the fiber of zero strain rate for a propagating fracture.

$$\frac{d\varepsilon_z}{dt} = \frac{d\varepsilon_z}{dR}\frac{dR}{dt} = 0 \qquad 5.5$$

Here, ε_z is the strain normal to the fracture, R is crack radius, and t is time. As long as dR/dt is non-zero (i.e., the crack is propagating), then the strain rate at any time is proportional to the derivative of strain with respect to crack radius. With this consideration, the Equation 2.50 can be numerically differentiated with respect to crack radius to solve for the location of zero strain rate. Figure 5.7 exhibits the results of this computation for varying values of crack radius and Poisson's ratio. Independent of crack Poisson's ratio, the zero strain rate location converges to 0 when the fracture front reaches the fiber optic cable ($x_{fD} = 1$). In Figure 5.8, the zero strain and zero strain rate locations are compared. The location of zero strain rate is closer to the fracture face than the location of zero strain except for small values of dimensionless crack radius. For a dimensionless crack radius of 0.1 or less, the location of zero strain and zero strain rate are approximately the same.

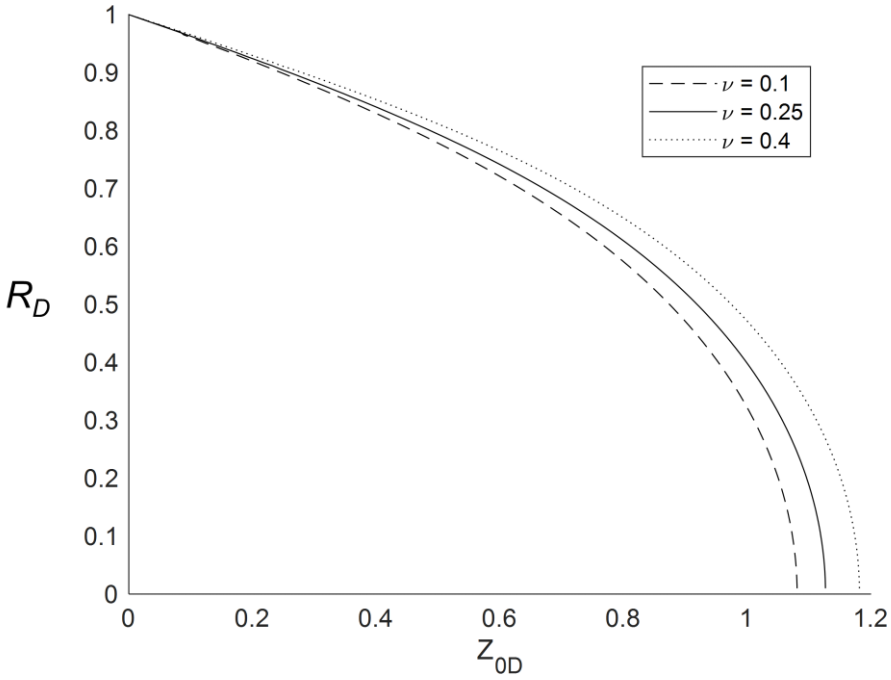

Figure 5.7 Dimensionless crack radius as a function of zero strain rate location for various values for Poisson's ratio.

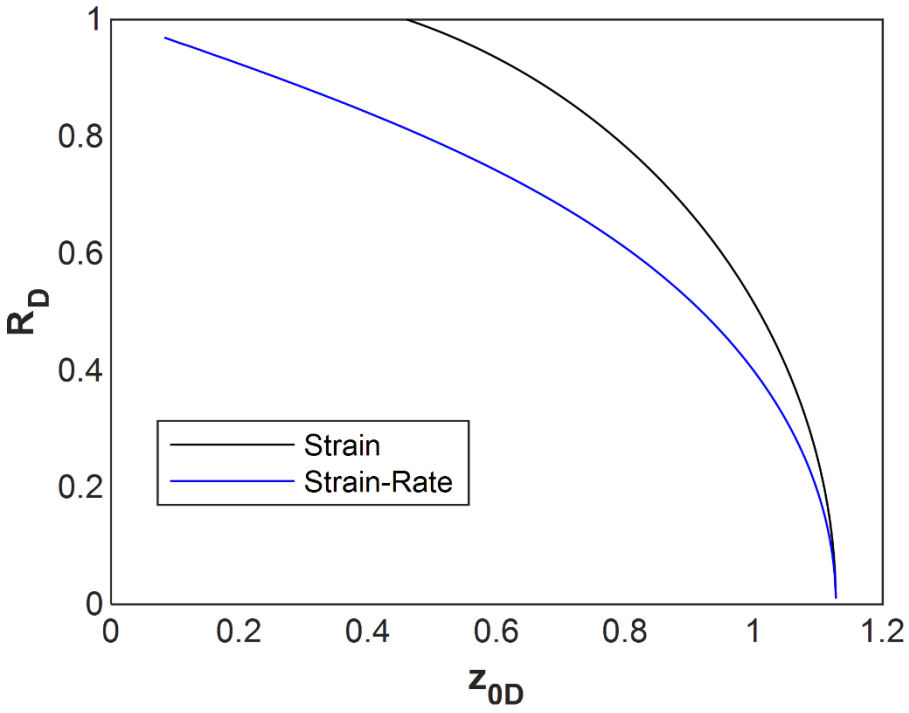

Figure 5.8 Comparison of the zero strain and zero strain rate locations.

A series of parabolic curve fits was performed akin to the curve fits performed in the zero strain location method. Table 5.5 provides the curve fit coefficients as a function of Poisson's ratio. The location of the fracture front as a function of the zero strain rate location can be approximated by inserting these coefficients in Equation 5.1. As with the zero strain location method, the curve fit is at least 10% accurate for $R_D \geq 0.25$.

Table 5.5 Zero strain rate location method curve fit coefficients.

	$z_{0D} > 1$	$0.75 \leq z_{0D} \leq 1$	$z_{0D} < 0.75$
a	-0.255*v* + -0.789	-1.83*v* + -1.02	-1.56*v* + -1.72
b	0.0952*v* + 0.00202	1.86*v* + 0.0793	1.64*v* + 0.914
c	0.33*v* + 1.05	-0.136*v* + 1.05	-0.0891*v* + 0.805

5.4. Application of the Zero Strain and Zero Strain Rate Location Methods to a Field Case

As an example of the utility of the zero strain location and zero strain rate location method, the approach was applied to LF-DAS data acquired from an unconventional field. In this case, the difference in true vertical depth between the horizontal monitor well and horizontal treatment well, Δh, was 243 feet. The lateral offset, Δl, was 411 feet. A Poisson's ratio of 0.25 was selected based on available data. Figure 5.9 presents the strain rate and strain waterfall plots. From the waterfall plot, at least two frac hits are evident that occur at approximately the same time, near X300 and X400 feet. As the analysis assumes a single propagating fracture, the fracture nearest to the visible zero strain locations (yellow/blue border) is selected for analysis. D_{hit}, the measured depth of the hit, X300 feet, is recorded for use in Equation 5.2.

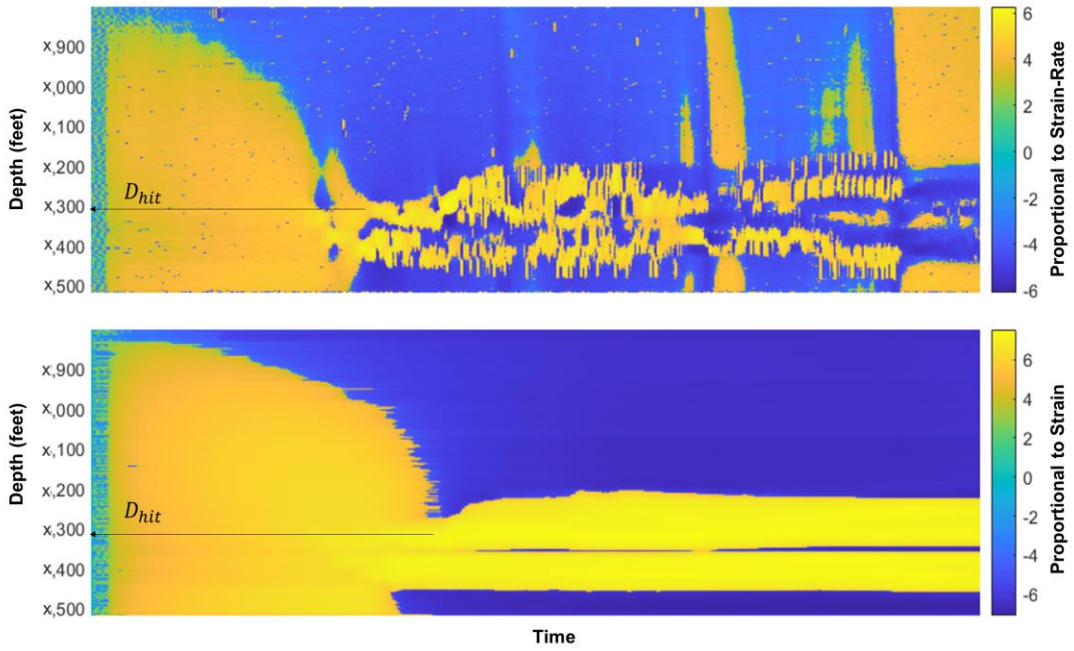

Figure 5.9 Low frequency DAS strain rate (top) and strain (bottom) waterfall plots, with the fracture hit location D_{hit} marked.

The next step is to determine the measured depths of zero strain and zero strain rate, $D_0(t)$, at each time increment from the strain waterfall plot. This can be done by tracing a line over the transition from yellow to blue on the waterfall plot using a graphical user interface such as WebPlotDigitizer (Rohatgi 2021), or by writing a program to interpolate the LF-DAS phase shift for the zero location. Results from the latter approach are exhibited in Figure 5.10, with both the zero strain and zero strain rate locations displayed as a function of time. As a derivative measurement, the zero strain rate location signal contains more noise than the zero strain location. This is especially true at early times when the fracture front is far from the fiber optic cable.

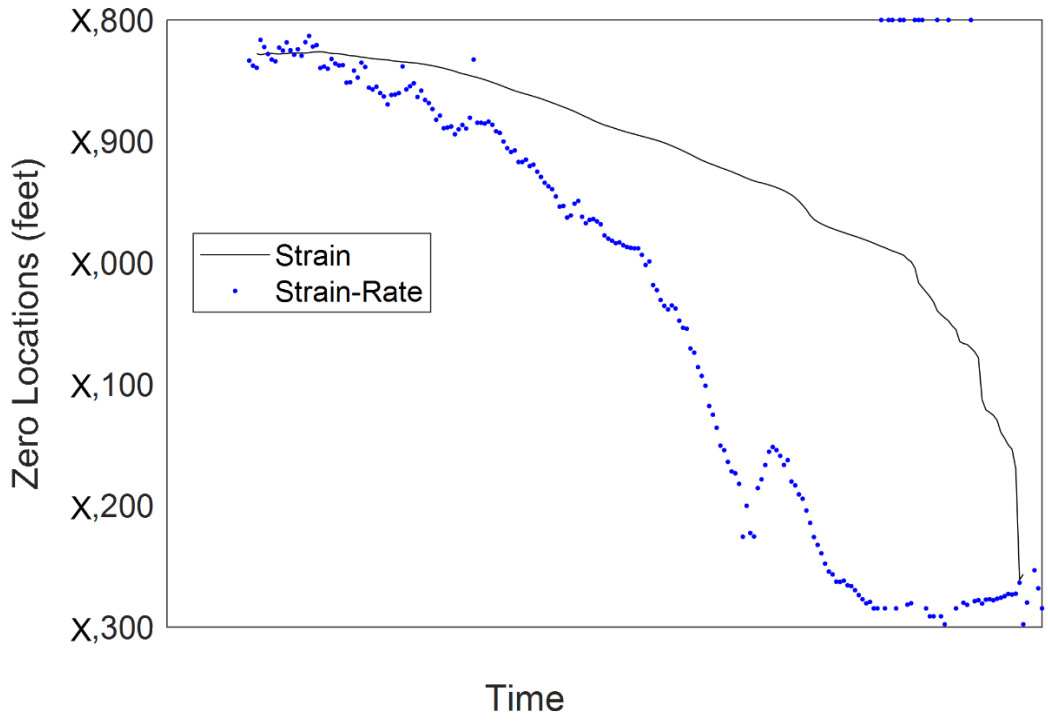

Figure 5.10 Measured depth of zero strain, D_0, extracted from the strain and strain rate waterfall plots.

After determining the zero strain and zero strain rate locations, the next step is to non-dimensionalize the zero strain and zero strain rate locations by Equation 5.2. The dimensionless zero strain and zero strain rate locations can then be used in Equation 5.1 to compute the dimensionless fracture radius utilizing the curve fit coefficients from Table 5.1 for strain and Table 5.5 for strain rate. Then, one can estimate the distance to the fracture front via Equation 5.3.

The estimated dimensionless locations of the fracture front as estimated by the zero strain and zero strain rate location methods are plotted in Figure 5.11. For $R_D > 0.5$, the estimates of the distance to the fracture front from the zero strain and zero strain rate location methods agree within approximately 10%. The noise in the estimated zero strain rate locations at early times propagates to the estimated fracture front location. The estimated decrease in fracture radius at early times for the zero strain location method is unrealistic. The same comment applies for the zero strain rate location method when the dimensionless fracture front location is near 0.9. The zero strain location method exhibits weakness for $R_D \leq \sim 0.5$ in the field application just as observed when interpreting the strains from the experimental validation. Interestingly, the estimated fracture growth rate from both methods is nearly constant.

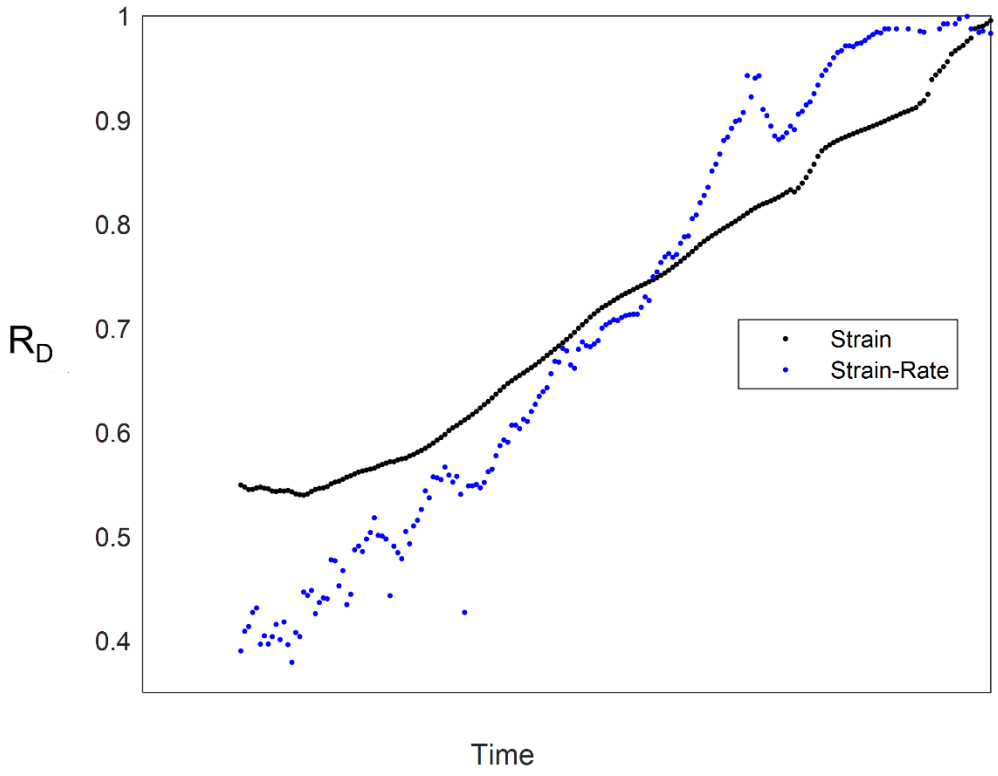

Figure 5.11 Estimated fracture front location from the zero strain and zero strain rate location methods.

The estimated distance to the fracture front was computed using both Sneddon's solution (Equation 4.2) and the curve fits for the zero strain and zero strain rate location methods and compared (Equation 5.1). The results are displayed in Figure 5.12. The curve fits agree well with the full analytical solution in this case with negligible differences especially for large dimensionless fracture radii.

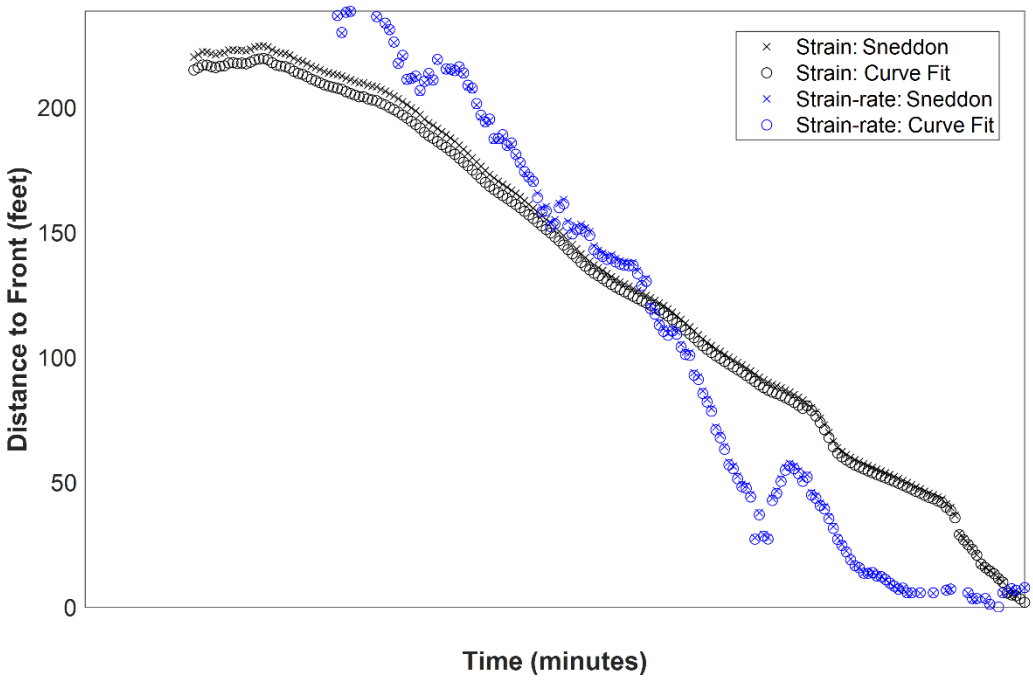

Figure 5.12 Comparison of the zero strain location method curve fit and full analytical solution to estimate dimensionless fracture half-length vs time.

A radial fracture model cannot adequately describe fractures generated during multi-cluster unconventional completions. However, the experimental results indicate that the fibers respond strongly to the portions of the fracture nearest to the monitor well. Using the developed methods, the front of the fracture that is closest to the monitoring well can be tracked, which provides information to characterize fracture propagation.

6. NUMERICAL STUDY OF THERMAL EFFECTS ON LOW-FREQUENCY DISTRIUBTED ACOUSTIC SENSORS*

Chapter 6 pivots to numerical simulation of the LF-DAS response to account for thermal effects. When a fracture emanates from a treatment well and intersects a fiber-instrumented monitor well, fracture fluid injected at ambient temperatures can cool a section of the sensing fiber. As discussed in the Chapter 1, temperature changes alter the LF-DAS response. The increasing use of LF-DAS for characterizing unconventional hydraulic fracture completions demands an investigation of the effects of temperature on the measured strain response by LF-DAS.

6.1. LF-DAS Mathematical Model with Thermal Effects

Jin et al. posited a linear relationship between the LF-DAS signal and temperature (Jin et al. 2019). In doing so, they successfully reproduced the temperature signal from an independent sensor in the borehole using LF-DAS based temperature measurements. The assumption that the optical phase shift behaves linearly with temperature enables expressing a relationship that includes strain and temperature effects on the LF-DAS signal.

Studying thermal effects on LF-DAS sensors requires a mathematical model that relates temperature and strain change to the LF-DAS optical phase shift. Equation 1.2 is repeated here and provides the basis for deriving such an expression.

---

* Part of this section is reproduced with permission from "Thermal Effects on Far-field Distributed Acoustic Strain-rate Sensors" by Leggett, S., Zhu, D., and Hill, A.D. 2021. *SPE J*. SPE-205178-PA. doi: 10.2118/205178-PA. Copyright 2021, Society of Petroleum Engineers. Further reproduction prohibited without permission.

$$\varphi = \frac{2\pi nl}{\lambda} \tag{6.1}$$

Here, φ is the optical phase shift, n is the index of refraction of the fiber optic cable's core, λ is the wavelength of the light pulse, and l is the representative path the light travels. Differentiating Equation 6.1 with respect to time yields:

$$\frac{d\phi}{dt} = \frac{2\pi nl}{\lambda}\left(\frac{1}{l}\frac{dl}{dt} + \frac{1}{n}\frac{dn}{dt} - \frac{1}{\lambda}\frac{d\lambda}{dt}\right) \tag{6.2}$$

Assuming a stable laser source, the term $d\lambda/dt$ can be neglected. For optical phase measurements, the representative distance that the light pulse travels is twice the gauge length, L_g, on an unstrained fiber. Deformation leads to minute changes in the distance traversed by the laser beam. This deformation divided by the gauge length yields the average strain over the gauge length of the fiber. Furthermore, the index of refraction of the fiber is sensitive to both axial strain, ε, and temperature, T. These considerations yield:

$$\frac{d\phi}{dt} = \frac{4\pi nL_g}{\lambda}\left(\frac{d\varepsilon}{dt} + \frac{1}{n}\frac{\partial n}{\partial T}\frac{dT}{dt} + \frac{1}{n}\frac{\partial n}{\partial \varepsilon}\frac{d\varepsilon}{dt}\right) \tag{6.3}$$

The terms $\partial n/\partial T$ and $\partial n/\partial \varepsilon$ are constants known as the thermo-optic coefficient, ζ_T and strain-optic coefficient, ζ_ε respectively. The total strain, ε, consists of mechanical strain, ε_m, and thermal strain, the product $\alpha * dT$, where α represents the effective thermal expansion coefficient of the fiber, casing, cement, and formation system.

$$\frac{d\varepsilon}{dt} = \frac{d\varepsilon_m}{dt} + \alpha\frac{dT}{dt} \tag{6.4}$$

The following table provides ranges of measured values for the thermo-optic coefficient, strain-optic coefficient, and thermal expansion coefficient in glass optical fibers. Typical

values for the pulsed light wavelength, and the index of refraction of the fiber are also provided.

Table 6.1. Properties of silica based optical fibers.

Variable	Symbol	Value	Units	Reference
Thermo-optic coefficient	ζ_T	8.6 – 12 x 10^{-6}	1/℃	(Hisham, 2019; Carr, 1990)
Strain-optic coefficient	ζ_ε	-0.27	dimensionless	(Carr, 1990)
Thermal expansion coefficient	α	5-8 x 10^{-7}	1/℃	(Hisham, 2019; Carr, 1990)
Wavelength	λ	1550	nm	(Hartog, 2017)
Index of refraction	n	1.468	dimensionless	(Hartog, 2017)

The derivation can be reduced to a simple expression, where the change in optical phase is linearly dependent on both strain and temperature.

$$\Delta\phi = C_T\Delta\bar{T} + C_\varepsilon\Delta\bar{\varepsilon} \tag{6.5}$$

The choice to use Δ in Equation 6.5 reflects that the optical phase shift is measured discretely. The LF-DAS optical phase shift responds to the average strain and temperature over the gauge length, hence the notation of $\bar{T}$ and $\bar{\varepsilon}$. C_T and C_ε are the DAS thermal and strain coefficients, respectively.

$$C_T = \frac{4\pi n L_g}{\lambda}\left(\frac{\zeta_T}{n} + \frac{\zeta_\varepsilon}{n}\alpha + \alpha\right) \quad 6.6$$

$$C_\varepsilon = \frac{4\pi n L_g}{\lambda}\left(1 + \frac{\zeta_\varepsilon}{n}\right) \quad 6.7$$

Substituting the appropriate parameters from Table 6.1 and considering a 7-meter gauge length, C_T becomes 0.62 radians/milliKelvin and C_ε equals 68 radians/microstrain. Evaluating Equations 6.6 and 6.7 using the thermal expansion coefficient for glass fibers represents a conservative estimate of thermal effects on the LF-DAS optical phase shift. When a fiber is fastened to metal components, researchers have demonstrated that the high thermal expansion coefficient of the metal increases the thermal response of the fiber sensor (Magne et al. 1997). Using the thermal expansion coefficient for steel doubles the DAS thermal coefficient. However, the thermal expansion coefficient for fibers is on the same order of magnitude of the surrounding cement, which could dampen the thermal response of the steel. Whether the thermal expansion coefficient of steel or fiber is employed does not alter the conclusions of this study.

6.2. Numerical Methods: Integrated Model

To study the LF-DAS response due to propagating hydraulic fractures considering both temperature and strain, the workflow illustrates in Figure 6.1 was employed. First, fracture propagation was simulated using a commercially available hydraulic fracture simulator, GOHFER (Halliburton 2018). The resulting fracture geometries were exported to programs that computed the strain and temperature along a fiber optic cable located on a monitor well 440 feet laterally offset to the treatment well with no offset in true vertical depth. Equation 6.5 provides a basis to model the LF-DAS response due to

the modeled changes in strain and temperature. Waterfall plots were created that exclude and include thermal effects to observe how significantly temperature influences the LF-DAS response.

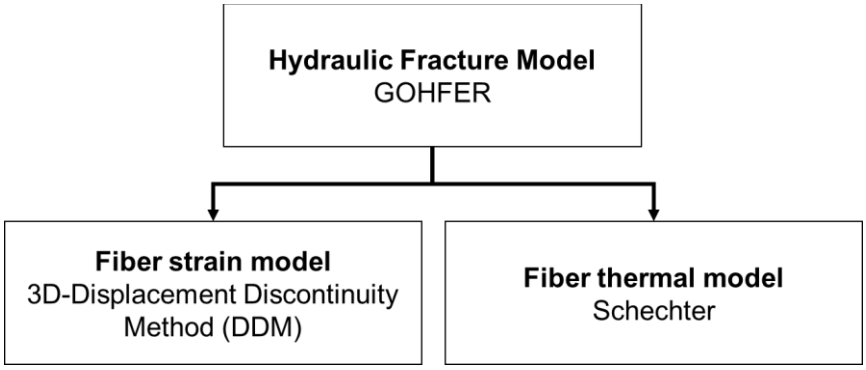

Figure 6.1 Workflow for simulating the LF-DAS response including thermal effects.

6.2.1. Hydraulic Fracture Propagation Model

A single state interval was simulated of a multi-cluster, limited-entry type completion typical in unconventional wells. Key parameters used in the GOHFER simulation are provided in Table 6.2. Reservoir mechanical properties required for the fracture model were computed from a synthetic well log using GOHFER's Auto-Log Assistant tool's default settings. The log used is provided in Appendix A.

Table 6.2 Parameters used in the fracture simulation.

Cluster spacing (feet)	20
# Clusters	5
Injection rate (BPM)	60
# Perforations/cluster	5
BPM/perf	2.4
Observation well horizontal offset	440 feet
Observation well TVD Offset	0 feet
Average Young's modulus (MMpsi)	2.8
Average Poisson's ratio	0.25
Gauge length (meters)	5

6.2.2. Strain Model

The simulated fracture geometries were exported every 6 seconds of simulated pump time. The geometries were then input into a three-dimensional displacement discontinuity method program to compute the strain along the offset monitor well as presented in Section 2.1.3. Specifically, Equations 2.63 and 2.69 were evaluated, reproduced here as Equations 6.8 and 6.9. Recall that $\boldsymbol{u_n}$ is a list of axial displacements along the fiber, $\boldsymbol{w}$ is a list containing the fracture width for each gridded element, and $\boldsymbol{B}$ is an influence coefficient matrix relating the effect of one fracture element's width w_i on the displacement at one location on the fiber $u_{n,j}$. The axial strain in the z direction, ε_z, was then computed by numerical differentiation using the central difference method.

$$\boldsymbol{u}_{\mathbf{n}} = \boldsymbol{B} \cdot \mathbf{w} \tag{6.8}$$

$$\varepsilon_z = \frac{u_n(i+1) - u_n(i-1)}{z(i+1) - z(i-1)} \quad 6.9$$

The strain rate along the fiber due to the propagating fractures, $\dot{\varepsilon}$, was then numerically evaluated by the central difference method.

$$\dot{\varepsilon} = \frac{\varepsilon_z(i+1) - \varepsilon_z(i-1)}{t(i+1) - t(i-1)} \quad 6.10$$

Where *t* is the time in seconds.

6.2.3. Hydraulic Fracture Temperature Model

An estimation of the temperature changes along a fiber optic cable was required to study thermal effects on LF-DAS sensors. Schechter's analytical solution for temperature in a domain that contains a rectangular fracture was employed to calculate the temperature along a hydraulic fracture's length (Schechter 1992). The model is presented in Equations 6.11 through 6.13, and estimates the temperature along the fracture where *x=0* represents the center of the fracture and the location of fluid injection. No temperature variation is modeled in the vertical direction. As will be discussed further in Chapter 6, the temperature at the fiber was assumed to be equal to the temperature within the fracture at the location of the fracture intersection.

$$T(x,t) = T_R - \left(T_R - T_{inj}\right)\left(1 - \frac{x}{x_f(t)}\right)^{\alpha_v} \quad 6.11$$

$$x_f(t) = \frac{q_{inj}\sqrt{t}}{2\pi Ch} \quad 6.12$$

$$\alpha_v = \frac{2}{C\rho c_p}\sqrt{\frac{k_f \rho_f c_{pf}}{\pi^3}} \quad 6.13$$

Here, x_f is the fracture half-length. Exponent α_v depends on the leak-off coefficient C, formation thermal conductivity k_f, density ρ_f, and specific heat coefficient c_{pf} as well as the density ρ and specific heat coefficient of the fluid c_p. The temperature at a point in the fracture at any time $T(x,t)$ depends on these parameters as well as the initial reservoir temperature, T_R, and the injected fluid temperature T_{inj}. As with strain rate, the temperature rate was computed numerically by the central difference method.

6.3. Simulated Fracture Geometries

Figure 6.2 illustrates the simulated fracture geometry after the first six minutes of pumping. The fractures are numbered by proximity to the heel and colored according to the fracture width. The fractures are planar and symmetrical. No longitudinal fractures are modeled. Fracture 3 does not intersect the observation well; the majority of the length growth occurs in the upper part of the fracture, above the observation well. The lower, minor portion of fracture 3 does not extend beyond 60 feet from the treatment well.

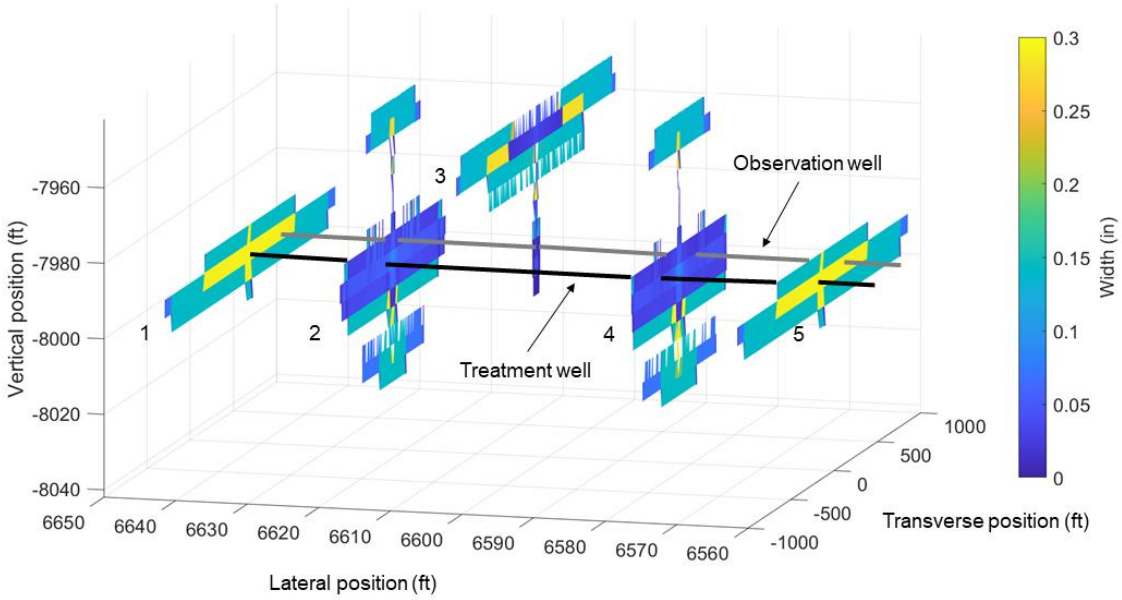

Figure 6.2 GOHFER simulated fracture geometry after six minutes of pumping.

In Figure 6.3a, the maximum half-length of each fracture is plotted during the first six minutes of pumping. The horizontal line at 440 feet represents the location of the observation well. Fractures 1, 2, 4 and 5 intersect the observation well between 2 and 4 minutes of pumping. Fracture 3 does not intersect the observation well. Figure 6.3b displays the evolution of the maximum fracture height of each fracture. As no inter-stage stress shadow is considered, there is symmetry between the modeled fractures. Fractures 1 and 5 grow similarly to each other, as do fractures 2 and 4. Fractures 1 and 5 remain within a low stress interval determined from the well log.

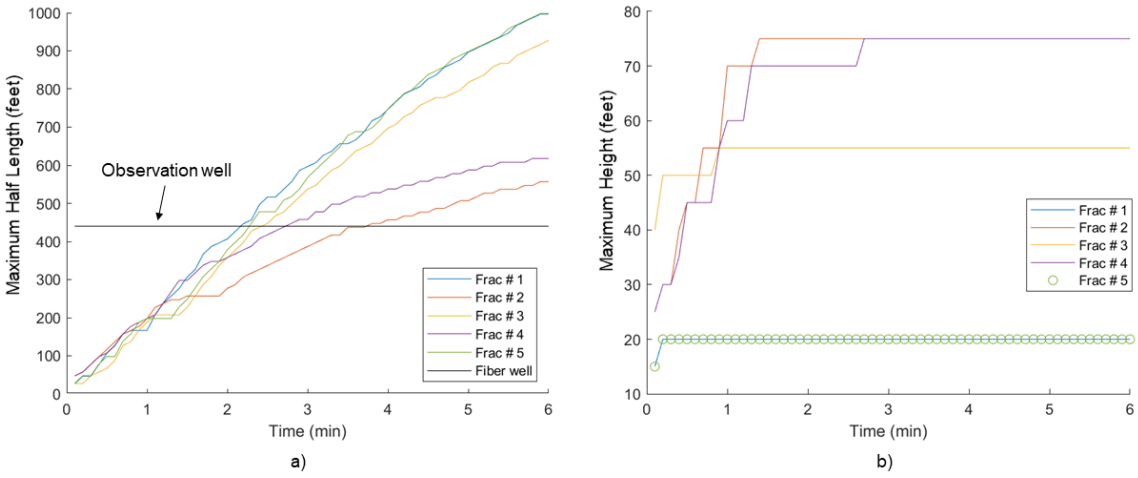

Figure 6.3 Maximum simulated fracture length (a) and height (b) over time.

6.4. Strain Rate Modeling Results

Strain rate patterns were generated by the displacement discontinuity method program. The simulated strain rate waterfall plot is shown in Figure 6.4 with time on the x axis, depth on the y axis, and simulated strain rate on as the color scale. The response is marked by a large region of extending fiber (yellow) converging to a narrow band surrounded by compressing fiber (blue), conforming to field observations as described by Ugueto et al. (2019). The color scale was terminated at an absolute value of 0.06 microstrain/s to highlight the converging region of extending fiber. The maximum modeled strain rate was 8.6 microstrain/s, and the minimum modeled strain rate was -11.9 microstrain/s. After the fracture intersection, complexity in the signal is

observed from the multiple propagating hydraulic fractures. This waterfall plot does not include thermal effects.

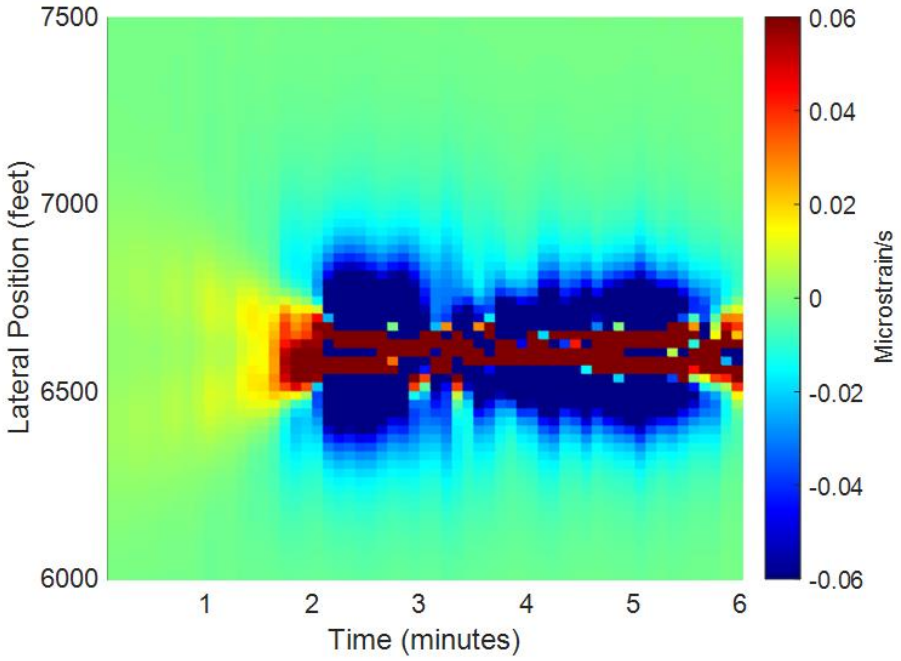

Figure 6.4 Synthetic LF-DAS waterfall plot considering only the strain rate component.

When applying this model, the coupling of the optical fiber to the formation should be considered. Lab experiments have demonstrated the ability for the optical fiber to slip within its protective tubing (Becker, 2018). Debonding was observed in the experiments discussed in chapter 4 of this work. The fiber, encased in a protective cable, is strapped

to the casing, and the casing bonds with the formation by cementing. The Young's Modulus of steel casing is multiple times that of rock, further dampening the fiber response to strain in the rock. In today's operations, most sensing fibers are protected with cushioning material (gel) to protect the sensing fiber from damage and prevent fiber slip. But decoupling of formation rock and steel casing during fracture hits impacts the sensing fiber responses. These considerations provide reason to expect the strain on the fiber to be less than the strain on the rock modeled here.

6.5. Temperature Modeling Results

Equations 6.11 to 6.13 and the LF-DAS temperature coefficient permit simulating a DAS waterfall plot including thermal effects. Each fracture was approximated as a rectangle by using an effective height for each fracture that ignores thin, minor sections of the fracture. For example, fractures 2 and 4 reach a maximum height of 75 feet, but 30 of those feet consist of thin sections with half lengths less than 70 feet. Thus, a fracture height of 45 feet results in an appropriate effective height to apply the temperature model. The leak-off coefficient was adjusted so that the fracture length modeled in 6.12 matched the simulated geometry at the time of the fracture hit. Figure 6.5 exhibits the temperature variation along the fracture half-length at one time. In Figure 6.6, the temporal variation of temperature and temperature rate at the monitor well is displayed at the locations where the fractures intersect the monitor well. By symmetry, fractures 1 and 5 have the same temperature profile, as do fractures 2 and 4. Fractures 2 and 4 cool slowly due to the larger effective fracture heights and lower fluid velocities in the fractures. As shown in Figure 6.6b, the time derivative of the temperature, which DAS

responds to, is nearly an order of magnitude greater for fractures 1 and 5 than fracture 2 and 4.

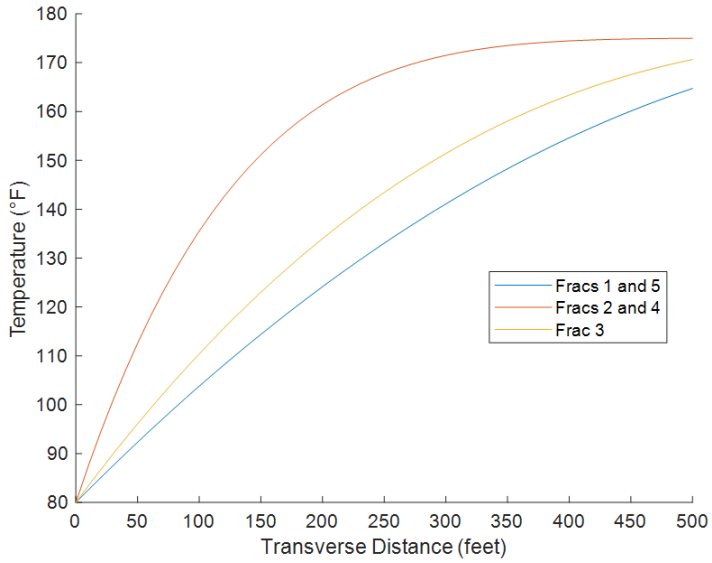

Figure 6.5 Simulated temperature along the fracture half-length

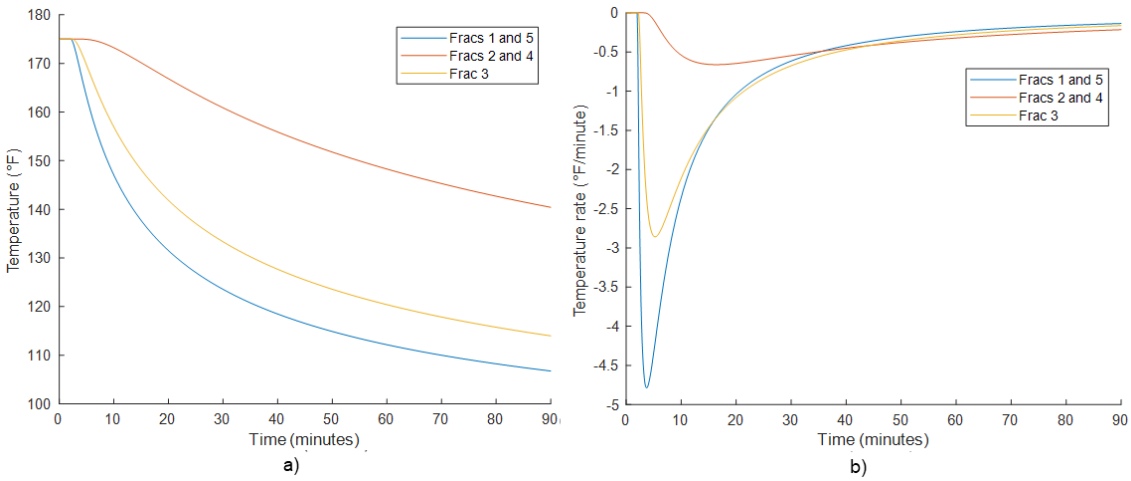

Figure 6.6 Simulated temperature at the fracture intersection locations over time

While this model provides an estimation of the temperature within the fracture, an estimate of the temperature along the fiber normal to the fracture face is required to simulate the LF-DAS response. DTS measurements have a spatial resolution of 1 meter, while the DAS gauge length determines the length scale of interest away from the fracture face. Two limiting cases are proposed for the temperature along the fiber due to an intersecting fracture. Heat transfer considering conduction perpendicular to the fracture face through the rock results in the smallest possible change in temperature along the fiber. On the other hand, a conduit may exist for fracture fluid to travel axially along the observation well such as channeling through the casing annulus or a longitudinal fracture. In this case, the temperature along the fiber could be approximated as the temperature of the fluid in the fracture at the location it intersects the observation well.

The conduction case is considered first. Figure 6.7 demonstrates the results of applying a 3D-finite difference conduction model to estimate the temperature along the fiber. Only fractures 1 and 5 are considered as they have the most potential to significantly alter the DAS signal. The results indicate that if conduction is the only means by which the fiber is cooled, cooling is limited to within 1 foot away from the fracture face over the duration of the pumping stage. This assumes that each fracture can be modeled as a single, planar, fracture, and does not consider branches or swarms of fractures that may intersect the well.

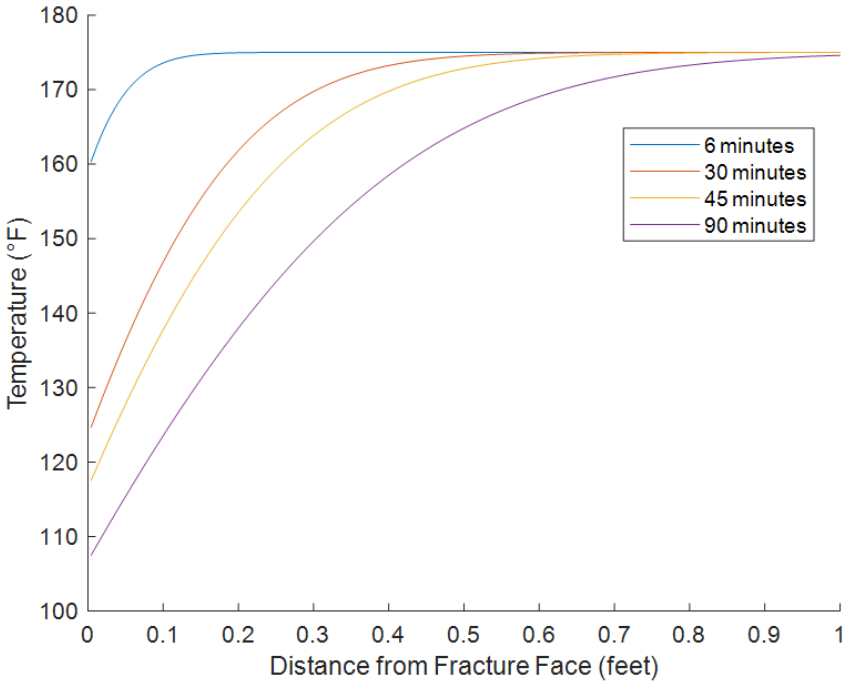

Figure 6.7 Temperature at the fiber vs. distance normal to the fracture face assuming conduction from fractures 1 and 5.

DTS and LF-DAS sensors respond to the average strain and temperature over the spatial resolution of the measurements. The signal associated with significant cooling in a 1-foot section of the fiber is minimized by the averaging of the signal over the gauge length. As illustrated in Figure 6.8, this signal minimization effect is less for DTS sensors than LF-DAS sensors due to the higher spatial resolution of DTS measurements. The computed temperature derivatives over the LF-DAS gauge length of 7 meters are two orders of magnitude less than the maximum temperature rate modeled in the fracture (compare to Fig. 7b). Interestingly, the spatial resolution of the sensors influences the timing of when the largest temperature change occurs. The largest temperature change by magnitude in the fracture occurs at 4 minutes by Schechter's model, but occurs at 7 minutes for DAS and 9 minutes for the DTS measurement. The modeled temperature rate of -0.18 °F/min should be detectable by DTS. For LF-DAS, the maximum temperature change by magnitude is less than 0.04 °F/min, corresponding approximately to a strain rate of 1 nanostrain per second.

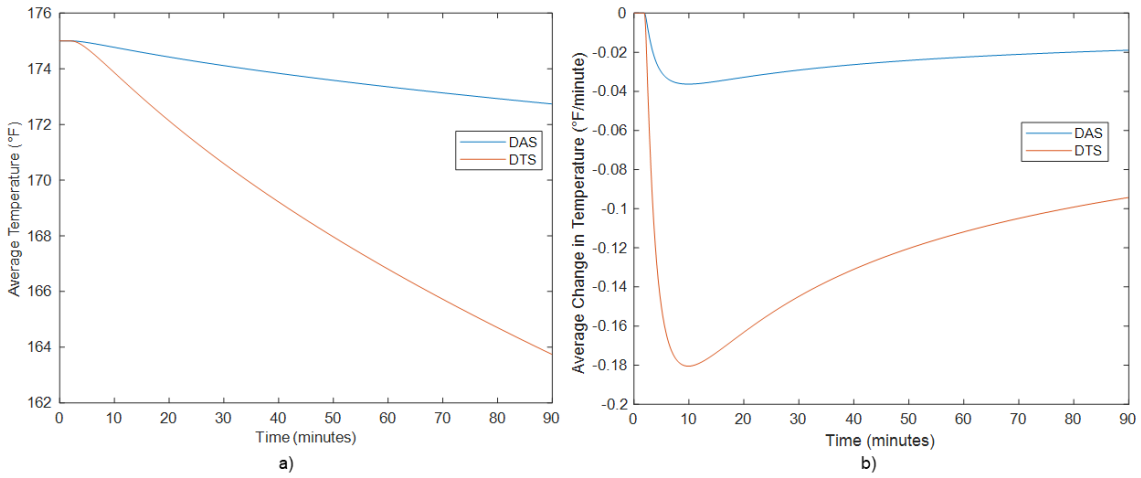

Figure 6.8 Temperature along the fiber (a) and its temporal derivative (b) averaged over the DTS and DAS spatial resolutions.

The second limiting case considers that a conduit exists for fracture fluid to travel axially along the instrumented well and cool the fiber optic cable. In this case, it is assumed that the fiber temperature is equal to the fracture fluid temperature where it intersects the well over a gauge length, or five meters in this synthetic example. The temperature change computed by Schechter's model for fractures 1 and 5 as shown in Figure 6.6b was converted to phase shift by Equation 6.5. Figure 6.9 presents the optical phase shift due to temperature and strain effects for a single channel corresponding to where fractures 1 and 5 intersected the observation well. It is significant to note the instances when the effects of temperature cause the polarity of the LF-DAS signal to switch from positive to negative. This corresponds to a color change on the LF-DAS waterfall plot

from yellow to blue. This finding suggests that temperature effects can appreciably affect LF-DAS interpretation after a fracture intersects the monitor well.

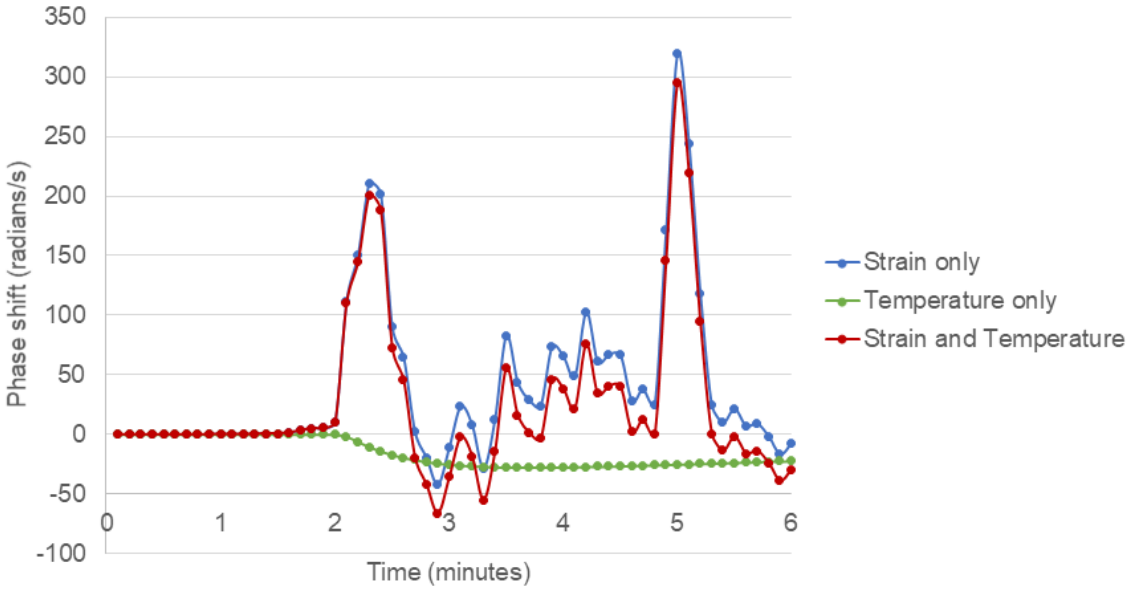

Figure 6.9 Simulated LF-DAS at a single channel on the optical fiber

6.6. LF-DAS Modeled Response Including Thermal Effects

With estimations of changes in strain and temperature along the fiber optic cable, a simulated LF-DAS waterfall plot can be generated that includes the effects of both mechanical and thermal phenomena. Figure 6.10 shows a LF-DAS waterfall plot that includes the effects of temperature changes. The units of the optical phase shift are

radians per second. As the temperature does not change until after the fracture intersects the observation well, the pattern of a large region of extension narrowing to a thin region of extension is preserved. Temperature effects should not typically impede the ability to recognize a fracture hit. However, as fracture fluid cools the observation well, additional complexity is added to the signal between 3 and 6 minutes, highlighted in Figure 6.11.

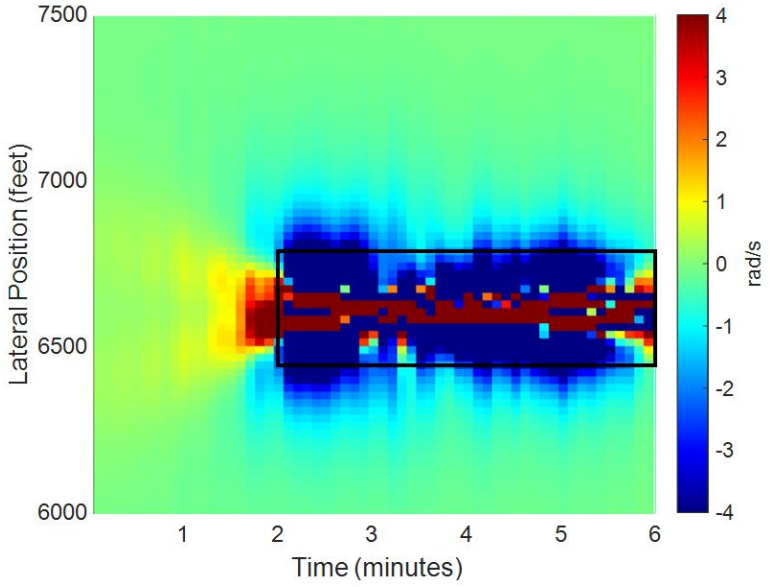

Figure 6.10 Simulated LF-DAS waterfall plot including strain rate and thermal effects

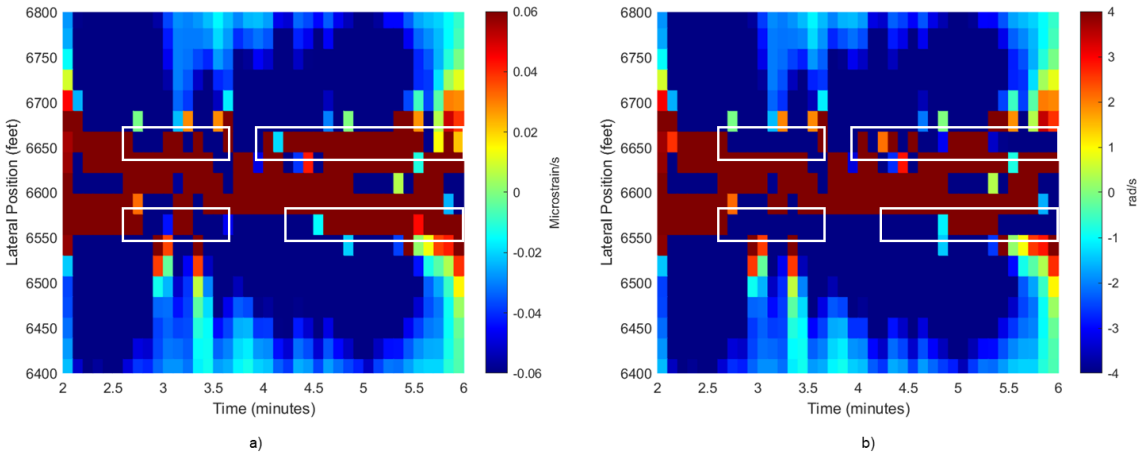

Figure 6.11 Comparison of strain rate (a) and LF-DAS (b) waterfall plots reveals that temperature changes add additional complexity to the signal

The results suggest that before, during, and immediately following a fracture intersecting a well instrumented with fiber, the strain on the fiber drives the LF-DAS signal. However, at later times, cool fracture fluid reaches the observation well. Then, the effects of the cooling temperature on the LF-DAS signal can equal or exceed strain effects, flipping the color over affected channels in the LF-DAS waterfall plots. Thermal effects on the LF-DAS are unlikely to change interpretations of the timing of fracture hits diagnosed from waterfall plots. The period of time before the fracture intersects the observation well is unaffected by temperature changes, and the strain response dominates the LF-DAS at the time of a fracture intersection. However, after the first fracture hit, temperature changes can obscure the interpretation of LF-DAS signals. In Section 6.4, the idea that the strain rate measured by the fiber is less than that of the

rock was presented. Therefore, it is possible that thermal effects can alter the LF-DAS signal more significantly than demonstrated in the synthetic example. Uncertainties in the fracture models and non-linear effects of temperature on the LF-DAS signal could also result in an overestimation of temperature effects in this work. However, the use of the fiber's thermal expansion coefficient instead of that of steel in Equation 6.6 represents a conservative estimation of the fiber's response to temperature.

6.7. Insights for Understanding Field Derived Waterfall Plots

We consider a LF-DAS waterfall plot from a field case to verify the concept of thermal effects on LF-DAS measurements. Figure 6.12 from Ugueto et al. (2019) visualizes the LF-DAS response at an observation well approximately 400 feet laterally offset and 160 feet vertically offset from a treatment well during a plug and perf completion. The treating pressure, rate, and proppant concentration are plotted synchronously below the waterfall plot. The characteristic region of extension focusing to a narrow region of extension surrounded by compression is visible. At the end of the stage, three regions of compressing fiber are identified that the researchers interpret as fractures that emanated from perforation clusters 4.1 to 4.3. At later times, the signal becomes complex, which can be interpreted as pulsations of an extending fracture. This is marked by the region in the black box. Strain rate response complexity after a fracture hit is evident from the GOHFER modeled synthetic case due to the interactions of multiple propagating fractures. A supplemental explanation for the signal complexity is that cool fracture fluid is altering the LF-DAS signal. Yet another explanation is that debonding of the fiber-

casing-cement-formation system is occurring, similar to what was observed in the laboratory experiments and discussed in Section 4.5.

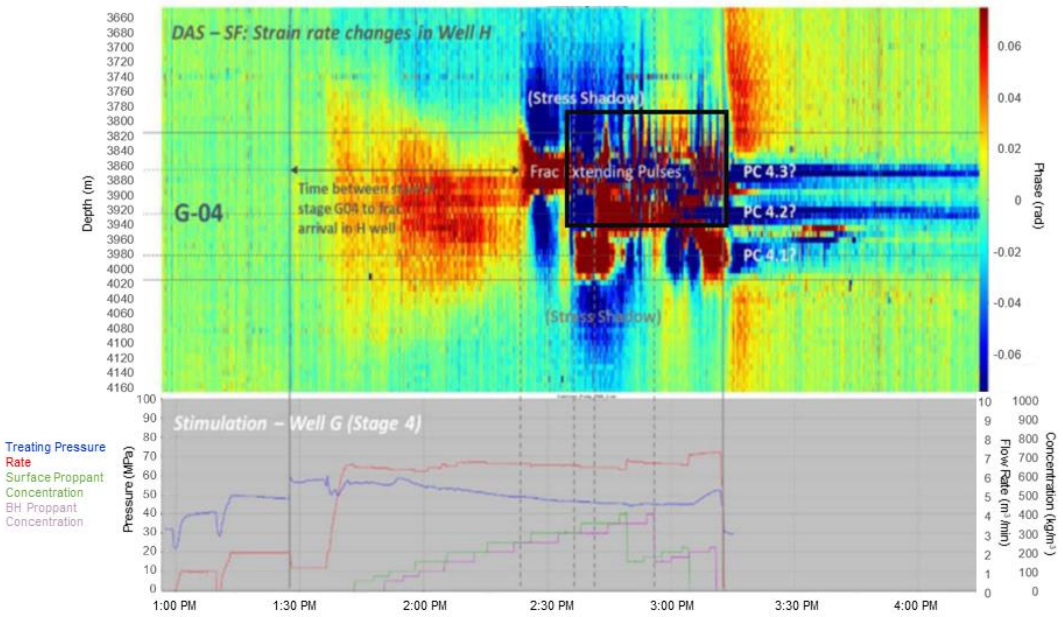

Figure 6.12 LF-DAS waterfall plot with corresponding offset well pumping plot (after Ugueto et al. 2019). Reproduced with permission from SPE.

6.8. A Proposed Sensor Configuration for LF-DAS Sensors

Finally, the ability to detect and interpret temperature changes at the milli-Kelvin scale could enable the development of new sensors to distinguish wet and dry fractures intersecting an observation well. Consider two LF-DAS cables run in tandem as in Figure 6.13. One fiber is mechanically coupled to the casing, while the other fiber is

within a conductive, protective coating that mechanically isolates the optical sensor from the surroundings. This configuration would enable two separate measurements: one responsive to both strain and temperature, one responsive only to temperature changes. Employing a model such as the one presented in this paper, the temperature effects could be removed from the measurements that responded to both strain and temperature and provide a purely mechanical measurement. Where cooling events are detected, wet fractures intersecting the observation well can be inferred. Strain rate events detected by the LF-DAS cables associated with these cooling events can be categorized separately from events that appear to be fracture intersections and yet have no associated cooling. As discussed, cooling events indicate high fracture fluid velocities, which are associated with fractures that take large injection rates. Therefore, the proposed sensor configuration should enable distinguishing the primary fractures from fractures that took less fluid or are dry in nature.

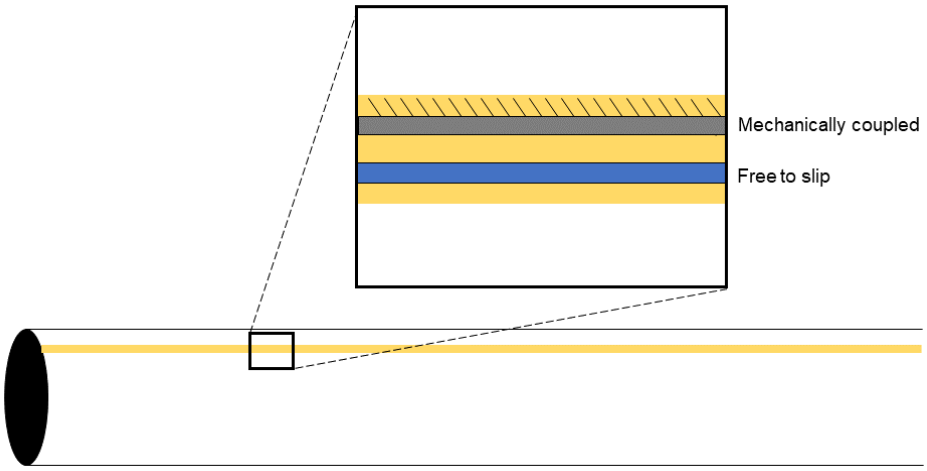

Figure 6.13 Proposed sensor configuration for high-resolution LF-DAS co-located temperature and strain measurements.

7. CONCLUSIONS

Low-frequency distributed acoustic sensing has proven to be a useful tool for informing hydraulic fracture completions in horizontal wells. Learnings from the experimental and numerical studies are summarized in this chapter.

7.1. Experimental Investigations

Learnings, conclusions, and contributions from the experimental investigations include:

1. A new laboratory experiment was developed to simulate the low-frequency distributed acoustic sensing response to a propagating hydraulic fracture.
2. The transparent EcoPoxy Flowcast Resin and Hardener system provides a means to visualize fracture growth while simultaneously recording measurements from embedded strain sensors with strong coupling to the fracture medium.
3. The mechanical behavior of the epoxy system used in this work can be adequately approximated by linear elastic relations.
4. Equation 3.22 accurately estimates the volume stored in a fluid injection system associated with a syringe pump due to two-phase liquid and gas compressibility.
5. The characteristic cone shaped region of extending fiber observed in strain rate waterfall plots indicates a fracture intersecting the fiber cables, or a frac hit.
6. Accurate determination of the timing of a frac hit from LF-DAS data depends on the spatial resolution of the fiber-casing-cement-formation system. Poor spatial resolution can lead to premature selections of the timing of a frac hit.
7. Debonding of the fiber-casing-cement-formation system affects the spatial resolution and can lead to prematurely selecting the timing of a frac hit event.

8. Equations 4.4 and 4.5 can be used to model the strain on the fiber to account for debonding near the location of the fracture intersection.
9. Both debonding and rapid drops in fracture pressure due to fracture growth spurts can cause negative pulses on the strain rate waterfall plot after the fracture intersection has occurred.
10. A fiber not intersected by a hydraulic fracture does not exhibit the characteristic cone shaped pattern and exhibited strain rates lower in magnitude than frac hit fibers.
11. The experimentally measured strains in the epoxy-fracture tests can be predicted by linear elastic finite element models. While the shape of the strain curves generated by Sneddon's model (Equation 4.2) follow the shape of the measured curve, they do not agree within uncertainty due to boundary effects.
12. The limited size of the unconstrained 8-inch fracture specimen caused disagreement between measured fracture radius and pressure and classical radial fracture models.
13. The zero strain and zero strain rate models can predict the nearest distance to the fracture front from LF-DAS data.
14. The zero strain and zero strain rate models remain unvalidated for $R_D < 0.5$.

7.2. Numerical Investigations of Temperature Effects

Conclusions of the numerical studies on the effect of temperature changes on the LF-DAS response include:

1. An integrated workflow was created to model changes in strain and temperature due to propagating hydraulic fractures from a horizontal well.

2. Equation 6.5 provides a relationship between the LF-DAS optical phase shift and changes in temperature and strain.
3. Temperature changes due to cool fracture fluid intersecting the monitor well will not change the interpretation of the timing of the fracture intersection event.
4. Temperature changes can appreciably alter the LF-DAS signal at a similar order of magnitude to strain changes after the frac hit occurs.
5. Cooling can cause additional complexity in LF-DAS waterfall plots after a frac hit occurs but has less of an effect if conduction is the only means by which heat is transferred along the fiber optic cable.
6. A new sensing configuration was proposed to harness the temperature sensitivity of LF-DAS sensors to garner additional information to characterize fractures intersecting the monitor well.

7.3. Final Remarks

This work has only touched the surface of interpreting LF-DAS data during offset fracturing. For example, a radial fracture model was assumed to develop the zero strain location method. An elliptical crack or rectangular crack model could easily be substituted to modify the zero strain location method for various fracture geometries. In addition, only a single propagating fracture is considered in the experiments and in the zero strain location method. By the principle of superposition, the strains due to multiple propagating fractures can be considered and incorporated into an interpretation method. Some of the results of this study are relevant for applications outside of petroleum engineering. The model relating changes in strain and temperature to the LF-DAS

optical phase shift can be applied in any distributed acoustic interrogation system. For instance, communication networks of fiber optic cables installed near the surface can be repurposed for strain or temperature sensing.

The use of light pulses to interrogate fiber optic cables for subsurface strain sensing offers a compelling analogy to experimentation and the pursuit of knowledge. Experimental investigations illuminate new knowledge out of the darkness of the unknown, just as light propagating in fiber optic cables through petroleum reservoirs illuminates hydraulic fracture propagation.

REFERENCES

2018. *Abaqus FEA*, Dassault Systemes (Reprint). https://www.3ds.com/products-services/simulia/products/abaqus/.

2021. *SmartSoft*, 4.2.4 edition, Smart Fibres (Reprint). https://www.smartfibres.com/products/smartsoft-software.

Alekseev, A. E., Vdovenko, V. S., Gorshkov, B. G. et al. 2015. A phase-sensitive optical time-domain reflectometer with dual-pulse diverse frequency probe signal. *Laser Physics* **25** (6): 065101. http://dx.doi.org/10.1088/1054-660X/25/6/065101.

Dake, L. P. 1978. *Fundamentals of reservoir engineering. L.P. Dake*: Elsevier Scientific Pub. Co.

Dakin, John Philip; Lamb, Christopher. 1990. Distributed fibre optic sensor system. United Kingdom; International (PCT) Patent No. GB2222247A.

EIA. 2021. *Annual Energy Outlook 2021*, EIA (Reprint). https://www.eia.gov/outlooks/aeo/.

Epstein, Alex. 2014. *The Moral Case for Fossil Fuels*. New York: Portfolio.

FBGS. What is the Young's Modulus of the DTG® Sensor?, https://fbgs.com/faq/what-is-the-youngs-modulus-of-the-dtg-sensor/ (accessed 11/2/2021.

Halliburton. 2018. *GOHFER 3D*, 9.1 edition (Reprint).

Harding, J. W. and Sneddon, I. N. 1945. The elastic stresses produced by the indentation of the plane surface of a semi-infinite elastic solid by a rigid punch. *Mathematical Proceedings of the Cambridge Philosophical Society* **41** (1): 16-

26. https://www.cambridge.org/core/article/elastic-stresses-produced-by-the-indentation-of-the-plane-surface-of-a-semiinfinite-elastic-solid-by-a-rigid-punch/00445496AC9A50B290DA4CE7029243E9.

Hartog, Arthur H. 2017. *An Introduction to Distributed Optical Fibre Sensors*. Oakville, CANADA: Taylor & Francis Group.

Haustveit, Kyle, Elliott, Brendan, Haffener, Jackson et al. 2020. Monitoring the Pulse of a Well Through Sealed Wellbore Pressure Monitoring, a Breakthrough Diagnostic With a Multi-Basin Case Study. *Proc.,* SPE Hydraulic Fracturing Technology Conference and Exhibition. https://doi.org/10.2118/199731-MS.

Hicke, K., Eisermann, R., and Chruscicki, S. 2019. Enhanced Distributed Fiber Optic Vibration Sensing and Simultaneous Temperature Gradient Sensing Using Traditional C-OTDR and Structured Fiber with Scattering Dots (in eng). *Sensors (Basel)* **19** (19).

Hurtig , E. , J. Schrotter , S. Grosswig , K. Kiihn , B. Harjes , W. Wieferig , and R. P. Orrell .,. 1993. Borehole temperature measurements using distributed fibre optic sensing. *Scientific Drilling* **3** (6): 283 – 286 .

IEA. World Energy Outlook 2021. *IEA*, https://www.iea.org/reports/world-energy-outlook-2021.

Jin, Ge and Roy, Baishali. 2017. Hydraulic-fracture geometry characterization using low-frequency DAS signal. *The Leading Edge* **36** (12): 975-980. https://library.seg.org/doi/abs/10.1190/tle36120975.1.

Karrenbach, Martin, Cole, Steve, Ridge, Andrew et al. 2019. Fiber-optic distributed acoustic sensing of microseismicity, strain and temperature during hydraulic fracturing. *GEOPHYSICS* **84** (1): D11-D23. https://library.seg.org/doi/abs/10.1190/geo2017-0396.1.

Kersey, A. D. , Davis, M. A. , Patrick, H. J. et al. 1997. Fiber grating sensors. *Journal of Lightwave Technology* **15** (8): 1442-1463.

Krohn, David A., MacDougall, Trevor W., and Alexis, Mendez. 2015. Fiber Optic Sensors: Fundamentals and Applications, Fourth Edition. In. Bellingham, Washington: SPIE Press.

Liu, Yongzan, Wu, Kan, Jin, Ge et al. 2020. Hydraulic Fracture Modeling of Fracture-Induced Strain Variation Measured by Low-Frequency Distributed Acoustic Sensing (LF-DAS) along Offset Wells. *Proc.,* 54th US Rock Mechanics/Geomechanics Symposium.

Molenaar, M.M.. M., Hill, D.J.. J., Webster, P.. et al. 2012. First Downhole Application of Distributed Acoustic Sensing for Hydraulic-Fracturing Monitoring and Diagnostics. *SPE Drilling & Completion* **27** (01): 32-38. https://doi.org/10.2118/140561-PA.

Moran, Michael and Shapiro, Howard. 2000. *Fundamentals of Engineering Thermodynamics*, 4th edition: John Wiley & Sons, Inc.

Morita, Nobuo. 2021. *Finite Element Programming in Non-linear Geomechanics and Transient Flow*. Cambridge, MA: Gulf Professional Publishing.

Pakhotina, Iuliia, Sakaida, Shohei, Zhu, Ding et al. 2020. Diagnosing Multistage Fracture Treatments with Distributed Fiber-Optic Sensors. *SPE Production & Operations* **35** (04): 0852-0864. https://doi.org/10.2118/199723-PA.

Raterman, Kevin T., Farrell, Helen E., Mora, Oscar S. et al. 2018. Sampling a Stimulated Rock Volume: An Eagle Ford Example. *SPE Reservoir Evaluation & Engineering* **21** (04): 927-941. https://doi.org/10.2118/191375-PA.

Rohatgi, Ankit. 2021. *WebPlotDigitizer*, 4.5 edition (Reprint). https://automeris.io/WebPlotDigitizer/.

Schechter, R.S. 1992. *Oil Well Stimulation*: Prentice Hall.

Shahri, Mojtaba, Tucker, Andrew, Rice, Craig et al. 2021. High Fidelity Fibre-Optic Observations and Resultant Fracture Modeling in Support of Planarity. *Proc.,* SPE Hydraulic Fracturing Technology Conference and Exhibition. https://doi.org/10.2118/204172-MS.

Smith, M. B. and Montgomery, C. 2015. Hydraulic Fracturing. In: CRC Press.

Sneddon, I. N. 1946. The Distribution of Stress in the Neighbourhood of a Crack in an Elastic Solid. *Proceedings of the Royal Society of London Series A, Mathematical and Physical Sciences* **187** (1009): 229-260. http://www.jstor.org/stable/97970.

Taylor, Henry F.; Lee, Chung E. 1993. Apparatus and method for fiber optic intrusion sensing. United States; International (PCT) Patent No. US5194847A.

Tosi, Daniele. 2017. Review and Analysis of Peak Tracking Techniques for Fiber Bragg Grating Sensors. *Sensors* **17** (10): 2368. https://www.mdpi.com/1424-8220/17/10/2368.

Ugueto, Gustavo A., Todea, Felix, Daredia, Talib et al. 2019. Can You Feel the Strain? DAS Strain Fronts for Fracture Geometry in the BC Montney, Groundbirch. *Proc.,* SPE Annual Technical Conference and Exhibition. https://doi.org/10.2118/195943-MS.

Wu, Kan. 2014. *Numerical Modeling of Complex Hydraulic Fracture Development in Unconventional Reservoirs*PhD dissertation, The University of Texas at Austin, Austin, Texas (December 2014).

Zhang, Zhishuai, Fang, Zijun, Stefani, Joe et al. 2020. Fiber Optic Strain Monitoring of Hydraulic Stimulation: Geomechanical Modeling and Sensitivity Analysis. *Proc.,* SPE/AAPG/SEG Unconventional Resources Technology Conference. https://doi.org/10.15530/urtec-2020-2648.

APPENDIX A

ZERO STRAIN LOCATION METHOD PROGRAM

```
function radius = Z_Zero_Sneddon(r,zero_location)

%Estimate radius from zero location. r, z consistent units

z = linspace(0,zero_location*2,500);
R = linspace(r/100,r*.95,300);

%Loop
Nz = length(z);
NR = length(R);
Uz = zeros(Nz,NR);
P = 1; E = 1; poisson = .3;
for j=1:NR
    %R(j)
    for i=1:Nz
        %z(i)
        Uz(i,j) = Sneddon1946(P,R(j),E,poisson,z(i),r); %meters
    end
end

%calculate strain
ezz = zeros(Nz,NR);
ezz(1,:) = (Uz(2,:)-Uz(1,:))./(z(2)-z(1));
ezz(Nz,:) = (Uz(Nz,:)-Uz(Nz-1,:))./(z(Nz)-z(Nz-1));
ezz(2:Nz-1,:) = (Uz(3:Nz,:)-Uz(1:Nz-2,:))./(z(3:Nz)-z(1:Nz-2));

[~, zero_indices] = min(abs(ezz));
z_almost_zeros = z(zero_indices);
z_zeros = zeros(NR,1); ezz_almost_zeros = zeros(NR,1);
for i=1:NR
    ezz_almost_zeros(i) = ezz(zero_indices(i),i);
    if zero_indices(i) == Nz
        z_zero = z_almost_zeros(i);
    elseif ezz_almost_zeros(i) > 0
        %Interpolate forwards
        e1 = ezz_almost_zeros(i);
        z1 = z_almost_zeros(i);
        point2_indx = zero_indices(i)+1;
        e2 = ezz(point2_indx,i);
        z2 = z(point2_indx);
        z_zeros(i) = interpolate_zero_strain(e1, e2, z1, z2);

    elseif ezz_almost_zeros(i) < 0
        %Interpolate backwards
        e2 = ezz_almost_zeros(i);
        z2 = z_almost_zeros(i);
        point1_indx = zero_indices(i)+1;
        e1 = ezz(point1_indx,i);
        z1 = z(point1_indx);
        z_zeros(i) = interpolate_zero_strain(e1, e2, z1, z2);

    elseif ezz_almost_zeros(i) == 0
        warning_zero_location = 'Exact match for zero strain, is this real?'
```

```
        z_zeros(i) = z_almost_zeros(i);

    end
end

[error, z_index] = min(abs(z_zero - z_location));
radius = R(z_index);


end
```

```
function U3 = Sneddon1946(P,c,E,poisson,z,r)


%Calculations
if c < 0
    error = 'negative radius'
elseif c == 0
    U3 = 0;
else
    if z<0
        z = z*-1;
    end
    K = -4*P*c*(1-poisson^2)/(pi*E);
    rho = r/c;   zeta = z/c;

    if zeta == 0
        if r < c
            U3 = 4*P*(1-poisson^2)./(pi*E).*sqrt(c.^2-r.^2);
        elseif r >= c
            U3 = 0;
        end
    elseif zeta < 0
        error_Sneddon1946_function = 'zeta less than zero'
    elseif zeta > 0
        U3 = K*integral(@(eta) fun(eta,zeta,poisson,rho),0,inf);
    end
end


function y = fun(eta,ZETA,SIGMA,RHO)
    y = (1+ZETA.*eta./(2.*(1-SIGMA))).*...
        (cos(eta)./eta - sin(eta)./eta.^2).*...
        exp(-1.*ZETA.*eta).*...
        besselj(0,RHO.*eta);
end

end
```

APPENDIX B

LOG DATA USED IN GOHFER SIMULATION

MD.ft	GR.API	S_w.frac	MD.ft	GR.API	S_w.frac	MD.ft	GR.API	S_w.frac
6000	108.5664	0.563508	7920	90.4699	0.279923	8220	105.7956	0.613605
6100	75.29844	0.5797	7930	107.809	0.287614	8230	109.8903	0.678093
6200	53.98913	0.546319	7940	99.95133	0.249096	8240	112.2687	0.549722
6300	81.61281	0.539353	7950	26.94899	0.252482	8250	98.63406	0.516365
6400	38.03045	0.597233	7960	15.25986	0.256989	8260	104.9982	0.548468
6500	72.40183	0.505897	7970	12.07389	0.216588	8270	100.46	0.694078
6600	65.11481	0.576602	7980	28.24977	0.272849	8280	95.45122	0.596495
6700	34.63766	0.543635	7990	39.90552	0.249156	8290	100.166	0.544951
6800	90.0998	0.500601	8000	13.01309	0.222439	8300	20.21648	0.636758
6900	106.191	0.548597	8010	19.27792	0.291896	8310	34.13673	0.588721
7000	39.32059	0.545038	8020	26.32131	0.286298	8320	39.43233	0.652353
7100	47.81622	0.588336	8030	17.17486	0.215472	8330	15.6134	0.56646
7200	81.225	0.503454	8040	37.58087	0.211164	8340	31.46136	0.658739
7300	32.20313	0.513644	8050	28.16807	0.234203	8350	24.61283	0.688758
7400	33.30949	0.567216	8060	101.0191	0.294096	8360	37.74409	0.650679
7500	41.46061	0.506107	8070	102.3435	0.2376	8370	81.49516	0.615605
7600	45.3296	0.521743	8080	94.67553	0.230035	8380	42.94686	0.657114
7700	88.08146	0.508884	8090	114.8623	0.56584	8390	16.95016	0.501264
7800	47.92316	0.532218	8100	90.132	0.605301	8400	51.88848	0.637533
7810	44.82224	0.283562	8110	109.0562	0.528279	8410	48.15114	0.592383
7820	26.24725	0.240879	8120	100.0585	0.676736	8420	91.41986	0.50732
7830	80.40945	0.221321	8130	99.50949	0.531975	8430	50.31071	0.512031
7840	17.96179	0.241197	8140	112.8888	0.632355	8440	66.99913	0.588045
7850	106.4841	0.280542	8150	95.40694	0.593582	8450	50.61214	0.650861
7860	105.1544	0.267417	8160	99.90117	0.608738	8460	56.25769	0.592738
7870	97.48119	0.231405	8170	102.7681	0.653686	8470	56.69187	0.696171
7880	100.9922	0.280274	8180	109.6719	0.632932	8480	87.46151	0.669493
7890	99.08541	0.219806	8190	97.42478	0.536963	8490	89.9468	0.654939
7900	100.1836	0.267211	8200	99.97628	0.572915	8500	80.43213	0.531363
7910	114.4006	0.292091	8210	105.3683	0.537977			

APPENDIX C

DETAILED EXPERIMENTAL RESULTS

Test A – No fiber

A series of tests were performed in epoxy blocks with no fiber to develop a procedure for generating radial, transverse fractures. In this test, the aluminum tubing was directly embedded in the epoxy. Fracture fluid leaked around the tubing-epoxy interface. Future experiments were modified so that a hole was drilled through the initial flaw and then the tubing was installed with an O-ring. This solved the problem of fracture fluid leaking around the tubing.

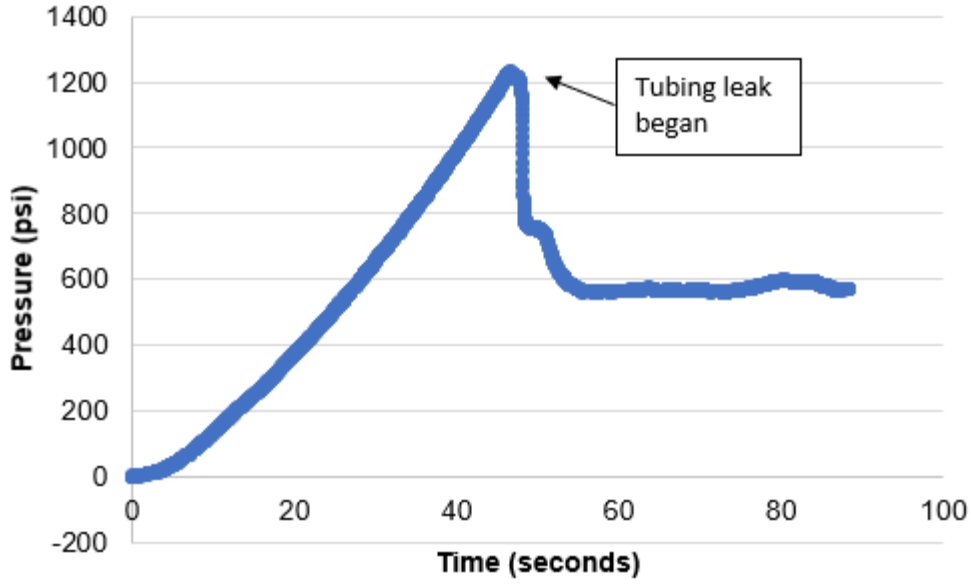

Test B – No fiber

This test used an O-ring and demonstrated that radial fractures could be generated with no leakage around the tubing.

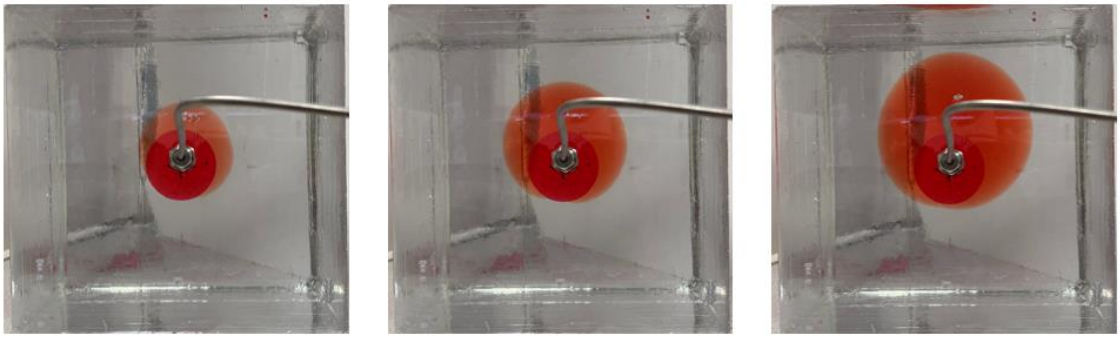

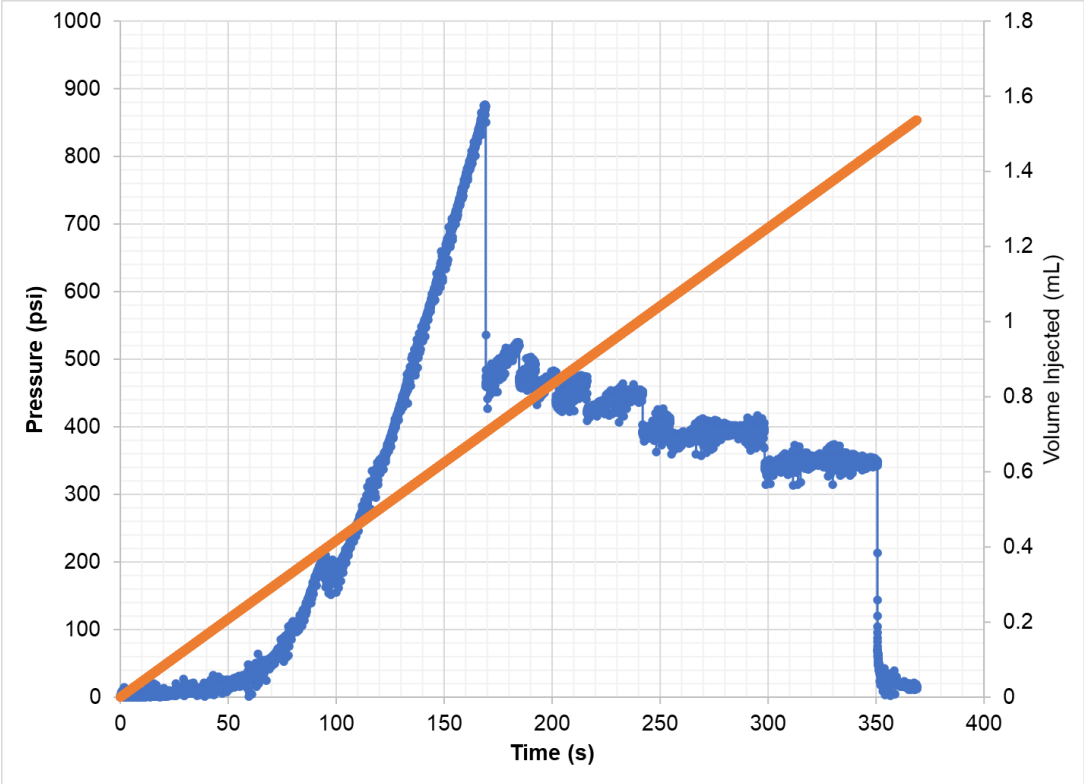
Pressure (psi)
Volume Injected (mL)
Time (s)
1000
900
800
700
600
500
400
300
200
100
0
1.8
1.6
1.4
1.2
1
0.8
0.6
0.4
0.2
0
0
50
100
150
200
250
300
350
400

Test C

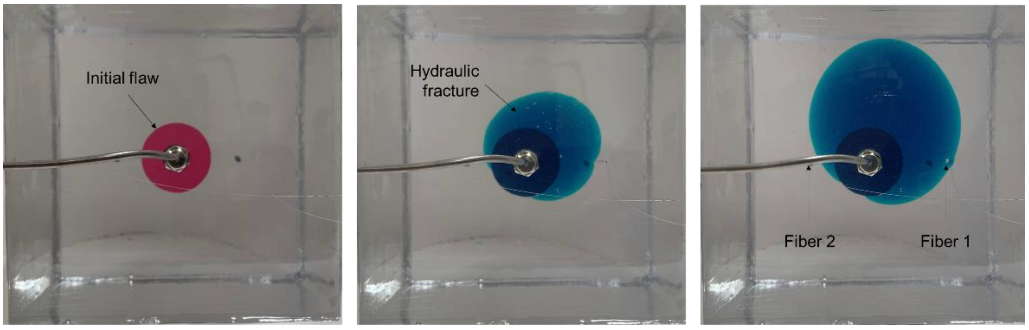
Initial flaw
Hydraulic fracture
Fiber 2
Fiber 1
a)
b)
c)

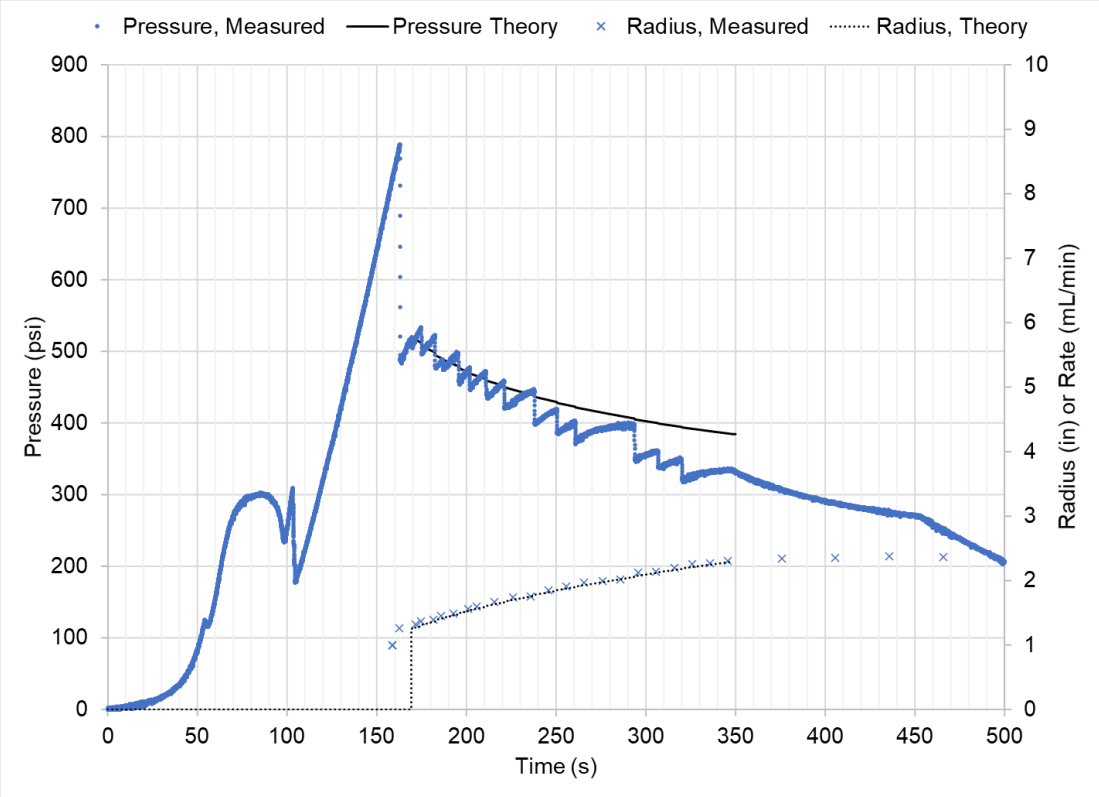

FBG #	z Location (inches)
FBG 1 - 1545	2.94
FBG 2	1.96
FBG 3	0.98
FBG 4	0.00
FBG 5	-0.98
FBG 6	-1.96
FBG 7	-2.94
FBG 8 - 1531	-3.92

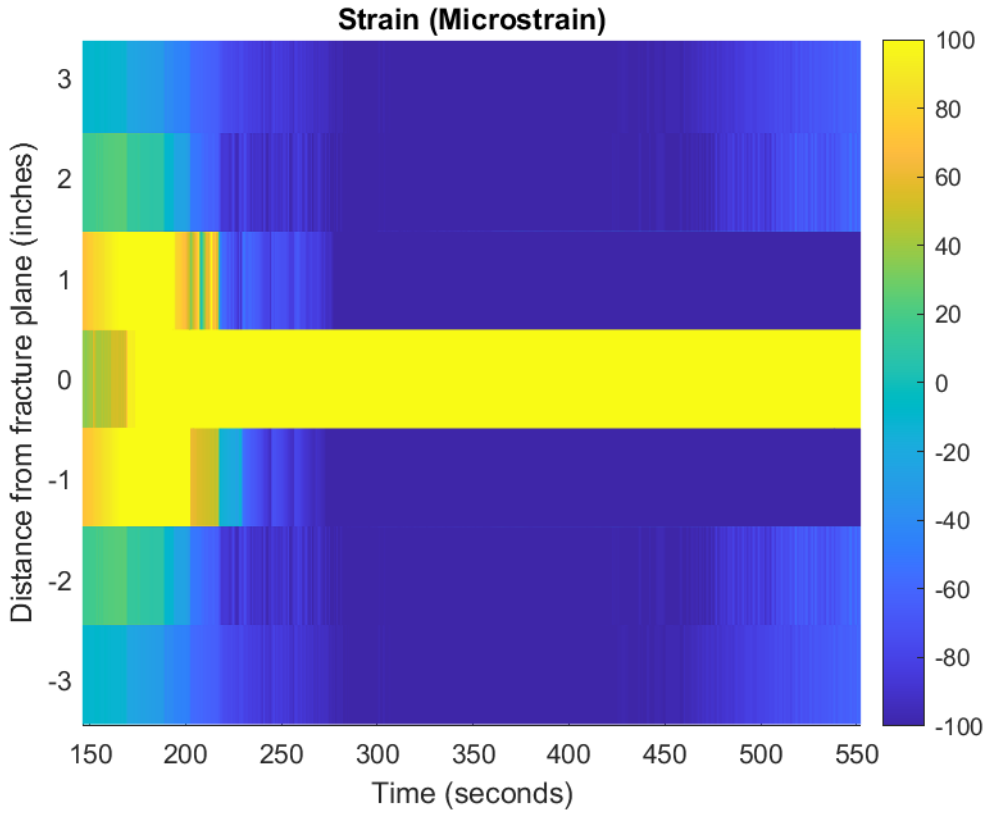
Strain (Microstrain)
Distance from fracture plane (inches)
3
2
1
0
-1
-2
-3
150
200
250
300
350
400
450
500
550
Time (seconds)
100
80
60
40
20
0
-20
-40
-60
-80
-100

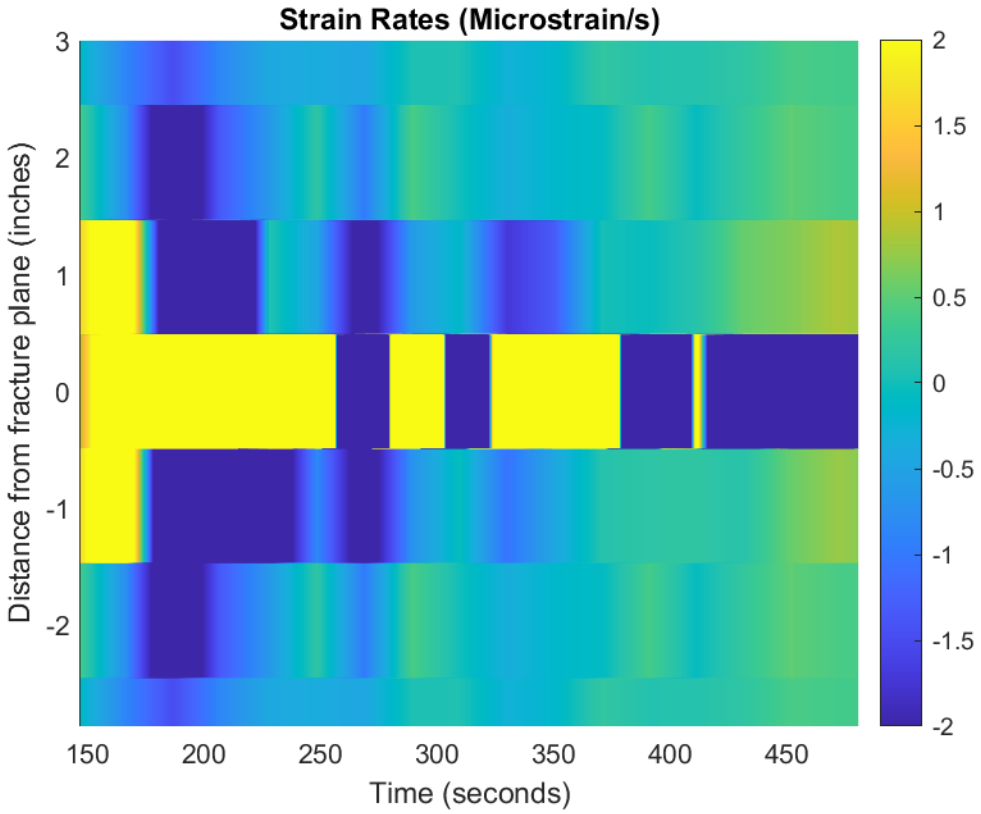
Strain Rates (Microstrain/s)
Distance from fracture plane (inches)
3
2
1
0
-1
-2
150
200
250
300
350
400
450
Time (seconds)
2
1.5
1
0.5
0
-0.5
-1
-1.5
-2

Test D

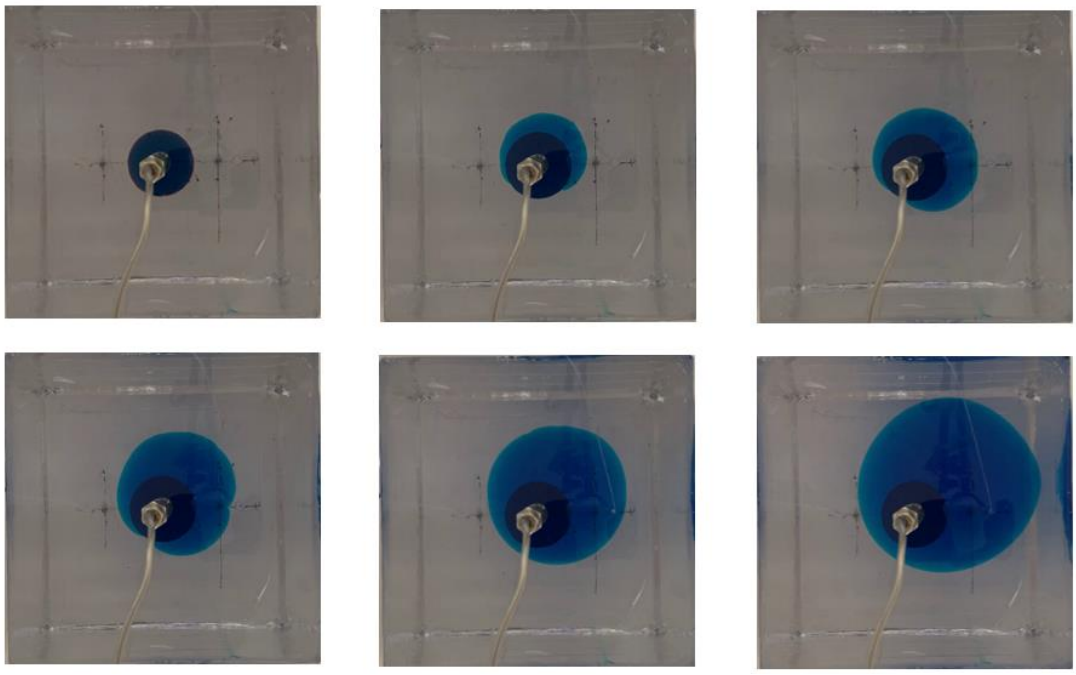

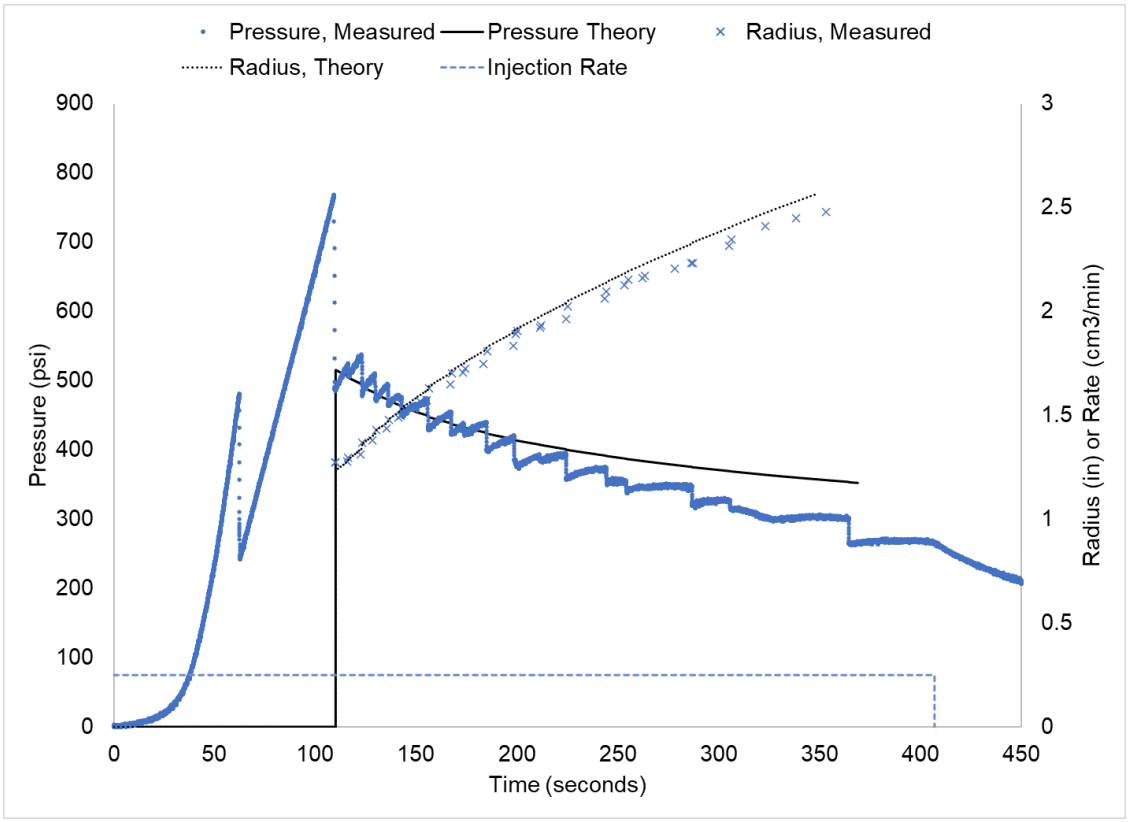
Pressure, Measured
Pressure Theory
Radius, Measured
Radius, Theory
Injection Rate
Pressure (psi)
Radius (in) or Rate (cm3/min)
Time (seconds)
0
100
200
300
400
500
600
700
800
900
0
0.5
1
1.5
2
2.5
3
0
50
100
150
200
250
300
350
400
450

	Z locations (inches)			
FBG#-w	Fiber 1	Fiber 2	Fiber 3	Fiber 4
1 - 1545	3	3.5	3.5	3
2 - 1543	2	2.5	2.5	2
3 - 1541	1	1.5	1.5	1
4 - 1539	0	0.5	0.5	0
5 - 1537	-1	-0.5	-0.5	-1
6 - 1535	-2	-1.5	-1.5	-2
7 - 1533	-3	-2.5	-2.5	-3
8 - 1531	-4	-3.5	-3.5	-4

Fibers 1 and 2

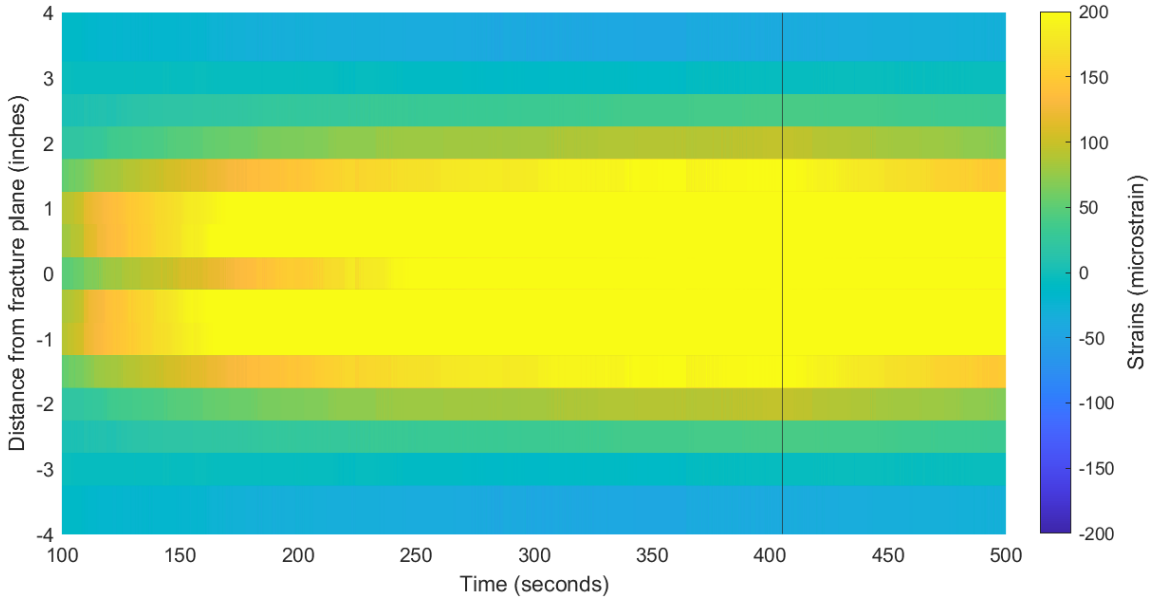

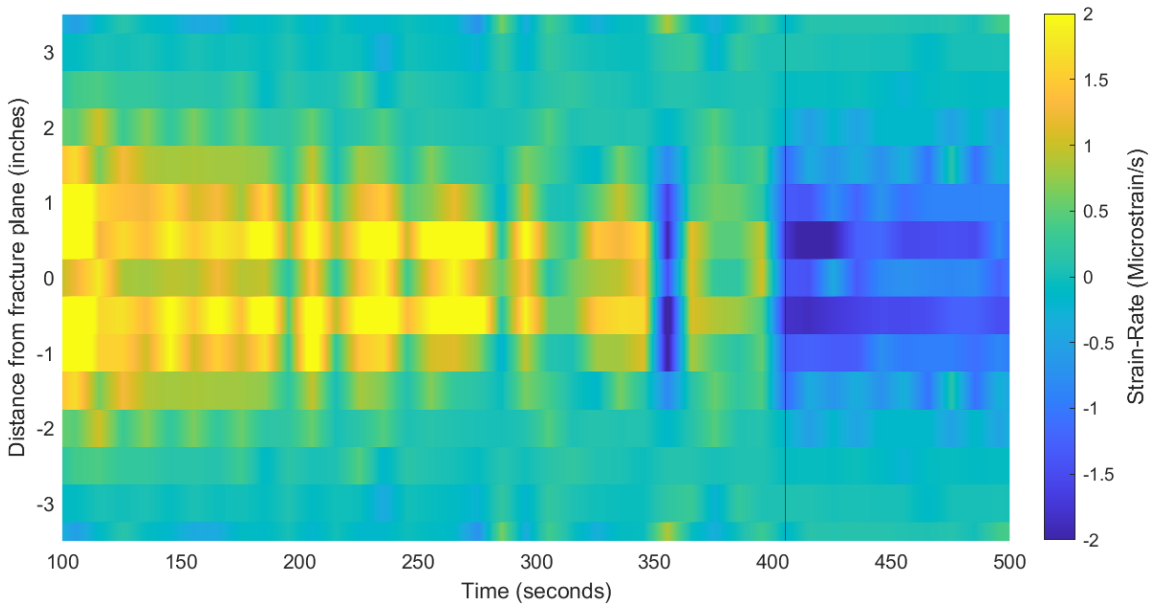
Distance from fracture plane (inches)
3
2
1
0
-1
-2
-3
100
150
200
250
300
350
400
450
500
Time (seconds)
2
1.5
1
0.5
0
-0.5
-1
-1.5
-2
Strain-Rate (Microstrain/s)

Fibers 3 and 4

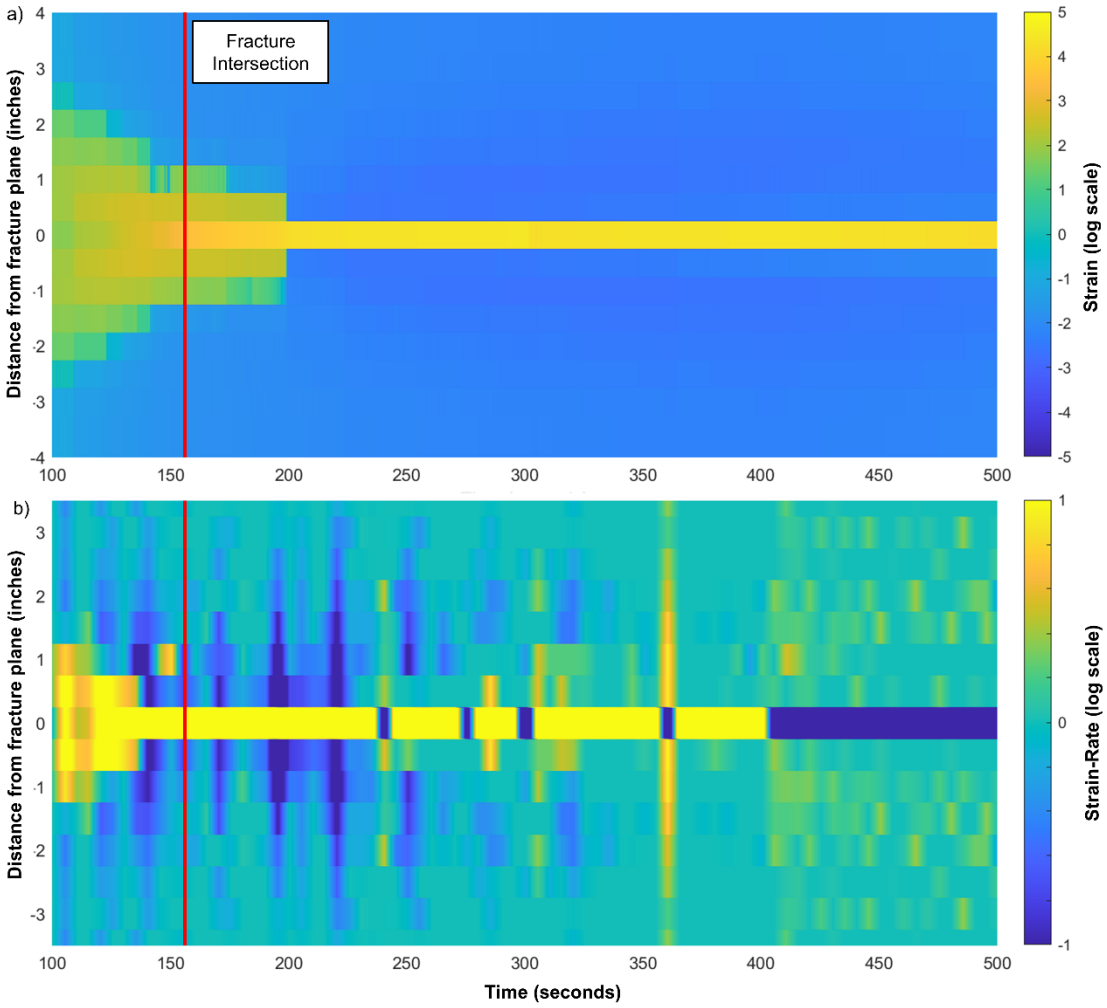

Test E

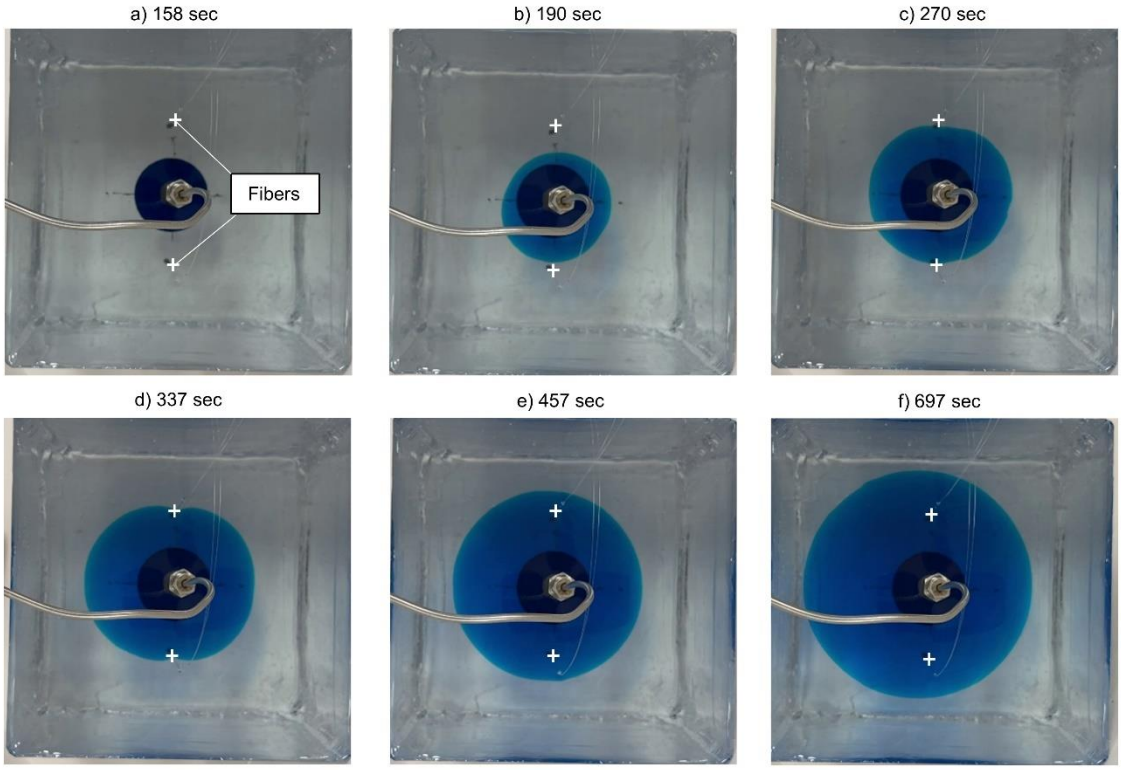

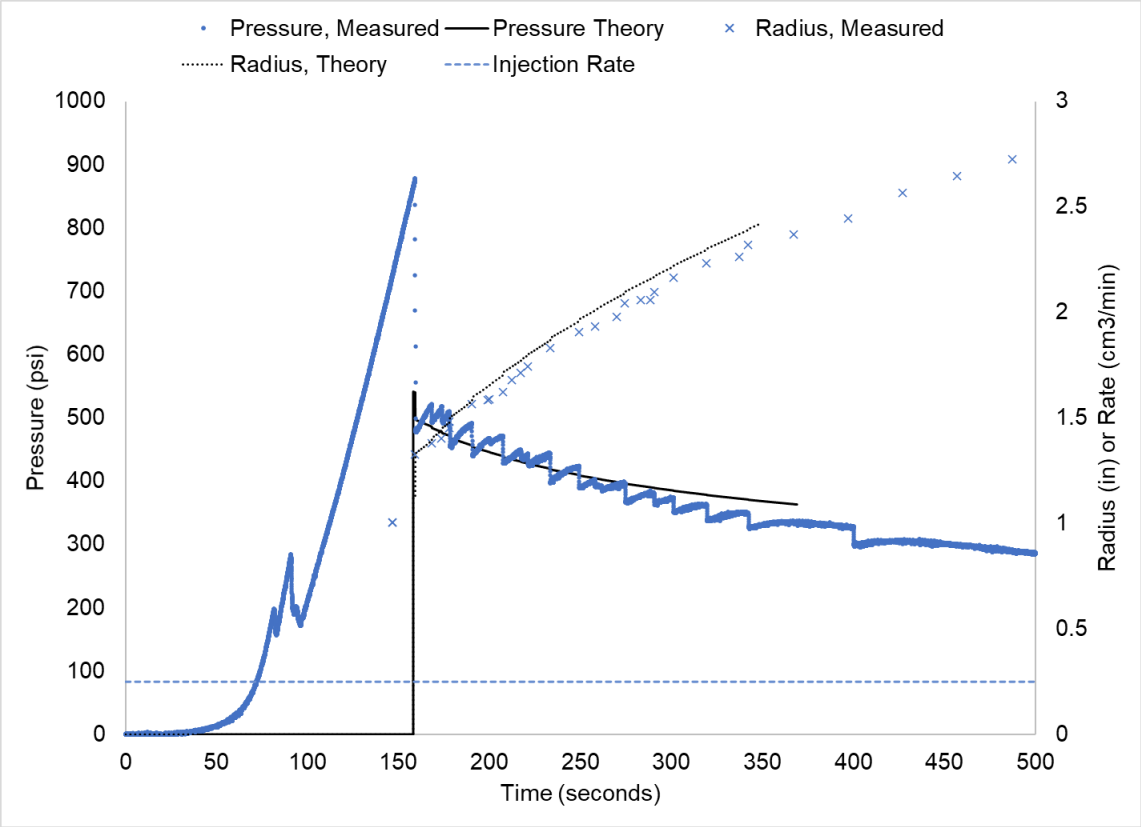

	Locations, z from crack (inches)			
FBG#-w	Fiber 1	Fiber 2	Fiber 3	Fiber 4
1 - 1557	0	0	0	0
2 - 1555	0.39	0.59	0.39	0.59
3 - 1553	0.79	0.98	0.79	0.98
4 - 1551	1.18	1.38	1.18	1.38
5 - 1549	1.57	1.77	1.57	1.77
6 - 1547	1.97	2.17	1.97	2.17
7 - 1545	2.36	2.56	2.36	2.56
8 - 1543	2.76	2.95	2.76	2.95

Fibers 1 and 2

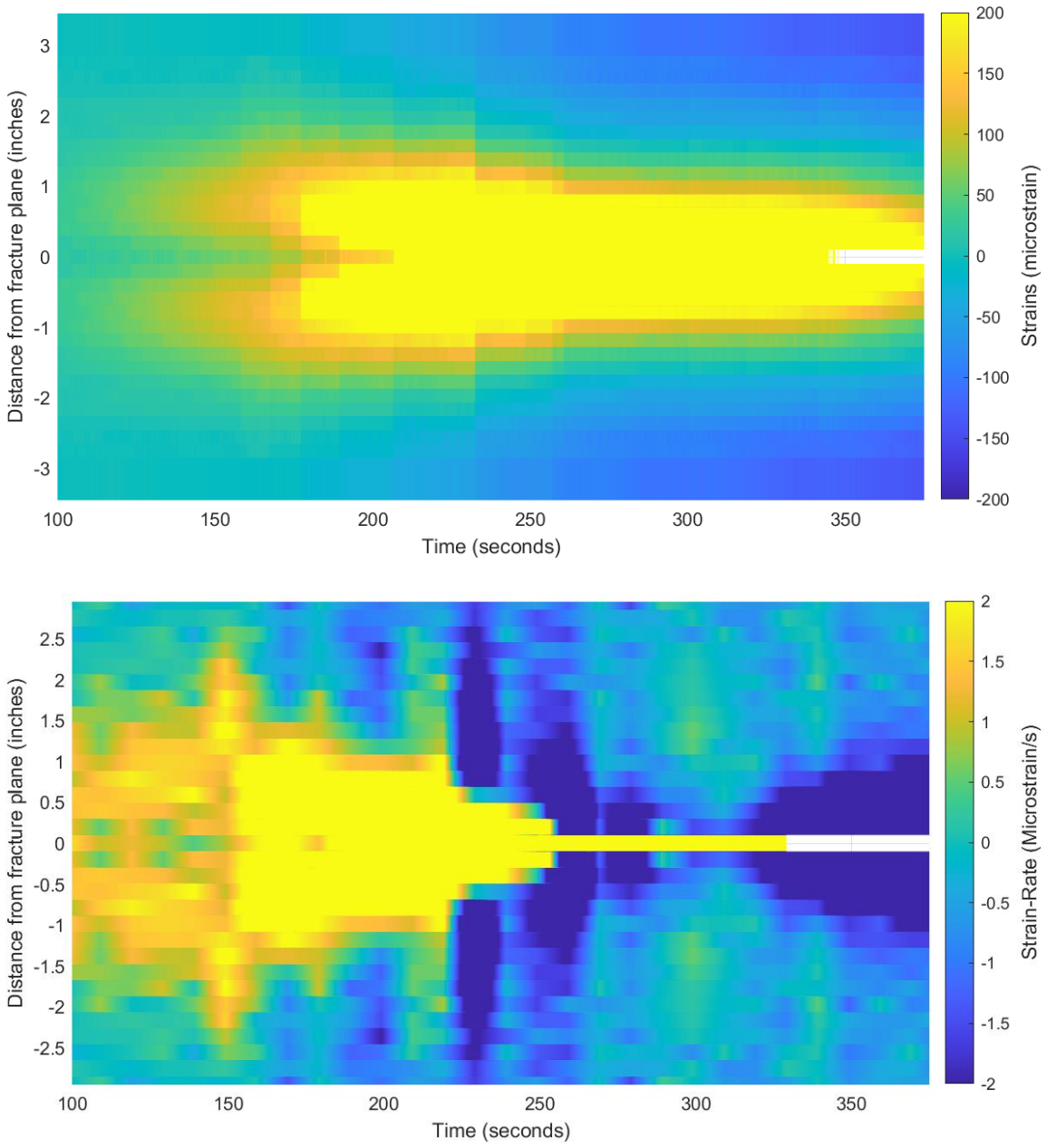

Fibers 3 and 4

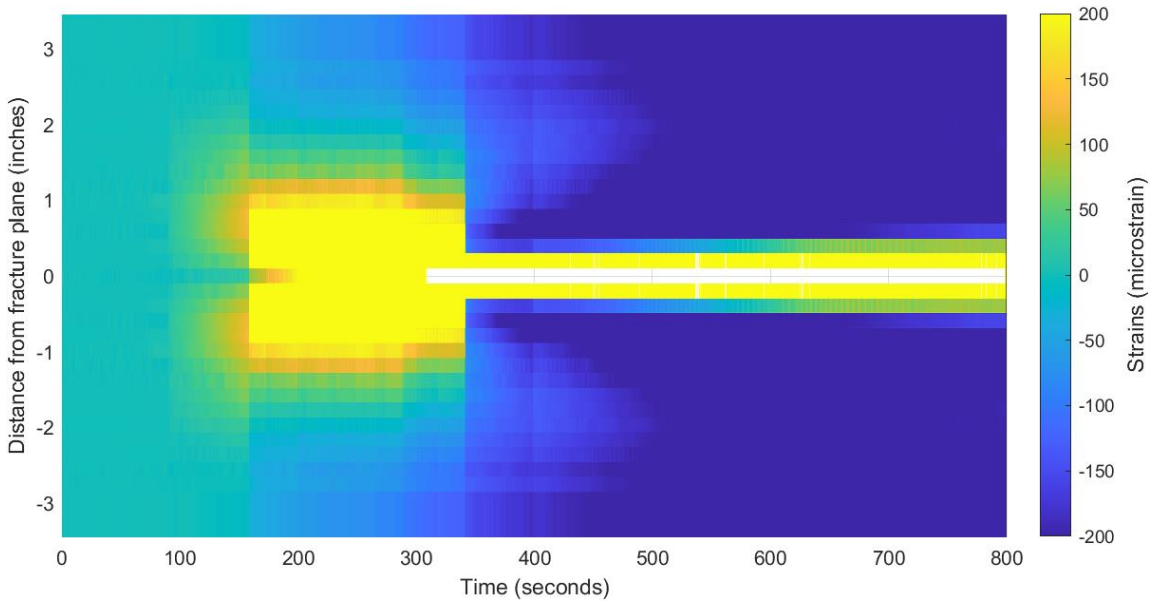
Distance from fracture plane (inches)
3
2
1
0
-1
-2
-3
0
100
200
300
400
500
600
700
800
Time (seconds)
200
150
100
50
0
-50
-100
-150
-200
Strains (microstrain)

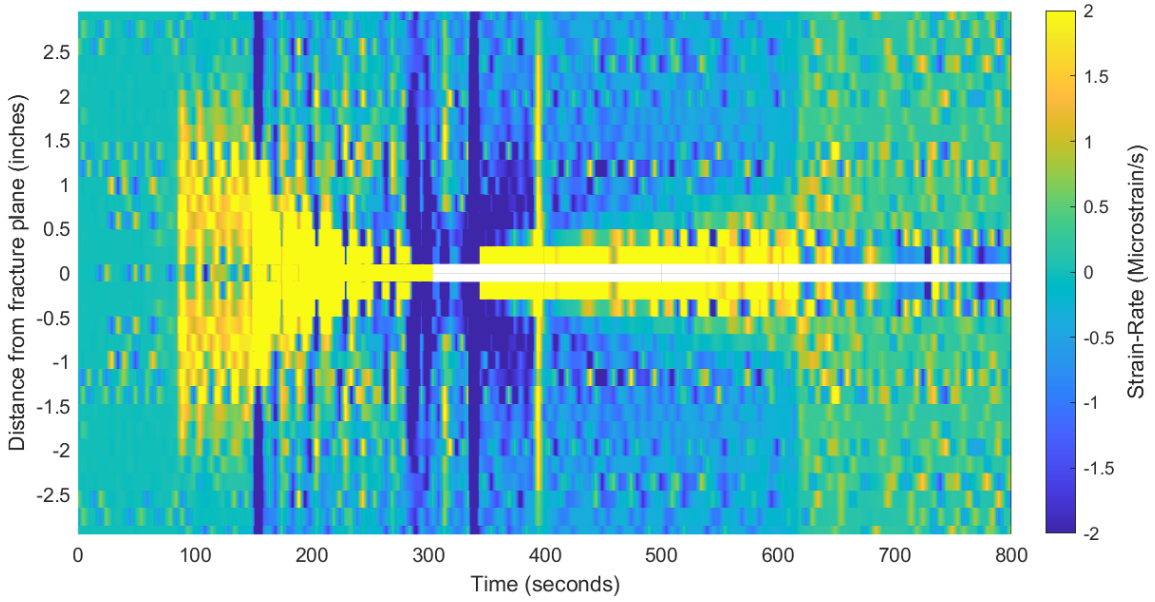
Distance from fracture plane (inches)
2.5
2
1.5
1
0.5
0
-0.5
-1
-1.5
-2
-2.5
0
100
200
300
400
500
600
700
800
Time (seconds)
2
1.5
1
0.5
0
-0.5
-1
-1.5
-2
Strain-Rate (Microstrain/s)